VIBRATION OF A SPINNING, CYCLIC SYMMETRIC ROTOR ASSEMBLED TO A FLEXIBLE STATIONARY HOUSING VIA MULTIPLE BEARINGS

Wei Che Tai

A dissertation
submitted in partial fulfillment of the
requirements for the degree of

Doctor of Philosophy

University of Washington

2014

Reading Committee:

I. Y. (Steve) Shen, Chair

Nicholas Boechler

Brian Fabien

Ulrich Hetmaniuk

Program Authorized to Offer Degree:
Mechanical Engineering

University of Washington

Abstract

VIBRATION OF A SPINNING, CYCLIC SYMMETRIC ROTOR ASSEMBLED TO A FLEXIBLE STATIONARY HOUSING VIA MULTIPLE BEARINGS

Wei Che Tai

Chair of the Supervisory Committee:
Professor I. Y. (Steve) Shen
Mechanical Engineering

A spinning cyclic symmetric rotor mounted on a stationary housing via multiple bearings is a very common platform used in modern rotary machinery. Representative examples include propellers, wind turbines, bladed turbine disks, and compressors. Nowadays, there are two main industrial trends in designing machines with the cyclic symmetric rotors. The first is to use larger rotors and lighter housing in order to increase efficiency and reduce costs. The second is to employ ground-based measurements.

Motivated by the industrial trends, this research is to develop a reduced-order formulation that accommodates arbitrary geometry of the spinning rotor and the stationary housing. Such a formulation is universal and will be valid for various cyclic symmetric rotors, ranging from wind turbines to bladed turbine disks. Mathematically, the governing equation of motion with reduced order takes the form of a set of ordinary differential equations with periodic coefficients associated with the spin speed. Characteristics drawn from this formulation can then be applied to any cyclic symmetric rotor mounted on a flexible housing. Furthermore, unstable response (e.g., parametric resonances) and stable response (e.g., rotor-based and ground-based response) of the rotor-bearing-housing system will be studied analytically, numerically, and experimentally, as follows.

In the analytical study, the system is first shown to have instabilities in terms of combination resonance of the sum type as a result of the periodic coefficients. All the resonance

peaks and corresponding bandwidth within a proper range of spin speeds, where the system remains positive definite, are analytically predicted by the method of multiple scales. As a result of combination resonance of the sum type, the instability occurs at extremely high spin speeds

Next, the stable response of the stationary and spinning system is studied analytically. The stationary system has two types of modes: rotor-dominant modes and housing-dominant modes. For the spinning system, two types of stable response are studied: the rotor-based response and the ground-based response. Both responses of rotor-dominant modes are similar to the case with rigid housing. The rotor-based response of housing-dominant modes, however, possesses a specific frequency splitting due to dominant vibration of the housing. For a housing-dominant mode with natural frequency $\omega^{(H)}$ obtained from the stationary system, when the system is spinning at spin speed ω_3, the rotor-based response splits into a forward and backward frequency branch equal to $\omega^{(H)} \pm \omega_3$. Such frequency splitting is defined as *gyroscopic splitting*. The gyroscopic splitting is analytically predicted via a perturbation analysis. Subsequently, the ground-based response is theoretically predicted. The theoretical prediction is briefly summarized as follows. The rotor-based response of a housing-dominant mode has frequency components $\omega^{(H)} \pm \omega_3$ due to gyroscopic splitting. Furthermore, if a rotor-based, cylindrical coordinate (r, θ, z) is employed to describe the vibration mode shape of a cyclic symmetric rotor, the mode shape is circumferentially modulated by the exponential function $e^{jk\theta}$, where k is the harmonic number which follows the identity $k = n + M(N)$. In this identity, n is the phase index governed by the cyclic symmetry of the rotor while $M(N)$ is multiples of numbers of identical substructures N. When the response is viewed from a ground-based observer, the circumferential harmonics $k\theta$ gives rise to additional frequency splitting $-k\omega_3$. Together with the gyroscopic splitting, the ground-based response splits into multiple forward and backward frequency branches following the rule $\omega^{(H)} - (k \pm 1)\omega_3$.

To confirm the results from the analytical study, a benchmark numerical model consisting of a cyclic symmetric rotor, a stationary housing, and two bearings is developed. The rotor

is a circular disk with four evenly spaced radial slots and a rigid hub. The stationary housing is a square plate with a central shaft subjected to fixed boundary conditions on the displacements at four corners. Based on this model, a numerical integration of the equation of motion ad use of the Floquet theory confirms the parametric resonance frequency and the instability bandwidth obtained from the method of multiple scales. Through the benchmark model, the gyroscopic splitting is also numerical confirmed for the rotor-based response. Moreover, ground-based response at various speed in the form of waterfall plots confirms that a housing-dominant mode splits following the rule $(k \pm \omega_3)$.

In order to verify the theoretical prediction of the ground-based response, a series of experiments on a stationary and spinning test rig is carried out. First of all, frequency response functions (FRFs) of the stationary rig are measured. Two FRFs are obtained using two excitation mechanisms. The first is to use an automatic hammer while the second is to use a piezoelectric (PZT) actuator. Two housing-dominant modes are identified by comparing the FRFs. Their mode shapes are characterized by one-nodal diameter and one-nodal line on the rotor and housing, respectively. Next, ground-based response of the spinning rig is measured to obtain waterfall plots. For the waterfall plot obtained form the hammer excitation, both housing-dominant modes reveal forward frequency branches which agree very well with the theoretical prediction. Only one housing-dominant mode presents a backward frequency branch. Nonetheless, the backward branch also agrees well with the theoretical prediction.

Lastly, a closed-form solution of rotor-bearing-housing systems with a special class of cyclic symmetry is derived. Specifically, the equation of motion can be transformed into a set of ordinary differential equations with constant coefficients, when the hub is rigid and the flexible portion of the rotor has only out-of-plane vibration motion. The transformed equation of motion appears as a time invariant gyroscopic system, whose closed-form solution is hence readily available. Both the original and transformed equation of motion are shown to have identical instabilities and rotor-based response through numerical simulations via the benchmark model.

TABLE OF CONTENTS

LIST OF FIGURES

LIST OF TABLES

DEDICATION

to my mother, father, and borther

Chapter 1
INTRODUCTION

The ultimate objective of this research is to provide a universal and rigorous modeling methodology for cyclic symmetric rotors assembled to housings with arbitrary geometry via multiple bearings. Hereinafter, such systems are referred to as rotor-bearing-housing systems. This methodology shall be tenable and legitimate to all cyclic symmetric rotor-bearing-housing systems. This methodology will also be tested and justified via multiple avenues, including numerical simulations, analytical predictions, and experimental verification. To this end, we aim to accomplish four specific goals in this research proposed as follows.

1. The first goal is to develop a rigorous mathematical formulation that is capable of modeling the rotor-bearing-housing systems and thus deriving the governing equation of motion.

2. The second goal is to study characteristics of the equation of motion whose parametric resonances and ground-based responses are of our primary interest. Both numerical and analytical analyses on a benchmark model are proposed to predict parametric resonances and ground-based stable responses.

3. The third goal is to verify the prediction of ground-based responses via calibrated experiments. Two experiments are performed. The first is performed on the stationary system and the other is on the spinning system.

4. The final goal is to derive analytic, closed-form, solutions of the equation of motion of a special class of cyclic symmetric rotors. More specifically, the stationary mode shapes of cyclic symmetric rotors have entirely out-of-plane motion. Examples include spinning disks.

1.1 Background and Literature Review

In this section a general background and literature review is introduced in response to the itemized goals respectively.

1.1.1 Reduced-order Model for Cyclic Symmetric Rotor-bearing-housing Systems

A spinning cyclic symmetric rotor mounted on a stationary housing via multiple bearings is a very common platform used in modern rotary machinery. Representative examples include propellers, wind turbines, bladed turbine disks, and compressors.

Traditionally, the housing is massive and rigid, so vibration tends to be more pronounced at the rotor. Therefore, most literature on rotor dynamics focuses on vibration analyses of spinning rotors. Traditional analyses of cyclic symmetric rotary machines often ignore the housing and bearings or assume rigid housing [7, 8, 9, 10, 11, 1, 12, 13, 14, 4, 2, 3], and primarily focus on rotor-based responses [15, 16].

In the last decade, emergent applications started to call for designs that employ a lighter housing or a larger rotor. A natural consequence is that vibration of the rotor and housing becomes coupled through the bearings. As an example, wind turbines now adopt long, huge blades, whereas the housing is reduced in weight to lower material costs. Research has shown that wind turbines experience considerable coupled vibration between the blades and the tower [17, 18, 19, 20, 21]. Such vibration could not only cause fatigue failures but also health concerns known as Wind Turbine Syndrome [22]. Similarly, in developing greener engines with higher fuel efficiency and less emission, turbine engine industry seeks to reduce the weight (and hence rigidity) and to increase the bypass ratio of turbine engines. This design trend tends to cause considerable coupled vibration between the rotating parts and the stationary parts and motivates vibration analyses of entire rotor-bearing-housing systems [23, 24].

Despite of the attempts to model a rotor-bearing-housing system, the rotor is assumed to either take a specific geometry (e.g., a beam) or be rigid body and lumped mass [25, 26]. A universal model for cyclic symmetric rotors and housing with arbitrary geometry still remains open.

Developing such a universal formulation, however, is a non-trivial task. There are two major challenges to overcome. The first challenge is that a systematic way to incorporate a stationary housing and multiple bearings to a spinning cyclic symmetric rotor is yet to be developed. The only knowledge thus far in this context is that presence of the bearings may cause some rotor modes to coupled with the bearings, while other modes may not [27]. More specifically, if a rotor vibration mode presents unbalanced inertia forces or moments as the rotor vibrates, the rotor vibration mode will couple with the housing. These vibration modes are known as *unbalanced modes* [27].

The second challenge is that equations of motion could possess extremely high order if a rotor-bearing-housing system is not properly formulated. Theoretically, such a system is governed by partial differential equations with time-varying coefficients because the rotor's mass and stiffness distributions change periodically with respect to the housing [17, 18, 19]. If a finite element method is used to discretize the system, the order will be so high that numerical solutions become impractical. Furthermore, due to the complex interaction between rotating rotors and non-rotating housings, approximation techniques which are involved with high degrees of freedom, such as the multi-blade coordinate transformation [28, 29], are often to be used. These additional degrees of freedom further increase the computational difficulties. Therefore, novel ways must be sought to significantly reduce the order to make numerical predictions feasible.

In order to develop a universal formulation that can accommodate both spinning rotors and stationary housings, two coordinate systems are employed in the formulation. A rotor-based coordinate system is used for the spinning rotor to accommodate its cyclic symmetry [1, 2, 3, 4]. A ground-based coordinate is used to describe response of the stationary housing [5]. The rotor and the housing are then discretized in respective coordinate systems, for example via mode shapes, to reduce the order. The rotor, housing, and bearings are then assembled together to derive the equation of motion with a reduced order. This process will be explained in detail in Chapter 2.

1.1.2 Ground-based Response

Recently novel sensing techniques started to monitor ground-based response of spinning cyclic symmetric rotors. For example, turbine engine industry has developed blade-tip-timing sensing techniques to measure vibration of spinning bladed turbine disks [30, 31, 32, 33, 34]. The advantage of monitoring ground-based response is that it is easy to implement practically and experimentally. Nevertheless, theoretical and numerical analysis regarding ground-based response of coupled rotor-bearing-housing systems is still limited. Therefore, there are practical needs for identifying characteristics of such system and thus analysing ground-based responses. Studying both features will help understand experimental vibration response of the entire rotor-bearing-housing systems.

However, finding response or identifying characteristics of the coupled rotor-bearing-housing systems is not trivial. It faces several challenges. The first challenge is complexity of the ground-based response for a spinning rotor-bearing-housing system. When only a rotor is considered, existing literature has shown that ground-based response of the rotor will split into primary and secondary branches of frequency components governed by its cyclic symmetry [3]. It remains open how the housing and bearings would affect these primary and secondary frequency components.

Second, there is no mathematical analysis to guide numerical simulations after the equation of motion is derived. Generally speaking, coupled vibration between the rotor and housing depends on geometry of the system as well as characteristics of the bearings. Numerical simulations alone are difficult to provide complete insights into characteristics of the coupled system. To better understand the system characteristics, a theoretical analysis is needed prior to the numerical simulations.

Third, numerical solutions are hard to interpret. Theoretically speaking, one can solve the equation of motion numerically and transform the solution back to the ground-based observer. The solutions will be extremely complicated and will not make sense unless a theoretical framework is developed prior to the numerical simulations. In order to keep track of the numerical solutions, a theoretical analysis on the rotor-based and the ground-based responses is needed to interpret the numerical simulations.

Therefore, theoretical analysis on the equation of motion will help understanding the ground-based response of the systems. A theoretical analysis along with numerical simulations will be presented in Chapter 3 and 4 to understand the ground-based response.

1.1.3 Experimental Verification

In addition to numerical and analytical study on the systems, experimental verification always plays an important role on justifying the methodology. Design and implementation of comprehensive experiments to the extent that the numerical and analytical prediction of the responses are justified are not an easy task. For spinning cyclic symmetric rotor-bearing-housing systems, there are several difficulties.

The first difficulty is run-out signals. The run-out signals appear as multiples of spin speed and are ubiquitous in the region of measuring responses of rotary machinery. Many sources could contribute to the run-out signal. It could be mechanical reasons such as the surface finish of the objects measured and rotor balance after assembly. It could be electrical reasons, known as electrical run-out, which often appears when using proximity probe to measure displacement [35]. To attenuate run-out signals, careful assembly of the systems, precise alignment between the rotor and housing, and conditioning measurement equipment are essential.

Second, appropriate experiment methods in regard to properly exciting the entire rotor-bearing-housing systems remains open. Typically speaking, a generic quantity that characterizes vibration of spinning rotors in ground-based coordinate is impulse response function [5, 3]. In these literature, automatic hammers were used to generate impact forces on the rotors as well as serve as input signal of impulse response functions of the systems. This method, however, may not be most appropriate to a rotor-bearing-housing system because the hammer may not impart enough energy to excite the heavier housing into needed vibration.

Third, as aforementioned, the ground-based response of a spinning cyclic symmetric rotor-bearing-housing system is complex. After the rotor is spinning, the ground-based responses of the rotor will split into primary and secondary branches of frequency components

governed by its cyclic symmetry [3]. Direct measurement on the spinning rotor will result in additional frequency components resulted from the presence of the stationary housing.

An experimental setup that addresses theses difficulties and successfully verifies the theoretical predictions will be introduced in Chapter 6.

1.1.4 Closed-form Solution

To date, solutions of the equations of motion of spinning cyclic symmetric rotor-bearing-housing systems rely on numerical methods. Numerical error sometimes can be detrimental to the accuracy even the stability of solutions. When it first comes to solving differential equations numerically, it is conventionally to test the numerical schemes through use of equations whose analytical solutions are available. Therefore, closed-form solutions are always desirable.

Generally speaking, existence of closed-form solutions highly depends on the geometry of rotors. When rotors have complex geometry, closed-form solutions are not plausible. Closed-form solutions, however, are achievable when rotors have specific geometry. For example, axisymmetric rotors-bearing-housing systems can be solved to obtain closed-form solutions. Tseng et al. [5] shows that equation of motion of an axisymmetric rotor-bearing-housing system can take the form of ordinary differential equations with constant coefficients. Since the differential equations have constant coefficients, standard eigenvalue approach is sufficient to obtain closed-form solutions.

On the other hand, equation of motion of a general cyclic symmetric rotor-bearing-housing takes the form of ordinary differential equations with periodic coefficients [6]. Closed-form solutions of this type of differential equations are generally limited, and often times perturbation techniques have to be used to obtain approximated solutions [28, 36, 37]. Nevertheless, Josic and Rosenbaum [38] introduced a specific family of equations with periodic coefficients that have closed-form solutions. This family of equations is formulated with a time varying rotation matrix. Furthermore, Kozlov [39] also pointed out that periodic systems are highly related to time invariant gyroscopic systems via proper time variant, orthogonal, coordinate transformations. Altogether, it is possible to seek a proper coordinate

transformation that converts the formulation of a cyclic symmetric rotor-bearing-housing system into ordinary differential equations with constant coefficients for a closed-form solution.

Despite the similarity between the equation of motion of the rotor-bearing-housing system and the equations in [38, 39], the former is much more complicated equation of motion and has much higher degrees of freedom than the latter. The techniques, therefore, can not be applied directly to the rotor-bearing-housing systems unless certain simplification or assumptions are made equation of motion of the system. One of those assumptions is that the stationary mode shapes of the rotor have entirely out-of-plane motion. Under this assumption, it can be shown that the repeated and distinct modes of the rotor are decoupled in the centrifugal softening matrix, gyroscopic matrix in the equations of motion [3] and the bearing stiffness matrix [6]. It will be demonstrated in Chapter 5 that rotor-bearing-housing systems satisfying the assumption possess closed-form solutions.

Since the closed-form solutions only require the kinematics assumptions on the rotor, it is equally applicable to rotor-bearing-housing systems with ball bearings and fluid dynamics bearings. The latter is the main stream in the industry of hard disk drives (HDD) and has wide applications in the field of turbomachinery.

1.2 Outline

This thesis consists of seven chapters. In Chapter 1, a general background and literature review are given to explain the motivation, challenges, and significance of this research. Also, the outline is given.

In Chapter 2, the mathematical formulation of the reduced-order model is derived. Two coordinate systems are employed in the formulation. A rotor-based coordinate system is used for the spinning rotor to accommodate its cyclic symmetry while a ground-based coordinate is used to describe response of the stationary housing. The rotor, housing, and bearings are assembled together to derive the equation of motion with reduced order. Solutions of the equation of motion are obtained via the method of multiple scales or numerical integrations.

In Chapter 3 and 4, the characteristics of the model are studied based on a benchmark

model. The characteristics fall into two categories of response, unstable response (parametric resonances) and stable response (rotor-based and ground-based response).

In Chapter 3, parametric resonances of the equation of motion are studied. As a result of the cyclic symmetry, the governing equation of the rotor-bearing-housing system appears in the form of a set of ordinary differential equations with periodic coefficients. Based on this governing equation, it can be shown that the coupled rotor-bearing-housing system may experience parametric instabilities when the rotor spins at extremely high spin speed.

Two numerical examples are conducted using the equations of motion to demonstrate the parametric resonances. The first example has an axisymmetric disk as the spinning rotor, while the second example has a cyclic symmetric rotor in the form of a circular disk with evenly spaced radial slots. The numerical model used this example will be the benchmark model for the rest of the paper. In both examples, the rotor is supported on a stationary elastic plate (i.e., the housing) via two elastic bearings. We then analyze stability of the rotor-bearing-housing system as a function of the spin speed to study how cyclic symmetry affects the stability. Finally, how damping affects the stability of a coupled rotor-bearing-housing system is demonstrated.

In Chapter 4, the rotor-based and ground-based response are studied. After understanding the unstable response, efforts are made to understand the rotor-based and ground-based response of the coupled rotor-bearing-housing system at conventional spin speed where the response is stable. Effects of coupling on the rotor-based and ground-based response are discussed in two theoretical analyses. At the beginning, the first theoretical analysis is performed on the coupled, stationary, system to demonstrate the interaction between the stationary rotor and housing resulted from bearing deformation. The analysis shows that the stationary system has two major types of modes: rotor-dominant modes $\omega^{(R)}$ and housing-dominant modes $\omega^{(H)}$. Later, effects of coupling on the rotor-based response of the spinning system are studied. Next, the second theoretical analysis is performed on the spinning system to study the interaction between the spinning rotor and housing resulted from periodic bearing deformation. First of all, the analysis suggests that the rotor-base response of rotor-dominant modes is similar to that of a system with rigid housing and does not show significant effects of coupling with the housing. Hence it is not discussed

in detail. Secondly, it shows that the rotor-based response of housing-dominant modes has forward and backward frequency splitting amount to the spin speed $\pm\omega_3$, which manifests the interaction between the spinning rotor and flexible housing. Such frequency splitting is defined as *gyroscopic splitting*. The gyroscopic splitting is analytically predicted by a perturbation method. The numerical fast Fourier transform (FFT) of the rotor-based response of housing-dominant modes of the benchmark used in Chapter 3 is computed and the results successfully verify the theoretical prediction. Lastly, the ground-based response of housing-dominant modes is theoretically predicted by transforming the rotor-based response to a ground-based observer. The prediction states that the ground-based response has multiple, patterned, frequency components $\omega^{(H)} - (k \pm \omega_3)$, where k is the index governed by the cyclic symmetry of the rotor while $\pm\omega_3$ comes from the gyroscopic splitting of housing-dominant mode $\omega^{(H)}$, as comprehensive interactions between the spinning rotor and housing. Once again, the benchmark model is used to confirm the theoretical prediction of the ground-based response and help highlight important characteristics of stable responses of the coupled system. The frequency components are observed in numerical waterfall plots are generated via the benchmark model.

In Chapter 5, the closed-form solution for a special cyclic symmetric rotor is derived. It begins with two important kinematic assumptions. Next, a brief review of equation of motion is given. Two preliminary work facilitating the derivation are prepared. The first is simplification of the periodic coefficients of the system. The second is discussion on boundary forces and moments and their relation between mode shapes with distinct and repeated natural frequencies. Third, existence of the coordinate transformation that gives rise to closed-form solution is proved. Finally, two numerical simulations are performed to verify the proof and further discussion of potential applications and implications of the closed-form solution are also given.

In Chapter 6, the experimental verification of the rotor-bearing-housing system is discussed in great detail. It consists of three parts. At the beginning, the experimental setup is introduced. The setup is to mimic the numerical benchmark as much as possible. Next, the experimental methods, results, and discussion of measured response of the stationary system are presented. Two frequency response functions (FRFs) are obtained using two excitation

modes. The first is to use automatic hammer while the second is to use the piezoelectric (PZT) actuator. Two housing-dominant modes $\Omega_L^{(H)}$ and $\Omega_H^{(H)}$ are identified by comparing the magnitude of peaks in the FRFs. At last, the experimental methods, results, and discussion of measured response of the spinning system are presented. In particular, the measured response is the ground-based response which is used to verify the theoretical and numerical analyses in Chapter 4. The same excitation modes are used to excite the spinning system. Waterfall plots are obtained. The waterfall plot associated with the first excitation mode reveal the forward and backward frequency branches of $\Omega_H^{(H)}$, which confirms well with the theoretical prediction. For the other mode $\Omega_L^{(H)}$, it shows only the forward branch with absence of the backward branch. Nonetheless, the forward branch also confirms well with the prediction.The waterfall plot associated with the second mode is also generated. Yet, it does not provide more information than the first plot.

In Chapter 7, conclusions of all the previous chapters are summarized and extension of current work is briefly discussed based on the collective findings in this thesis.

Chapter 2

REDUCED-ORDER MODEL

In this chapter, the mathematical formulation of the equation of motion with reduced order (referred to as the reduced-order model hereinafter) will be derived.

As aforementioned, two coordinates are employed to describe the rotor and housing respectively and derive the equation of motion with reduced order. Specifically, the derivation consists of the following steps.

The first step is to extract mode shapes of the rotors and housings. Since the two coordinates are fixed relative to the rotor and the housing, respectively, the rotors and housings could be considered stationary in the respective coordinates. Then a finite element analysis is conducted on the rotor and housing to obtain their natural frequencies and mode shapes. Since the mode shapes are orthogonal in respective coordinate systems, they form two complete sets of basis.

The second step is discretization through use of the two coordinate systems. Since the mode shapes are complete, rotor-based response of the spinning rotor can be represented in terms of its mode shapes and their modal response (also known as generalized coordinates). Likewise, ground-based response of the stationary housing can be represented in terms of its mode shapes and their modal response. Therefore, kinetic and potential energies of the rotor and housing can be discretized in terms of these two sets of generalized coordinates. Similarly, bearing deformation resulting from relative displacements between the rotor and housing can also be discretized. (Since two coordinate systems are present, the relative displacement is only meaningful after a coordinate transformation is performed.)

2.1 Coordinate Systems

To begin with, we employ two coordinate systems in the formulation to over come the difficulties of modelling the coupled rotor-bearing-housing systems. A rotor-based coordinate

system is used for the spinning rotor to accommodate its cyclic symmetry [1, 2, 3, 4]. A ground-based coordinate is used to describe response of the stationary housing [5].

2.1.1 Space Fixed Coordinate XYZ

Let O be a convenient reference point on the housing. With O being the origin, one can define an inertia frame XYZ with unit vectors $\mathbf{I}$, $\mathbf{J}$, and $\mathbf{K}$. Now consider an arbitrary point P in the housing with position vector

$$\mathbf{r} \equiv r_x\mathbf{I} + r_y\mathbf{J} + r_z\mathbf{K} \tag{2.1}$$

2.1.2 Rotating Coordinate xyz

Let $\mathbf{i}$, $\mathbf{j}$, and $\mathbf{k}$ be the unit vectors of the xyz coordinate system and $\mathbf{I}$, $\mathbf{J}$, and $\mathbf{K}$ be the unit vectors of the inertia frame XYZ (or $\tilde{X}\tilde{Y}\tilde{Z}$) coordinate system. Then

The ground-based coordinate XYZ is the inertia frame with a fixed point O_1 as the origin.

The rotor-based coordinate xyz, on the other hand, is a coordinate with O_2 as the origin and rotating about its z axis with constant angular velocity ω_3; moreover, z axis is fixed in the space

Let $\mathbf{I}$, $\mathbf{J}$, and $\mathbf{K}$ be the unit vectors of XYZ while $\mathbf{i}$, $\mathbf{j}$, and $\mathbf{k}$ be the unit vectors of xyz. Then

$$\begin{pmatrix} \mathbf{i} \\ \mathbf{j} \\ \mathbf{k} \end{pmatrix} = \mathbf{R}(t) \begin{pmatrix} \mathbf{I} \\ \mathbf{J} \\ \mathbf{K} \end{pmatrix} \tag{2.2}$$

In equation (2.2), $\mathbf{R}(t)$ is a coordinate transformation matrix between XYZ and xyz

$$\mathbf{R}(t) = \begin{bmatrix} cos(\omega_3 t) & -sin(\omega_3 t) & 0 \\ sin(\omega_3 t) & cos(\omega_3 t) & 0 \\ 0 & 0 & 1 \end{bmatrix} \tag{2.3}$$

After employing the two coordinate sytems XYZ and xyz, the stationary housing and the spinning rotor can be formulated under XYZ and xyz, respectively.

2.2 Formulation of the Stationary Housing

The stationary housing is modelled as an elastic structure with arbitrary shapes. When the housing undergoes an elastic deformation $\mathbf{W}^H(\hat{\mathbf{r}}, t)$, where the superscript (H) refers to the stationary housing, it can be approximated in terms of n_h vibration modes via

$$\mathbf{W}^H(\hat{\mathbf{r}}, t) \approx \sum_{n=1}^{n_h} \mathbf{W}_n^H(\hat{\mathbf{r}}) q_n^H(t) \tag{2.4}$$

In equation (2.4),

$$\mathbf{W}_n^H(\hat{\mathbf{r}}) \equiv W_{xn}^H(\hat{\mathbf{r}})\mathbf{I} + W_{yn}^H(\hat{\mathbf{r}})\mathbf{J} + W_{zn}^H(\hat{\mathbf{r}})\mathbf{K} \tag{2.5}$$

is the n-th vibration mode shape and $q_n^H(t)$ is the corresponding generalized coordinate. In addition, the mode shapes satisfy the orthonormality conditions $\int \mathbf{W}_m^H(\hat{\mathbf{r}}) \cdot \mathbf{W}_n^H(\hat{\mathbf{r}}) dm = \delta_{mn}$ and $\int V_H \left[\mathbf{W}_m^H(\hat{\mathbf{r}}), \mathbf{W}_n^H(\hat{\mathbf{r}})\right] dV = \left[\omega_n^H\right]^2 \delta_{mn}$, where δ_{mn} is the Kronecker delta, ω_n^H is the natural frequency of the n-th vibration mode, and $V_H[\bullet, \bullet]$ is an potential energy inner-product operator. Since the housing is stationary, the motion of point P results entirely from the elastic deformation $\mathbf{W}^H(\hat{\mathbf{r}}, t)$. Hence, the displacement of P is

$$\mathbf{R}_P^H \equiv \mathbf{W}^H(\hat{\mathbf{r}}, t) \tag{2.6}$$

and the velocity of point P is

$$\dot{\mathbf{R}}_P^H = \sum_{n=1}^{n_h} \mathbf{W}_n^H(\hat{\mathbf{r}}) \dot{q}_n^H(t) \tag{2.7}$$

where (2.4) has been used. Moreover, the kinetic energy of the housing is $T^H = \frac{1}{2} \sum_{n=1}^{n_h} \left[\dot{q}_n^H\right]^2$ and the potential energy of the housing is $V^H = \frac{1}{2} \int V_h[\mathbf{W}^H, \mathbf{W}^H] dV = \frac{1}{2} \sum_{n=1}^{n_h} \left[\omega_n^H q_n^H(t)\right]^2$.

2.3 Formulation of the Rotor

The rotor is modelled as an elastic solid of arbitrary geometry with its centroid G located on the spin axis (i.e., rotor is perfectly balanced). Moreover, the rotor is subject to free-body boundary conditions and can undergo rigid-body motion as well as elastic deformation. To formulate the motion of the rotor, let us first define a virgin state for reference. In the virgin state, the rotor-bearing-housing system experiences no elastic deformation and no

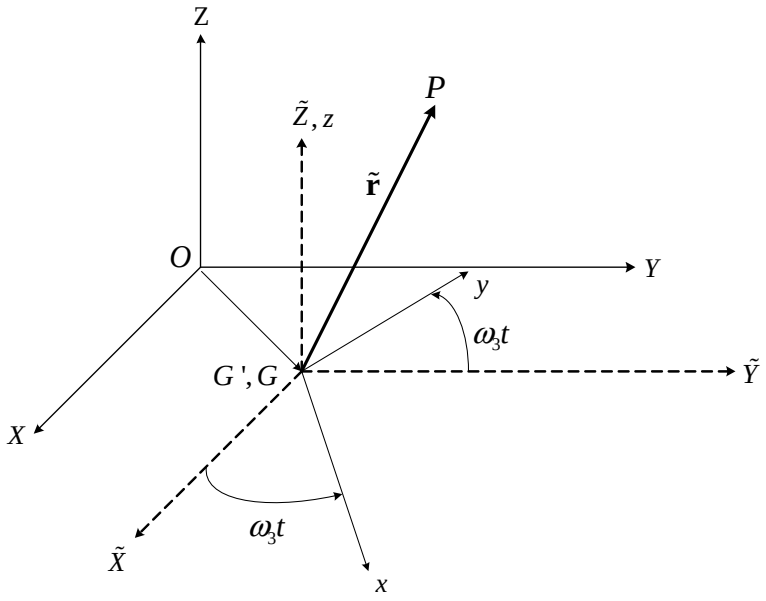

Figure 2.1: Coordinate System xyz for the Spinning Rotor

rigid-body motion except the spin of the rotor. Moreover, let G' denote the location of the centroid in the virgin state; see Fig. 2.1. (Note that G and G' coincide in the virgin state, but will correspond to two different points in actual motion.) With G' as the origin, one can define an inertia Cartesian coordinate system $\tilde{X}\tilde{Y}\tilde{Z}$ with $\tilde{Z}$ being the spin axis in the virgin state. (Note that the rotor might wobble in actual motion; therefore, $\tilde{Z}$ is not the spin axis in actual motion.) Also, one can define a rotating coordinate system xyz with constant angular velocity ω_3. It is also convenient to assume that xyz coincides with the principal axes of the rotor in the virgin state. Note that xyz axes do not attach to the rotor, because the rotor can rock and translate, but xyz axes cannot. Nonetheless, xyz axes are the best coordinate system to describe the motion of the rotor.

Now let us consider the motion of a point P on the rotor. In the virgin state, position of P relative to G' is defined by vector $\tilde{\mathbf{r}}$ (Fig. 2.1), where $\tilde{\mathbf{r}} \equiv \tilde{r}_x\mathbf{i} + \tilde{r}_y\mathbf{j} + \tilde{r}_z\mathbf{k}$. In the deformed state, the position of P with respect to the inertia frame XYZ becomes

$$\mathbf{R}_P^R(\tilde{\mathbf{r}}, t) = \overrightarrow{OG'} + \tilde{\mathbf{r}} + \mathbf{W}^R(\tilde{\mathbf{r}}, t) \tag{2.8}$$

where $\mathbf{W}^R(\tilde{\mathbf{r}},t)$ is the displacement of P that includes rigid-body motion (excluding the spin) and elastic deformation. The superscript (R) refers to the rotor.

Under the coordinate system xyz, several sets of complete mode shapes are available. For example, when the rotor is stationary, undamped, and subjected to free boundary conditions, the rotor will have a set of complete mode shapes

$$\mathbf{W}_n^R(\tilde{\mathbf{r}}) \equiv W_{xn}^R(\tilde{\mathbf{r}})\mathbf{i} + W_{yn}^R(\tilde{\mathbf{r}})\mathbf{j} + W_{zn}^R(\tilde{\mathbf{r}})\mathbf{k} \tag{2.9}$$

with natural frequencies ω_n^R, $n = 0, 1, 2, \ldots$. (For rotors with complicated geometry, $\mathbf{W}_n^R(\tilde{\mathbf{r}})$ and ω_n^R can be calculated through finite element analyses, for example.) Moreover, these mode shapes are orthogonal satisfying $\int \mathbf{W}_m^R(\tilde{\mathbf{r}})\cdot\mathbf{W}_n^R(\tilde{\mathbf{r}})dm = \delta_{mn}$ and $\int V_R\left[\mathbf{W}_m^R(\tilde{\mathbf{r}}), \mathbf{W}_n^R(\tilde{\mathbf{r}})\right] dV = \left[\omega_n^R\right]^2 \delta_{mn}$, where $V_R\left[\bullet,\bullet\right]$ is a potential energy inner-product operator of the rotor. Also note that the mode shapes $\mathbf{W}_n^R(\tilde{\mathbf{r}})$ include six infinitesimal rigid-body modes with zero natural frequencies. Let us label the zero-th mode as the infinitesimal rigid-body spin of the rotor, i.e.,

$$\mathbf{W}_0^R(\tilde{\mathbf{r}}) \equiv \frac{1}{\sqrt{\bar{I}_3}}\left(-\tilde{y}\mathbf{i} + \tilde{x}\mathbf{j}\right) \tag{2.10}$$

where $\bar{I}_3$ is the centroidal mass moment of inertia about the spin axis.

Since the vibration mode shapes are complete, the position vector $\mathbf{R}_P^R(\tilde{\mathbf{r}},t)$ of the rotor in (2.8) can be approximated as

$$\mathbf{R}_P^R(\tilde{\mathbf{r}},t) \approx \overrightarrow{OG'} + \tilde{\mathbf{r}} + \sum_{n=1}^{n_r} \mathbf{W}_n^R(\tilde{\mathbf{r}}) q_n^R(t) \tag{2.11}$$

where $q_n^R(t)$ is the generalized coordinates whose response is to be determined, and n_r is the number of modes retained in the series for approximation. Note that the rigid-body spin of the rotor, $\mathbf{W}_0^R(\tilde{\mathbf{r}})$, does not appear in $\mathbf{R}_P^R(\tilde{\mathbf{r}},t)$, because the spin of the rotor is redundant and has been described by the rotation of the coordinate system xyz. With the displacement in (2.11), the potential energy of the rotor is

$$V^R = \frac{1}{2}\int V_R[\mathbf{W}^R, \mathbf{W}^R]dV = \frac{1}{2}\sum_{n=1}^{n_r}\left[\omega_n^R q_n^R(t)\right]^2 \tag{2.12}$$

According to (2.11), the velocity of point P is

$$\dot{\mathbf{R}}_P^R(\tilde{\mathbf{r}},t) = \boldsymbol{\omega}\times\tilde{\mathbf{r}} + \sum_{n=1}^{n_r}\mathbf{W}_n^R(\tilde{\mathbf{r}})\dot{q}_n^R(t) + \sum_{n=1}^{n_r}\left[\boldsymbol{\omega}\times\mathbf{W}_n^R(\tilde{\mathbf{r}})\right] q_n^R(t) \tag{2.13}$$

where $\boldsymbol{\omega} = \omega_3 \mathbf{k}$. With the velocity field (2.13), the kinetic energy of the rotor is

$$\begin{aligned} T^R &= \frac{1}{2}\bar{I}_3\omega_3^2 + \frac{1}{2}\sum_{n=1}^{n_r}\left[\dot{q}_n^R\right]^2 + \frac{1}{2}\omega_3^2\sum_{n=1}^{n_r}\sum_{m=1}^{n_r}\lambda_{mn}q_m^R(t)q_n^R(t) \\ &+ \omega_3\sum_{n=1}^{n_r}J_{bn}^R\dot{q}_n^R(t) + \omega_3^2\sum_{n=1}^{n_r}J_{cn}^R q_n^R(t) \\ &+ \omega_3\sum_{n=1}^{n_r}\sum_{m=1}^{n_r}g_{nm}q_m^R(t)\dot{q}_n^R(t) \end{aligned} \tag{2.14}$$

where

$$\lambda_{mn} = \lambda_{nm} \equiv \delta_{mn} - \int W_{mz}^R(\tilde{\mathbf{r}})W_{nz}^R(\tilde{\mathbf{r}})dm \tag{2.15}$$

$$J_{bn}^R \equiv \mathbf{k}\cdot\int \tilde{\mathbf{r}}\times\mathbf{W}_n^R(\tilde{\mathbf{r}})dm \tag{2.16}$$

$$J_{cn}^R \equiv \int\left[\tilde{\mathbf{r}}\cdot\mathbf{W}_n^R(\tilde{\mathbf{r}}) - \tilde{r}_z W_{nz}^R(\tilde{\mathbf{r}})\right]dm \tag{2.17}$$

$$g_{nm} = -g_{mn} \equiv \mathbf{k}\cdot\int\left[\mathbf{W}_m^R(\tilde{\mathbf{r}})\times\mathbf{W}_n^R(\tilde{\mathbf{r}})\right]dm \tag{2.18}$$

For (2.15) to (2.18), the integration is carried out with respect to the rotor.

2.4 Bearing Deformations

The purpose of this section is to derive bearing deformations in terms of $q_n^H(t)$ and $q_n^R(t)$. Let A and A' be two mating surfaces of a bearing (e.g., inner race and outer race), where A is on the rotor and A' is on the stationary housing. When the spindle vibrates, the two bearing surfaces move relatively to each other. In addition, the relative motion could be linear or angular.

To determine the linear bearing deformation, let $\mathbf{r_A}$ and $\mathbf{r_{A'}}$ be the position vector of A and A', respectively. Then $\mathbf{r_A} - \mathbf{r_{A'}}$ defines the linear bearing deformation. According to Fig. 2.2 and (2.11),

$$\mathbf{r}_A = \overrightarrow{OG'} + \overrightarrow{G'A} + \sum_{n=1}^{n_r}\mathbf{W}_n^R(\tilde{\mathbf{r}}_A)q_n^R(t) \tag{2.19}$$

According to (2.6),

$$\mathbf{r}_{A'} = \sum_{n=1}^{n_h}\mathbf{W}_n^H(\hat{\mathbf{r}}_A)q_n^H(t) \tag{2.20}$$

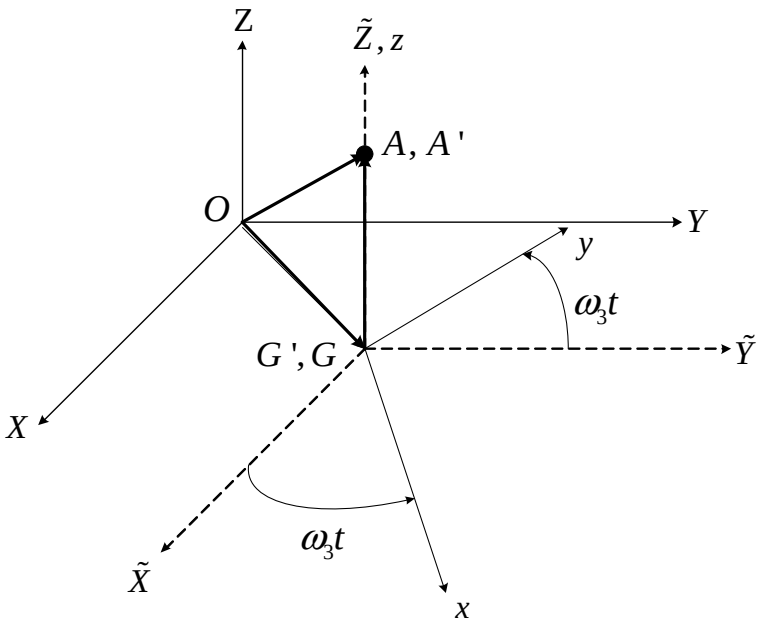

Figure 2.2: Bearing Position A and A'

Based on (2.19) and (2.20), the linear bearing deformation is $\mathbf{r}_A - \mathbf{r}_{A'} \equiv \Delta_x \mathbf{I} + \Delta_y \mathbf{J} + \Delta_z \mathbf{K}$, where

$$\begin{aligned} \Delta_x &\equiv \sum_{n=1}^{n_r} \left[W_{xn}^R(\tilde{\mathbf{r}}_A) \cos \omega_3 t - W_{yn}^R(\tilde{\mathbf{r}}_A) \sin \omega_3 t \right] q_n^R(t) \\ &- \sum_{n=1}^{n_h} W_{xn}^H(\hat{\mathbf{r}}_A) q_n^H(t) \end{aligned} \tag{2.21}$$

$$\begin{aligned} \Delta_y &\equiv \sum_{n=1}^{n_r} \left[W_{xn}^R(\tilde{\mathbf{r}}_A) \sin \omega_3 t + W_{yn}^R(\tilde{\mathbf{r}}_A) \cos \omega_3 t \right] q_n^R(t) \\ &- \sum_{n=1}^{n_h} W_{yn}^H(\hat{\mathbf{r}}_A) q_n^H(t) \end{aligned} \tag{2.22}$$

and

$$\Delta_z \equiv \sum_{n=1}^{n_r} W_{zn}^R(\tilde{\mathbf{r}}_A) q_n^R(t) - \sum_{n=1}^{n_h} W_{zn}^H(\hat{\mathbf{r}}_A) q_n^H(t) \tag{2.23}$$

Note that the coordinate transformation (2.2) is used, because $\mathbf{W}_n^R(\tilde{\mathbf{r}}_A)$ in (2.18) is represented in coordinates xyz and must be transformed into the inertia frame XYZ.

For the angular deformation of the bearing, the elastic deformation of the stationary housing will induce an infinitesimal rigid-body rotation

$$\boldsymbol{\alpha} \equiv \alpha_x \hat{\mathbf{I}} + \alpha_y \hat{\mathbf{J}} + \alpha_z \hat{\mathbf{K}} = \frac{1}{2} \nabla \times \sum_{n=1}^{n_h} \mathbf{W}_n^H(\hat{\mathbf{r}}_A) q_n^H(t) \tag{2.24}$$

where $\hat{\mathbf{r}}_A$ is the position vector of A in the XYZ frame. Similarly, the rotor will experience an infinitesimal rigid-body rotation

$$\boldsymbol{\beta} \equiv \beta_x \mathbf{i} + \beta_y \mathbf{j} + \beta_z \mathbf{k} = \frac{1}{2} \nabla \times \sum_{n=1}^{n_r} \mathbf{W}_n^R(\tilde{\mathbf{r}}_A) q_n^R(t) \tag{2.25}$$

Note that $\boldsymbol{\beta}$ in (2.25) is written in the rotating frames xyz. Transforming $\boldsymbol{\beta}$ back to the inertia coordinates XYZ via (2.2) results in

$$\begin{aligned} \boldsymbol{\beta} &= \sum_{n=1}^{n_r} \left(\beta_{xn} \cos\omega_3 t - \beta_{yn} \sin\omega_3 t\right) q_n^R(t) \mathbf{I} \\ &+ \sum_{n=1}^{n_r} \left(\beta_{xn} \sin\omega_3 t + \beta_{yn} \cos\omega_3 t\right) q_n^R(t) \mathbf{J} \\ &+ \sum_{n=1}^{n_r} \beta_{zn} q_n^R(t) \mathbf{K} \end{aligned} \tag{2.26}$$

The angular displacements of A relative A' are $\boldsymbol{\xi} \equiv \xi_x \mathbf{I} + \xi_y \mathbf{J} + \xi_z \mathbf{K}$, where

$$\xi_x = \sum_{n=1}^{n_r} \left[\beta_{xn} \cos\omega_3 t - \beta_{yn} \sin\omega_3 t\right] q_n^R(t) - \sum_{n=1}^{n_h} \alpha_{xn} q_n^H(t) \tag{2.27}$$

$$\xi_y = \sum_{n=1}^{n_r} \left[\beta_{xn} \sin\omega_3 t + \beta_{yn} \cos\omega_3 t\right] q_n^R(t) - \sum_{n=1}^{n_h} \alpha_{yn} q_n^H(t) \tag{2.28}$$

and

$$\xi_z = \sum_{n=1}^{n_r} \beta_{zn} q_n^R(t) - \sum_{n=1}^{n_h} \alpha_{zn} q_n^H(t) \tag{2.29}$$

2.5 Vector and Matrix Notation

To keep track of the lengthy derivation, let us use vector and matrix notation.

2.5.1 Vector of Generalized Coordinates

$$\mathbf{q}(t) = \left[\ (\mathbf{q}^H)^T(t),\ (\mathbf{q}^R)^T(t)\right]^T \tag{2.30}$$

where $\mathbf{q}^H(t) = [\ q_1^H,\ q_2^H,\ \cdots,\ q_{n_h}^H]^T$ and $\mathbf{q}^R(t) = [\ q_1^R,\ q_2^R,\ \cdots,\ q_{n_r}^R]^T$.

2.5.2 Modal Vector and Matrix of Bearing deformations

Let us define the bearing linear and angular deformation modal matrices of each housing and rotor mode in terms of modal vectors.

$$\mathbf{W}^H(\mathbf{r}_{A'}) \equiv [\mathbf{W}_1^H(\mathbf{r}_{A'}), \mathbf{W}_2^H(\mathbf{r}_{A'}), \cdots, \mathbf{W}_{n_H}^H(\mathbf{r}_{A'})] \tag{2.31}$$

$$\mathbf{W}^R(\tilde{\mathbf{r}}_A) \equiv [\mathbf{W}_1^R(\tilde{\mathbf{r}}_A), \mathbf{W}_2^R(\tilde{\mathbf{r}}_A), \cdots, \mathbf{W}_{n_R}^R(\tilde{\mathbf{r}}_A)] \tag{2.32}$$

$$\boldsymbol{\alpha}^H(\mathbf{r}_{A'}) \equiv [\boldsymbol{\alpha}_1^H(\mathbf{r}_{A'}), \boldsymbol{\alpha}_2^H(\mathbf{r}_{A'}), \cdots, \boldsymbol{\alpha}_{n_H}^H(\mathbf{r}_{A'})] \tag{2.33}$$

$$\boldsymbol{\beta}^R(\mathbf{r}_A) \equiv [\boldsymbol{\beta}_1^R(\mathbf{r}_A), \boldsymbol{\beta}_2^R(\mathbf{r}_A), \cdots, \boldsymbol{\beta}_{n_R}^R(\mathbf{r}_A)] \tag{2.34}$$

Eqn. (2.31) to (2.34) are hereafter termed linear/angular housing/rotor-bearing modal matrix for simplicity.

Then, we can define the housing-bearing-rotor modal matrix $\mathbf{B}^B(t)$, which is written in vector form in terms of housing/rotor-bearing modal matrices as

$$\mathbf{B}^B(t) = \begin{bmatrix} \mathbf{W}^H(\mathbf{r}_{A'}) & \mathbf{R}(t)\mathbf{W}^R(\tilde{\mathbf{r}}_A) \\ \boldsymbol{\alpha}^H(\mathbf{r}_{A'}) & \mathbf{R}'(t)\boldsymbol{\beta}^R(\tilde{\mathbf{r}}_A) \end{bmatrix} \tag{2.35}$$

In (2.35), $\mathbf{R}(t)$ is the coordinate transformation matrix defined in (2.3) whereas $\mathbf{R}'(t)$ is a 2 by 2 matrix that contains only the time dependent entries of $\mathbf{R}(t)$. Both of them are responsive to coordinate transformation introduced in Eq.(2.3). In addition, $\mathbf{W}^H(\mathbf{r}_A)/\mathbf{W}^R(\tilde{\mathbf{r}}_A)$ and $\boldsymbol{\alpha}^H(\mathbf{r}_A)/\boldsymbol{\beta}^R(\tilde{\mathbf{r}}_A)$ are the linear/angular housing/rotor-bearing modal matrices defined in (2.31) to (2.34). They represent the mode shapes and angular deformation of housing/rotor at the positions of bearings, which dicretize the relative motion of A' and A.

2.5.3 Matrix form of bearing deformations

With the vector notation, the linear and angular bearing deformations can be rewritten as

$$\boldsymbol{\Delta}_b \equiv (\Delta_x, \Delta_y, \Delta_z, \xi_x, \xi_y)^T = \mathbf{B}^B(t)\mathbf{q}(t) \tag{2.36}$$

In (2.36), $\mathbf{B}^B(t)$ is defined in (2.35).

2.6 Generalized Forces

2.6.1 Generalized Bearing Forces

To simplify (2.35), let us define a 5 by 5, general coordinate transformation matrix $\mathbf{T}(t)$

$$\mathbf{T}(t) = \mathbf{R}(t) \oplus \mathbf{R}'(t) \tag{2.37}$$

where $\oplus$ is the direct sum. In addition, $\mathbf{T}(t)$ is orthonormal satisfying $\mathbf{T}^T(t)\mathbf{T}(t) = \mathbf{I}$, where $\mathbf{I}$ is identity matrix. Again, $\mathbf{W}^H(\mathbf{r}_A)/\mathbf{W}^R(\tilde{\mathbf{r}}_A)$ and $\boldsymbol{\alpha}^H(\mathbf{r}_A)/\boldsymbol{\beta}^R(\tilde{\mathbf{r}}_A)$ are the linear/angular bearing deformation modal matrices of the housing part and rotor part, respectively, i.e., the linear/angular housing-bearing and rotor-bearing modal deformation matrices defined in Subsec. 2.5.2. Then we can define the housing-bearing modal matrix and rotor-bearing modal matrix as

$$\mathbf{B}^H = \begin{bmatrix} \mathbf{W}^H(\mathbf{r}_{A'}) \\ \boldsymbol{\alpha}^H(\mathbf{r}_{A'}) \end{bmatrix} \tag{2.38}$$

and

$$\mathbf{B}^R = \begin{bmatrix} \mathbf{W}^R(\tilde{\mathbf{r}}_A) \\ \boldsymbol{\beta}^R(\tilde{\mathbf{r}}_A) \end{bmatrix} \tag{2.39}$$

Then, (2.35) can be rewritten as a compact form as

$$\mathbf{B}^B(t) = \begin{bmatrix} \mathbf{B}^H & \mathbf{T}(t)\mathbf{B}^R \end{bmatrix} \tag{2.40}$$

$\mathbf{B}^B(t)$ is hereafter termed the housing-bearing-rotor modal matrix because it contains both the rotor-bearing and housing-bearing modal matrices. Two things worth noticing in (2.38), (2.39), and (2.40). First of all, since $\mathbf{B}^H$ and $\mathbf{B}^R$ are defined in the respective coordinates of the rotor and housing, they are both constants. Secondly, since $\mathbf{B}^B(t)$ is defined by means of mixture of the two coordinates, now it has time varying components which presenting the rotor is spinning with respect to the stationary housing.

Given a 5 by 5 bearing stiffness matrix $\tilde{\mathbf{K}}^B$, the generalized bearing stiffness $\mathbf{K}^B(t)$ takes the form

$$\mathbf{K}^B(t) \equiv \sum (\mathbf{B}^B(t))^T \tilde{\mathbf{K}}^B \mathbf{B}^B(t) \tag{2.41}$$

which has the period $2\pi/\omega_3$ because of the periodicity of $\mathbf{B}^B(t)$, For each bearing, the bearing forces consist of three force components and two moment components. Moreover, the bearing forces are linear combination of spring forces described by

$$\mathbf{F}_b \equiv (F_{xb}, F_{yb}, F_{zb}, M_{xb}, M_{yb})^T = -\tilde{\mathbf{K}}^B \mathbf{\Delta}_b \tag{2.42}$$

where $\tilde{\mathbf{K}}^B$ is the 5×5 stiffness matrix in physical domain. The virtual work done by the bearing forces is

$$\delta W_b = \sum \mathbf{F}_b^T \delta \mathbf{\Delta}_b = -\delta \mathbf{q}^T \mathbf{Q}_b \tag{2.43}$$

where the summation sums over all the bearings and $\mathbf{Q}_b$ is the generalized bearing force vector. Substitution of (2.36) and (2.42) into (2.43) yields $\mathbf{Q}_b = \mathbf{K}^B(t)\mathbf{q}$, where $\mathbf{K}^B(t) \equiv \sum (\mathbf{B}^B)^T(t) \tilde{\mathbf{K}}^B \mathbf{B}^B(t)$.

2.6.2 Generalized Damping Forces

For rotating machines, damping is very difficult to model accurately and effectively. If the damping model is too simple, predictions on forced response amplitude will be inaccurate. If the damping model is too complicate, it could become impractical to apply. As a compromise, the damping model used in this section assumes proportional damping and modal viscous damping factors.

For the stationary housing, Let us assume a damping force density (damping force per unit volume) as

$$\mathcal{F}^H(\hat{\mathbf{r}}, t) = -2\rho_H \sum_{n=1}^{n_H} \zeta_n^H \omega_n^H \mathbf{W}_n^H(\hat{\mathbf{r}}) \dot{q}_n^H(t) \tag{2.44}$$

where ρ_H is the density of the stationary housing, and ζ_n^H is the viscous damping factor of each housing mode. In this case, the model allows some flexibility through ζ_n^H while keeping the complexity of the model under control. The virtual work done by the damping force is

$$\int_{V_H} \left(\mathcal{F}^H \cdot \delta \mathbf{R}_P^H \right) dV_H = -2 \sum_{n=1}^{n_H} \zeta_n^H \omega_n^H \dot{q}_n^H(t) \delta q_n^H(t) \tag{2.45}$$

where (2.6) have been used.

For the rotating part, there are two types of damping: internal damping and external damping. For asymmetric rotors, external damping is very difficult to model accurately and remains largely open. Therefore, we will only focus on internal damping only. For internal damping, let us assume

$$\mathcal{F}^R(\tilde{\mathbf{r}},t) = -2\rho_R \sum_{n=1}^{n_R} \zeta_n^R \omega_n^R \mathbf{W}_n^R(\tilde{\mathbf{r}}) \cdot q_n^R(t) \tag{2.46}$$

where ρ_R is the density of the rotor, and ζ_n^R is the internal viscous damping factor of each rotor mode. The virtual work done by the internal damping force is

$$\int_{V_R} \left(\mathcal{F}^R \cdot \delta\mathbf{R}_P^R\right) dV_R = -2\sum_{n=1}^{n_R} \zeta_n^R \omega_n^R \dot{q}_n^R(t)\delta q_n^R(t) \tag{2.47}$$

where (2.11) have been used.

Finally, the virtual work done by all the damping forces is arranged in a matrix form.

$$\delta W_d = -\delta\mathbf{q}^T \mathbf{D}\dot{\mathbf{q}} \tag{2.48}$$

where

$$\mathbf{D} = 2 \times \text{diag}\left[\zeta_1^H\omega_1^H, \ldots, \zeta_{n_H}^H\omega_{n_H}^H, \zeta_1^R\omega_1^R, \ldots, \zeta_{n_R}^R\omega_{n_R}^R\right] \tag{2.49}$$

2.7 Equations of Motion

With the kinetic energy, potential energy, and generalized bearing forces of the rotor-bearing-housing system, one can derive the equations of motion through use of Lagrangian equations. The resulting equation of motion is

$$\ddot{\mathbf{q}} + [\mathbf{G} + \mathbf{D}]\dot{\mathbf{q}} + \left[\mathbf{K} + \mathbf{K}^B(t)\right]\mathbf{q} \;\; = \;\; 0 \tag{2.50}$$

In (2.50),

$$\mathbf{G} = \begin{bmatrix} \mathbf{0} & \mathbf{0} \\ \mathbf{0} & \mathbf{G}_{22}(n,m) \end{bmatrix} \tag{2.51}$$

with $\mathbf{G}_{22}(n,m) = 2\omega_3 g_{nm}$ given in (2.18) and $\mathbf{D}$ is defined in (2.49). Also,

$$\mathbf{K} = \begin{bmatrix} \boldsymbol{\omega}^H & \mathbf{0} \\ \mathbf{0} & \boldsymbol{\omega}^R - \omega_3^2\mathbf{K}_\lambda(n,m) \end{bmatrix} \tag{2.52}$$

where $\boldsymbol{\omega}^H \equiv \text{diag}\left[\left\{\omega_1^H\right\}^2, \left\{\omega_2^H\right\}^2, \ldots, \left\{\omega_{n_h}^H\right\}^2\right]$, $\boldsymbol{\omega}^R = \text{diag}\left[\left\{\omega_1^R\right\}^2, \left\{\omega_2^R\right\}^2, \ldots, \left\{\omega_{n_r}^R\right\}^2\right]$, and $\mathbf{K}_\lambda(n,m) = \lambda_{nm}$ defined in (2.15). $\mathbf{K}^B(t)$ in (2.50) is symmetric and has periodic coefficients with the spin speed ω_3.

2.7.1 Convergence Rate

The essence of this mathematical model is component-mode synthesis, in which the rotor and housing are each treated as an individual component. Therefore, the shape functions used to discretize each component will affect convergence rate of the model.

In this model, natural boundary conditions are imposed on each component at the bearings to obtain mode shapes as the shape functions. Such an approach provides great convenience, because mode shapes form a complete set of admissible functions. Moreover, this approach allows a simpler formulation of the centrifugal softening, gyroscopic effects, and bearing deformation in general. Nevertheless, a trade-off is the convergence rate, because the natural boundary conditions may not be satisfied after the components are assembled.

When modelling flexible multi-body systems, Meirovitch [40] points out that convergence can suffer if the admissible functions (mode shapes in our case) of substructures are not chosen properly. The poor convergence results from the fact that a finite linear combination of the admissible functions is not able to satisfy the natural boundary conditions. As a result, a relatively large numbers of degrees of freedom are needed for a reasonable convergence.

To prevent poor convergence rate, we use the concept of *balanced* and *unbalanced modes* [27] to minimize the number of mode shapes that are capable of satisfying all natural boundary conditions. (Since *unbalanced modes* include both unbalanced inertia forces and moments, their linear combination comprises the minimum number of mode shapes to satisfy all possible natural boundary conditions.) We also conducted a convergence test to ensure that the equations of motion have a decent convergence rate.

Chapter 3

PARAMETRIC RESONANCE

There are two things worth noting regarding the equation of motion (2.50). First, not all rotor modes need to be retained in (2.50). According to Kim et al. [27], presence of bearings may cause some rotor modes to coupled with the bearings, while other modes may not [27]. If a rotor mode presents unbalanced inertia forces or moments as the rotor vibrates, the rotor mode is called an *unbalanced mode*. The unbalanced inertia forces or moments will result in a resultant deforming the bearings. Therefore, only *unbalanced modes* will be coupled to the housing via the bearings, and only *unbalanced modes* need to be retained in (2.50).

Second, instability of the rotor-bearing-housing system can be found analytically or numerically. For analytical solutions, one can use any perturbation methods, such as the method of multiple scales, to (2.50). Since $\mathbf{K}^B(t)$ is symmetric in (2.50), the rotor-bearing-housing system will present instability in the form of combination resonances of the sum type, if the gyroscopic matrix $\mathbf{G}$ and the damping matrix $\mathbf{D}$ are not present. Moreover, the range of spin speed in which the combination resonance occurs can be predicted analytically in terms of the coefficients in $\mathbf{K}$ and $\mathbf{K}^B(t)$.

The instability can also be found by numerically integrating the equation of motion (2.50). For example, (2.50) can be written in a state-space form and integrated over one period of time to find the fundamental matrix. If any eigenvalue of the fundamental matrix has a magnitude greater than unity, the rotor-bearing-housing system is unstable.

To demonstrate the instability, we perform two numerical examples along with analytical analysis. The first one is *Axisymmetric Rotor* and the second one is *Cyclic Symmetric Rotor*.

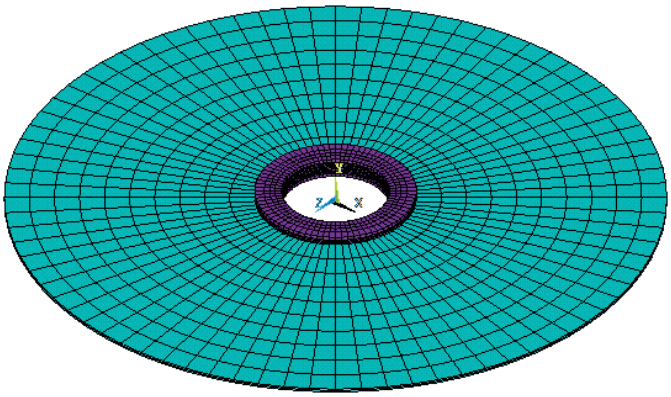

Figure 3.1: FEA Model: Axisymmetric Rotor

3.1 Example 1: Axisymmetric Rotor

In this example, the rotor is a circular disk with a rigid hub; see Fig. 3.1. The disk has outer diameter of 152.8 mm, inner diameter of 37.28 mm, and thickness of 0.79 mm. The disk is elastic with Young's modulus 280 GPa and Poisson's ratio of 0.33 and has density of 2700 kg/m^3. The disk has a rigid hub at the center with outer diameter of 37.28 mm, inner diameter of 25 mm and thickness of 4.74 mm. Also, the hub is symmetric with respect to the disk plane. Based on the rotor geometry, gyroscopic term will be negligible, i.e., $\mathbf{G} = \mathbf{0}$. Moreover, damping is assumed to be zero, i.e., $\mathbf{D} = \mathbf{0}$, in this example to serve as a reference.

The housing consists of a square plate and a shaft; see Fig. 3.2. The length and thickness of the square plate are 180 mm and 3.95 mm, respectively. The plate is elastic with Young's modulus 280 GPa and Poisson's ratio of 0.33 and has density of 2700 kg/m^3. Moreover, the square plate is simply supported at the four corners. The shaft is rigid and is located at the center of the plate. The shaft has outer diameter of 25 mm and length of 5.925 mm.

The rotor and housing are connected via two ball bearings. The outer race of the upper bearing is located at 0.79 mm above the disk plane on the rigid hub. The outer race of the lower bearing is located at 0.79 mm below the disk plane on the rigid hub. The inner races of the bearings are located on the shaft of the housing. Moreover, the bearing stiffness

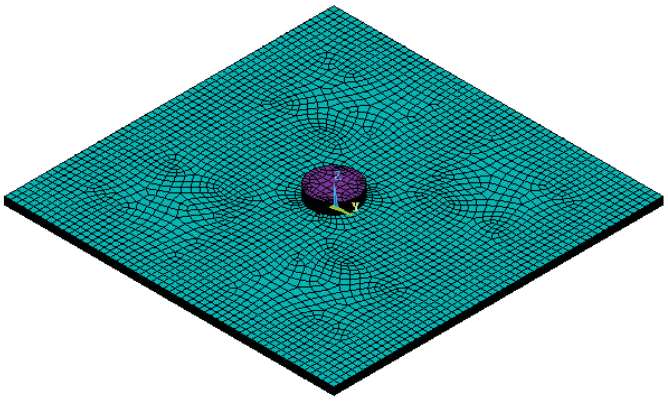

Figure 3.2: FEA Model: Housing

coefficients are given as

$$\tilde{\mathbf{K}}^B = \text{diag}\left[2.16 \times 10^7, 2.16 \times 10^7, 5.76 \times 10^6, 58.5, 58.5\right] \tag{3.1}$$

where the coefficients in (3.1) are in MKS units.

To obtain natural frequencies ω_n^R and mode shapes $\mathbf{W}_n^R(\mathbf{r})$ of the rotor, we first note that the rotor is subjected to free boundary conditions. Therefore, the rotor will present both rigid-body modes and elastic modes. The rigid-body modes are obtained analytically (cf. (2.10)), while the elastic modes are obtained via a finite element analysis in ANSYS. The elastic modes basically appear as disk vibration with nodal diameters and nodal circles. A quick calculation via [27] indicates that only zero- and one-nodal-diameter modes are unbalanced modes.

For this example, the following modes are retained in (2.50): (a) three rigid-body translational modes of the rotor along the x, y and z axes, (b) two rigid-body rocking modes of the rotor around x and y axes, (c) unbalanced modes of the rotors including zero- and one-nodal-diameter modes whose natural frequencies are lower than 4000 Hz, and (d) 14 elastic modes from the housing.

To predict the stability of the rotor-bearing-housing system, the equation of motion (2.50) is rewritten in a state-space form and numerically integrated over a period of time to obtain its fundamental matrix. If any eigenvalue has a magnitude greater than 1, the

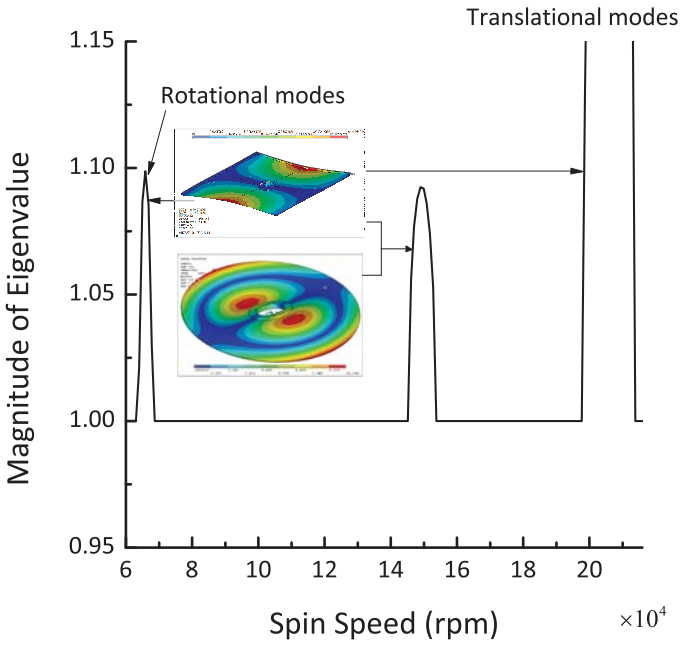

Figure 3.3: Parametric Resonances of the Axisymmetric Rotor

system is unstable. Figure 3.3 shows the largest magnitude of all eigenvalues from the fundamental matrix. As shown in Fig. 3.3, there are three instability zones and each instability zone corresponds to a combination resonance of the sum type. Each combination resonance involves vibration mode from the housing and a vibration mode from the rotor. The vibration mode from the housing is the same for all instability zones. As far as the rotor modes, the first and the last instability zones are dominated by rigid-body rocking modes and rigid-body translational modes, respectively. The second instability zone is dominated by a one-nodal-diameter unbalanced mode with natural frequency of 1325.90 Hz. For the speed range shown in Fig. 3.3, the stiffness matrix $\mathbf{K}$ remains positive definite. If the spin speed increases further, $\mathbf{K}$ will lose its positive definiteness (cf. (2.52)) resulting in an divergence instability.

For this example and its instability, there are several issues worth further exploration. First, equation of motion of an axisymmetric rotor-bearing-housing system can be written in a different form than (2.50). Since the spinning rotor is axisymmetric, one can use a

ground-based observer to describe motion of the spinning axisymmetric rotor. By doing so, Tseng et al. [5] shows that equation of motion of an axisymmetric rotor-bearing-housing system can take the form of ordinary differential equations with *constant* coefficients, i.e.,

$$\ddot{\mathbf{q}}' + \mathbf{G}'\dot{\mathbf{q}}' + \mathbf{K}'\mathbf{q}' = \mathbf{0} \tag{3.2}$$

where $\mathbf{q}'$ is a vector of generalized coordinates from the ground-based observer only, and $\mathbf{G}'$ and $\mathbf{K}'$ are corresponding constant gyroscopic and stiffness matrices observed in the ground-based coordinates. (Note that $\mathbf{G} \neq \mathbf{G}'$ and $\mathbf{K} \neq \mathbf{K}'$.) For systems with an axisymmetric rotor, equations of motion (2.50) and (3.2) are equivalent. One equation of motion can be derived from the other, if a coordinate transformation is introduced between the rotor-based coordinates and the ground-based coordinates [1]. Such transformation has also been discussed in [41].

Second, the stability predicted from (2.50) and (3.2) should be identical. According to Huseyin [42], the stability of the rotor-bearing-housing system can be predicted through use of the characteristic equation of (3.2). Let λ be eigenvalues of the system, the characteristic equation of (3.2) can be written as a function of λ^2, i.e.,

$$f(\lambda^2) \equiv \left|-\lambda^2 - i\lambda\mathbf{G}' + \mathbf{K}'\right| = 0 \tag{3.3}$$

Complex λ in (3.3) indicates instability of the system. After we transform the equation of motion to the ground-based observer, we have also calculated λ according to (3.3). We observe that λ becomes complex at the same spin speed, where the rotor-bearing-housing system experiences instability as shown in Fig. 3.3. For example, Fig. 3.4 shows the root loci λ^2 of the system after transformed to the ground-based formulation from around 58000 rpm to 60500 rpm. As seen in Fig. 3.4, root loci λ^2 disappears between 59000 rpm to 60500 rpm, which is corresponding to the first instability zone in Fig. 3.3 and has roughly the same width. Therefore, the stability predicted from (2.50) and (3.2) are indeed the same.

Third, instability does appear in gyroscopic systems under certain conditions. Meirovitch [43] shows that eigenvalues of undamped gyroscopic systems are purely imaginary implying no instability. That conclusion, however, is achieved under the assumption that the stiffness

[1] Please refer to Appendix A for detail

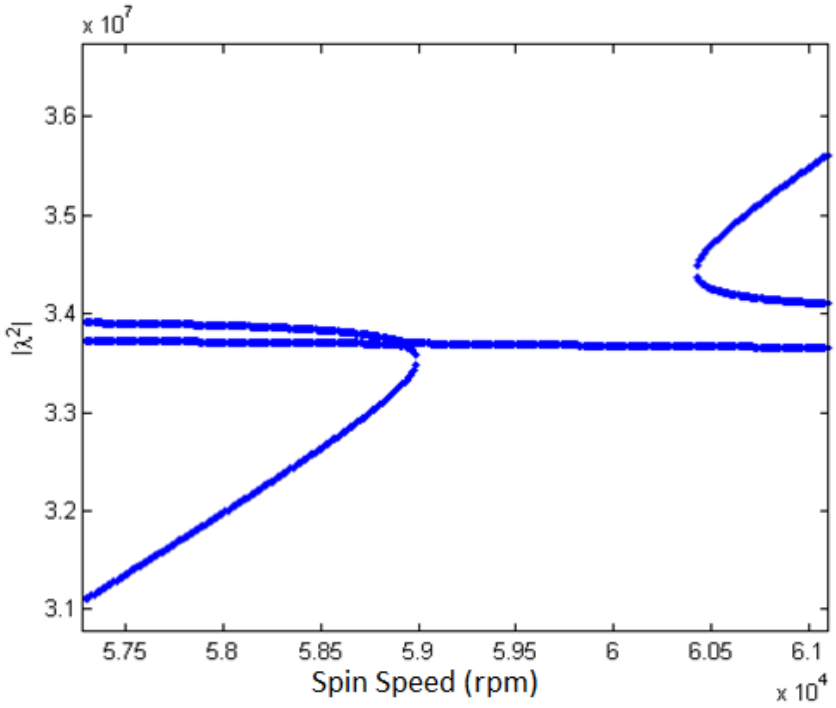

Figure 3.4: Root Loci of λ^2 v.s. ω_3

matrix $\mathbf{K}'$ is positive definite. Huseyin [42] indicates that the instability can occur when a gyroscopic system loses its positive definiteness. According to our calculation, all instabilities in Fig. 3.3 occur after the stiffness matrix $\mathbf{K}'$ in (3.2) has lost its positive definiteness. This finding is consistent with the stability predictions by Huseyin [42] and Meirovitch [43].

3.2 Example 2: Cyclic Symmetric Rotor

In this example, the rotor is a circular disk with four radial slots evenly spaced in the circumferential direction; see Fig. 3.5. The slotted disk also has a rigid hub. The disk has the same dimensions and material as in Example 1, except that the slots are 4.8 mm wide and 52 mm long. The housing remains the same, and the rotor is mounted on the housing through the same two bearings. Again, there is no gyroscopic term, i.e., $\mathbf{G} = \mathbf{0}$. Both undamped and damped systems are considered.

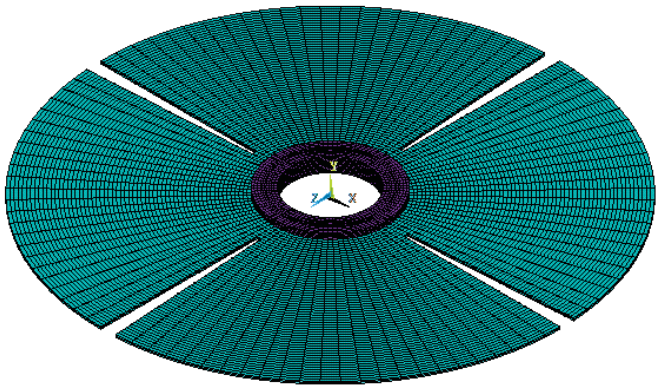

Figure 3.5: FEA Model: Cyclic Symmetric Rotor

3.2.1 Undamped System

In this part of the example, damping term is assumed to be zero, i.e., $\mathbf{D} = \mathbf{0}$. For the rotor, its rigid-body modes are calculated analytically. For the rotor's elastic modes, their natural frequencies ω_n^R and mode shapes $\mathbf{W}_n^R(\mathbf{r})$ are obtained via ANSYS. For this example, the following modes are retained in (2.50): (a) three rigid-body translational modes of the rotor along the x, y and z axes, (b) two rigid-body rocking modes of the rotor around x and y axes, (c) unbalanced modes of the rotors with natural frequencies lower than 4000 Hz, and (d) 14 elastic modes from the housing. Please note that the unbalanced modes for the cyclic symmetric rotor are significantly different from those of the axisymmetric rotor in Example 1. Altogether, 34 modes are retained in (2.50) for the cyclic symmetric rotor-bearing-housing system due to the large number of unbalanced modes under 4000 Hz resulting from the slots.

To ensure that enough number of modes is retained, we check the convergence by considering a stationary rotor with $\omega_3 = 0$. Theoretically, the solution of (2.50) will converge to the exact solution when infinitely many modes are retained. When $\omega_3 = 0$, the exact solution can be approximated fairly well by using a finite element analysis of the entire rotor-bearing-housing system. Table 3.1 compares the first fourteen natural frequencies between these two sets of solutions. The frequencies in the column labeled "ANSYS" are

Table 3.1: Natural Frequency (Hz): ANSYS vs. MATLAB®

Mode	ANSYS	MATLAB®	% Relative Error
1	148.55	149.41	0.58
2	148.55	149.41	0.58
3	294.22	296.10	0.64
4	313.30	313.22	0.03
5	423.82	423.99	0.04
6	423.82	423.99	0.04
7	452.99	452.89	0.00
8	440.45	456.42	3.63
9	472.59	472.59	0.02
10	925.25	928.78	0.38
11	925.27	929.01	0.40
12	1104.70	1109.39	0.42
13	1104.70	1109.39	0.42
14	1138.70	1139.08	0.03

natural frequencies predicted from the finite element analysis of the entire rotor-bearing-housing system with $\omega_3 = 0$. The frequencies in the column labeled "MATLAB®" are natural frequencies predicted from (2.50) with 34 modes retained. According to Table 3.1, the largest relative error between these two solutions is 3.63%. Therefore, 34 modes are enough to ensure convergence in predicting an accurate response of the cyclic symmetric rotor-bearing-housing system.

When the spin speed $\omega_3 \neq 0$, equation of motion (2.50) can be analyzed via the method of multiple scales to predict the speed range in which combination resonance may occur. Table 3.2 shows the first four predicted speeds ω and their bandwidth σ, where the combination resonance occurs at $\omega - \sigma/2 < \omega_3 < \omega + \sigma/2$.

At the same time, (2.50) can be numerically integrated as explained above. Figure 3.6

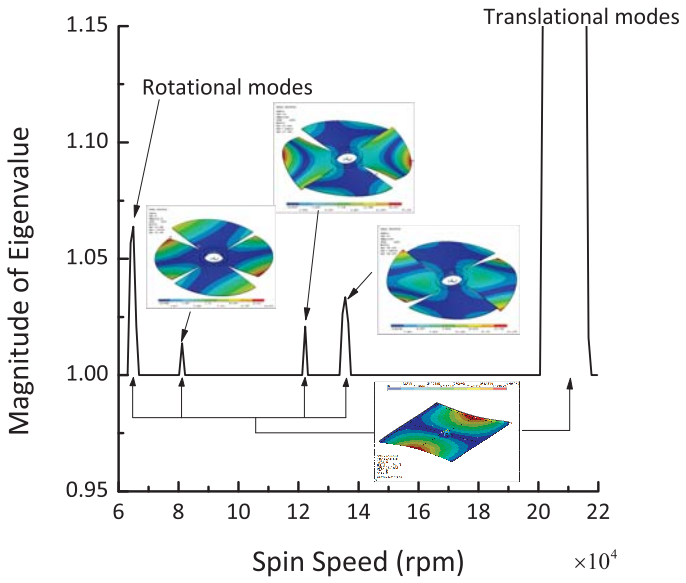

Figure 3.6: Parametric Resonances of Cyclic Symmetric Rotor

shows the largest magnitude of eigenvalues from the fundamental matrix. (The numerical integration was only performed within 64,000 rpm to 135,000 rpm with resolution of 100 rpm.) As shown in Fig. 3.6, there are five instability zones. The five instability zones basically have the same mechanism as those shown in Example 1. Each instability zone results from a combination resonance between a housing mode and a rotor mode. The housing mode involved is the same from Example 1. The first instability zone involves rigid-body rocking of the rotor. The second, third, and fourth instability zones each involves an unbalanced mode of the rotor. Finally, the last instability zone involves rigid-body translation in the radial (x and y) directions.

There are several things worth discussing. First, the predictions from the method of multiple scales (cf. Table 3.2) are quite accurate. According to Fig. 3.6, the first four instability zones center around 64,000 rpm, 81,000 rpm, 122,000 rpm, and 135,000 rpm. These predictions, in general, agree well with those shown in Table 3.2.

Second, combination resonances resulting from the rigid-body translation and rocking modes are almost identical for the axisymmetric and cyclic symmetric rotors. Combination

Table 3.2: Instabilities: the Method of Multiple Scales

Instabilities	Speed ω (rpm)	Bandwidth σ (rpm)
1	64075.78	1193.66
2	81426.85	311.12
3	122565.22	3761.47
4	135695.50	629.20

resonances resulting from the unbalanced modes, however, are very different. For the axisymmetric rotor, only one unbalanced mode with a natural frequency of 1325.90 Hz leads to an instability zone. For the cyclic symmetric rotor, it has three unbalanced modes under 4000 Hz (i.e., 419.24 Hz, 1080.30 Hz, and 1272.40 Hz, respectively). These unbalanced modes lead to the second, third and fourth instability zones shown in Fig. 3.6.

3.2.2 Effects of Damping

To examine how damping affects the instability, let us incorporate the damping terms $\mathbf{D} \neq \mathbf{0}$ into the equation of motion (2.50) in two steps.

In the first step, the rotor damping is absent (i.e., $\zeta^R = 0$), whereas the housing damping ζ^H is assumed constant. Figure 3.7 is the blowup of the fourth instability zone in Fig. 3.6 in the interval of 136,000 to 152,000 rpm after damping of the housing modes is included. As seen in Fig. 3.7, the width of the instability zone increases as the viscous damping factor of the housing increases (following the arrow). In other words, the housing damping has a destabilizing effect.

In the second step, the viscous damping of the housing ζ^H remains the same, but the rotor damping is introduced such that $\zeta^R = 0.05\zeta^H$. Figure 3.8 is the same blowup of the fourth instability zone with damping of both the housing and rotor included. As seen in Fig. 3.8, the width of the instability zone decreases as the rotor damping increases. In other words, the rotor damping has a stabilizing effect.

The numerical results shown in Figure 3.7 and Figure 3.8 may seem somewhat counter-

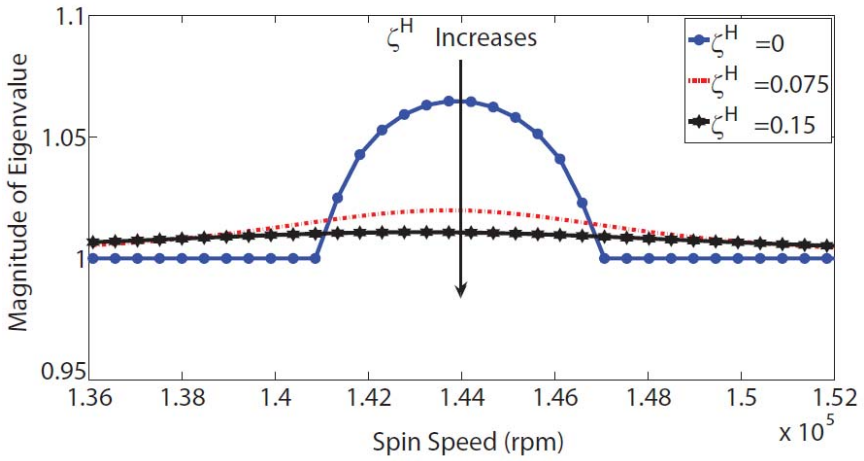

Figure 3.7: Effect of Housing Damping on Instability Zone

intuitive. There are, however, theoretical supports that housing damping could destabilize the system and rotor damping could do the opposite. Let us investigate this in more detail as follows.

According to Eq. (2.49), the damping matrix $\mathbf{D}$ has non-uniform diagonal values resulting from different natural frequencies and viscous damping factors of the housing and rotor modes. The effect of non-uniform damping on parametrically excited systems, whose equations of motion are similar to Eq. (2.50), is particularly intriguing [44, 45, 46]. According to [44, 45], non-uniform damping could worsen combination resonances by increasing the width of instability zones under certain circumstances. The particular circumstances depend highly on the structure of the periodic matrices as well as the damping ratio of each mode. Therefore, effects of non-uniform damping may vary significantly from one problem to another.

On the other hand, this phenomenon can be viewed from a different perspective. If there exists a coordinate transformation such that Eq. (2.50) can be transformed into an equation with constant coefficients (as in Example 1), it would take the form

$$\ddot{\mathbf{q}}' + [\mathbf{G}' + \mathbf{D}'_R + \mathbf{D}'_H]\dot{\mathbf{q}}' + [\mathbf{K}' + \mathbf{S}'_R]\mathbf{q}' = \mathbf{0} \tag{3.4}$$

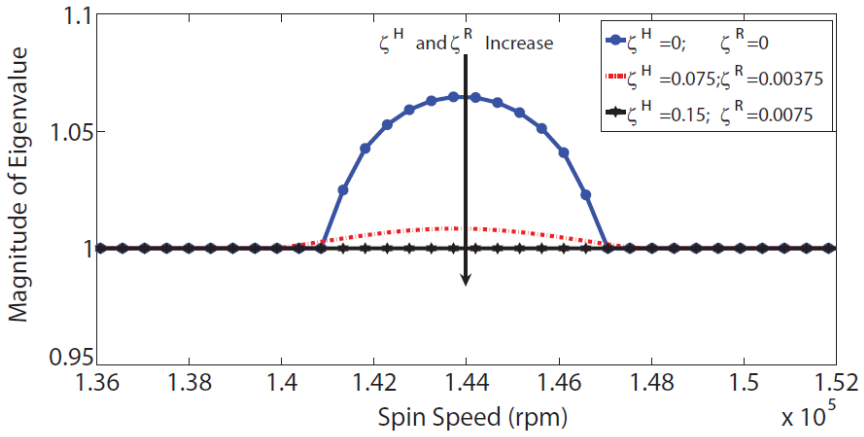

Figure 3.8: Effect of Housing and Rotor Damping on Instability Zone

In (3.4) $\mathbf{D}'_R$ and $\mathbf{S}'_R$ are constant damping and circulatory matrices resulting from the damping of the rotor modes, whereas $\mathbf{D}'_H$ results from the damping of the stationary housing. Equation (3.4) is a standard form of damped gyroscopic systems with non-conservative forces [47, 48, 49, 50].

For such systems, damping can destabilize the otherwise stable gyroscopic systems, and yet combination of damping and circulatory matrices can do the opposite [47, 49, 50]. In the case of asymmetric rotors, such a coordinate transformation may not even exist, and Eq. (3.4) is not necessarily achievable. Nonetheless, the criteria provided in [47, 49, 50] are still good guidelines to investigate the qualitative behavior of Eq. (2.50) when damping is present.

Based on the results from [47, 49, 50], the presence of housing damping will introduce only $\mathbf{D}'_H$, which tends to destabilize the coupled rotor-bearing-housing system. This is exactly what the numerical results show in Fig. 3.7. In contrast, the damping of the rotor modes contributes to both damping and circulatory matrices in (3.4), which can stabilize the coupled rotor-bearing-housing system. This is exactly what the numerical results show in Fig. 3.8. Therefore, the numerical results in Fig. 3.7 and Fig. 3.8 are in line with theoretical predictions from the literature [47, 49, 50].

Chapter 4

FREE RESPONSE

As stated in Chapter 3, the equations of motion has instability when spin speed is extremely high. The response at conventional spin speed is generally stable. Moreover, response of the system at conventional spin speed is more important in practical use.

4.1 Rotor-Based Response

In this section, we predict the rotor response for a rotor-based observer by analyzing the equation of motion (2.50) theoretically. We also confirm the prediction by solving (2.50) numerically using the benchmark example. The benchmark model is the same as that in Sec. 3.2.

4.1.1 Theoretical Analysis

In the equation of motion (2.50), the gyroscopic matrix $\mathbf{G}$ and centrifugal matrix $\mathbf{K}_\lambda$ are determined solely by the mode shapes of the rotor. Therefore, it is the periodic bearing stiffness term $\mathbf{K}^B(t)$ in (2.50) that describes the coupling effects between the rotor and housing. By expanding (2.41), $\mathbf{K}^B(t)$ can be arranged into a block matrix form

$$\mathbf{K}^B(t) = \begin{bmatrix} \mathbf{\Lambda} & \mathbf{\Phi} \\ \mathbf{\Psi} & \mathbf{\Xi} \end{bmatrix} \tag{4.1}$$

In particular, each block can be written in index notation

$$\Lambda_{ij} = (\mathbf{B}_i^H)^T \tilde{\mathbf{K}}^B \mathbf{B}_j^H \tag{4.2}$$

$$\Phi_{ij} = (\mathbf{B}_i^H)^T \tilde{\mathbf{K}}^B \mathbf{T}(t) \mathbf{B}_j^R \tag{4.3}$$

$$\Psi_{ij} = (\mathbf{B}_i^R)^T \mathbf{T}^T(t) \tilde{\mathbf{K}}^B \mathbf{B}_j^H \tag{4.4}$$

and

$$\Xi_{ij} = (\mathbf{B}_i^R)^T \mathbf{T}^T(t) \tilde{\mathbf{K}}^B \mathbf{T}(t) \mathbf{B}_j^R \tag{4.5}$$

where $\mathbf{B}_i$ is the i-th column of $\mathbf{B}^H$ and $\mathbf{B}^R$ defined in (2.38) and (2.39), and the superscripts R and H indicate if $\mathbf{B}_i$ results from the rotor or the housing, respectively. Also, $\mathbf{T}(t)$ is the coordinate transformation matrix defined in (2.37). For many practical applications, the bearing stiffness $\tilde{\mathbf{K}}^B$ is symmetric and so is (4.1), which implies that $\mathbf{\Phi} = \mathbf{\Psi}^T$.

Equation (4.2) indicates that $\mathbf{\Lambda}$ is constant and thus irrelevant to the periodicity of $\mathbf{K}^B(t)$. Furthermore, (4.5) shows that whether or not $\mathbf{\Xi}$ is periodic explicitly depends on $\tilde{\mathbf{K}}^B$ because $\mathbf{T}^T(t)$ and $\mathbf{T}(t)$ may cancel each other after multiplying with $\tilde{\mathbf{K}}^B$. For certain types of bearings, $\tilde{\mathbf{K}}^B$ has a specific structure such that $\mathbf{T}(\mathbf{t})^T\tilde{\mathbf{K}}^B\mathbf{T}(\mathbf{t})$ ends up being constant. For example, when $\tilde{\mathbf{K}}^B$ is from a ball bearing or hydrodynamic bearing, $\mathbf{T}(\mathbf{t})^T\tilde{\mathbf{K}}^B\mathbf{T}(\mathbf{t})$ is constant and thus $\mathbf{\Xi}$ has no contribution to the periodicity either.

In contrast, (4.3) indicates that $\mathbf{\Phi}$ is always periodic because of $\mathbf{T}(t)$. Moreover, $\mathbf{\Phi}$ results from bearing deformation matrices of the housing and rotor or the housing-bearing and rotor-bearing modal matrices (i.e., $\mathbf{B}^H$ and $\mathbf{B}^R$). In other words, the relative motion between the housing and rotor always introduces the periodicity of $\mathbf{K}^B(t)$ regardless of types of bearings.

To better explain the physics, $\mathbf{T}(t)$ in (2.37) can further be written in the form of a matrix exponential function, i.e.,

$$\mathbf{T}(t) = \exp[(\mathbf{\Theta} \oplus \mathbf{\Theta}')t] \tag{4.6}$$

where $\exp[\bullet]$ defines the matrix exponent and

$$\mathbf{\Theta} = \begin{bmatrix} 0 & -\omega_3 & 0 \\ \omega_3 & 0 & 0 \\ 0 & 0 & 0 \end{bmatrix}; \quad \mathbf{\Theta}' = \begin{bmatrix} 0 & -\omega_3 \\ \omega_3 & 0 \end{bmatrix} \tag{4.7}$$

are two gyroscopic matrices arising from the two coordinate transformation matrices $\mathbf{R}(t)$ and $\mathbf{R}'(t)$ defined in (2.37). Substitution of (4.6) into (4.3) then leads to

$$\Phi_{ij} = (\mathbf{B}_i^H)^T\tilde{\mathbf{K}}^B \exp[(\mathbf{\Theta} \oplus \mathbf{\Theta}')t]\mathbf{B}_j^R \tag{4.8}$$

In (4.8), there are several things worth further discussion. First of all, when the rotor is at rest, i.e., $\omega_3 = 0$, Φ_{ij} is a constant matrix. This occurs because $\mathbf{\Theta}$ and $\mathbf{\Theta}'$ in (4.7)

are zero causing $\exp[(\boldsymbol{\Theta} \oplus \boldsymbol{\Theta}')t]$ to be an identity matrix. Moreover, the rotor-based response and ground-based response are identical sharing the same natural frequencies of the coupled rotor-bearing-housing system. Naturally, these natural frequencies are governed by frequency components of the rotor and housing as well as the bearing coupling effect (i.e., time-independent part of $\mathbf{K}^B(t)$). As the coupled rotor-bearing-housing system vibrates, each vibration mode will consist of simultaneous rotor motion and housing motion. Some of these modes will be dominated by rotor response, and they will be called "rotor-dominant modes" for the rest of the paper. A rotor-dominant mode has a natural frequency $\omega^{(R)}$, where R indicates that rotor is the dominant component and the pair of parentheses indicates that the vibration mode encompasses the entire rotor-bearing-housing system. (Note that the rotor-dominant modes are not the rotor modes in (2.11).) For the rotor-dominant modes, their rotor response discretized in (2.11) in terms of $q_n^R(t)$ will have a strong component of $e^{j\omega^{(R)}t}$. In contrast, their housing response discretized in (2.7) in terms of $q_n^H(t)$ will be much smaller.

On the contrary, other coupled rotor-bearing-housing modes will be dominated by housing response, and they will be called "housing-dominant modes" for the rest of the paper. A housing-dominant mode has a natural frequency $\omega^{(H)}$, where H indicates that housing is the dominant component and the pair of parentheses indicates that the vibration mode encompasses the entire rotor-bearing-housing system. (Again, please note that the housing-dominant modes are not the housing modes in (2.7).) For the housing-dominant modes, their housing response discretized in (2.7) in terms of $q_n^H(t)$ will have a strong component of $e^{j\omega^{(H)}t}$. In contrast, their rotor response discretized in (2.11) in terms of $q_n^R(t)$ will have a smaller response.

When the rotor spins at low speed, the time-dependent part of $\Phi_{ij}(t)$ starts to appear in the form of the two gyroscopic matrices in (4.7) coupling every rotor mode and housing mode. Since the spin speed is low, $\Phi_{ij}(t)$ can be treated as a perturbation to the stationary case of $\omega_3 = 0$. Perturbation solutions developed in [51] can then be used to predict response of (2.50). Now let us consider a housing-dominant mode with response $e^{j\omega^{(H)}t}$ when $\omega_3 = 0$. As the rotor spins, the product of $\mathbf{K}^B(t)\mathbf{q}$ in (2.50) and use of [51] will lead to a modal response $e^{j\left(\omega^{(H)} \pm \omega_3\right)t}$ in the rotor modes $q_n^R(t)$.

Figure 4.1: Mode Shapes of Elastic Modes

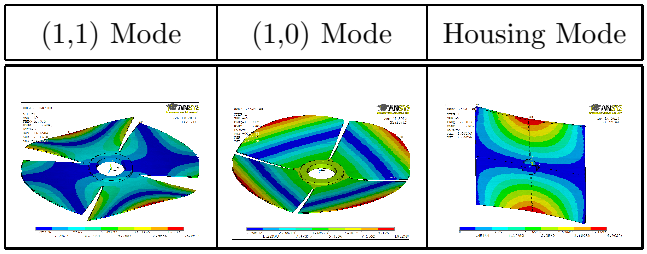

This implies that rotor modes will see strong frequency components of

$$\omega^H \pm \omega_3 \quad \text{for} \quad q_n^R(t) \tag{4.9}$$

Similarly, the product of $\mathbf{K}^B(t)\mathbf{q}$ in (2.50) will generate $e^{j(\omega^R \pm \omega_3)t}$ for modal response $q_n^H(t)$ of the housing. This implies that housing modes will see strong frequency components of

$$\omega^R \pm \omega_3 \quad \text{for} \quad q_n^H(t) \tag{4.10}$$

These phenomena in (4.9) and (4.10) are termed *gyroscopic splitting* in this paper.

4.1.2 Numerical Study

To demonstrate this gyroscopic splitting phenomena, (2.50) is solved numerically for the benchmark numerical example. The natural frequencies ω_n^R and mode shapes $\mathbf{W}_n^R(\tilde{\mathbf{r}})$ of the rotor are obtained via a finite element analysis in ANSYS by the same manner as we did in the numerical example Cyclic Symmetric Rotor in Sec. 2, Chapter 3. Similarly, the rotor is subjected to free boundary conditions. Therefore, the rotor will also present both rigid-body modes and elastic modes.

A quick calculation via [27] indicates that phase indices $n = 1$, $n = 3$, and $n = 4$ modes are unbalanced modes, which will be coupled to the housing vibrations and therefore will be included. All the other elastic modes of the rotor will not be coupled to the housing.

The following 10 representative modes are retained in (2.50) for this example: (a) three rigid-body translational modes of the rotor along the x, y and z axes, (b) two rigid-body

rocking modes of the rotor around x and y axes, (c) a pair of one-nodal-diameter one-nodal-circle modes ($n = 1$ and $n = 3$) of the rotor with repeated natural frequencies (thereafter denoted as (1,1) modes), (d) one zero-nodal-diameter one-nodal-circle mode ($n = 4$) of the rotor with a distinct natural frequency (thereafter denoted as (1,0) mode), and (e) a pair of modes from the housing with repeated natural frequencies. Figure 4.1 shows the mode shapes of all elastic modes included.

The numerical scheme used is $ODE45$ in MATLAB®, which used the fourth and fifth order Runge-Kutta formulas. The absolute and relative errors are 10^{-6} and 10^{-9}, respectively. A set of unit initial displacements is given to both housing modes, and a time series of free response is obtained by solving (2.50) using $ODE45$. Also, a fast Fourier transform (FFT) is applied to the time series to obtain corresponding frequency response.

Two rounds of simulations are conducted. The first round of simulations is for the case of $\omega_3 = 0$ as a reference. In this case, coefficients of (2.50) are constant. Free response of a set of ordinary differential equations with constant coefficients can be obtained by solving for the corresponding eigenvalues. Table 4.1 shows all eigenvalues of (2.50) when $\omega_3 = 0$, which correspond to the natural frequencies of coupled rotor-bearing-housing modes. In particular, there are eight rotor-dominant modes and two housing-dominant modes. Inspection of eigenvectors confirms that the rotor-dominant modes have very little housing vibration. Similarly, the housing-dominant modes have very little rotor vibration. There are a couple of things worth noting. First, all coupled rotor-bearing-housing modes are repeated except the (1,0) mode and out-of-plane translation mode. Second, unit initial conditions $q^H_{1H}(0) = q^H_{2H}(0) = 1$ will theoretically excite all coupled rotor-bearing-housing modes.

Figure 4.2 shows the FFT of the free responses of a few representative rotor and housing modes. The response can be classified into three different groups. The first group is q^H_{nH} represented by the dash line. This is the modal response from a housing mode. The second group is q^R_{nr} represented by three solid lines. These are frequency response from three representative rotor modes: one rigid-body rocking mode, one in-plane translational mode, and one (1,1) mode. These modes all have a significant in-plane displacement component during in-plane translation or rocking motion. These modes are also all repeated modes. The third group is q^R_{nd}, represented by two dash-dotted lines. They are modal response

Table 4.1: Natural Frequency of Coupled Rotor-Bearing-Housing Modes, $\omega_3 = 0$

Mode Number	Dominant Part	Dominant Shape	Frequency (Hz)
1,2	Rotor	Rocking	184.18
3	Rotor	(1,0)	316.66
4,5	Housing	1 nodal line	937.04
6,7	Rotor	(1,1)	1192.6
8	Rotor	Out-of-plane translation	4072.51
9,10	Rotor	In-plane translation	5043.29

from rotor's out-of-plane translational mode and (1,0) modes. These modes do not have any in-plane components. Moreover, they are all distinct modes.

There are two things worth noting in Fig. 4.2. First, q^R_{nd} modes from the rotor have very small response. This occurs because the in-plane and out-of-plane motions are very weakly coupled in this numerical example. The vibration of the housing is primarily rocking and slightly out-of-plane. Therefore, excitation at the housing modes does not generate significant in-plane response. In contrast, q^R_{nr} modes coupled very well with housing mode q^H_{nH}, because they both have significant rocking component. As a result, q^R_{nr} modes are strongly excited presenting significant response. Second, the response shows that a housing mode occurs at 936.7 Hz, a rocking mode at 183.3 Hz, and a (1,1) mode at 1200 Hz. These frequencies are very close to those in Tab. 4.1 indicating that numerical integration from $ODE45$ is quite accurate.

In the second round of simulations, the rotor spins at 7200 rpm. Figure 4.3 shows the frequency response under the same initial conditions. The notation of q^H_{nH}, q^R_{nr}, and q^R_{nd} remains the same as in Fig. 4.2. Comparing Fig. 4.2 with Fig. 4.3, we note that the housing mode frequency in rotor response q^R_{nr} has split from 936.7 Hz in Fig. 4.2 into two frequency

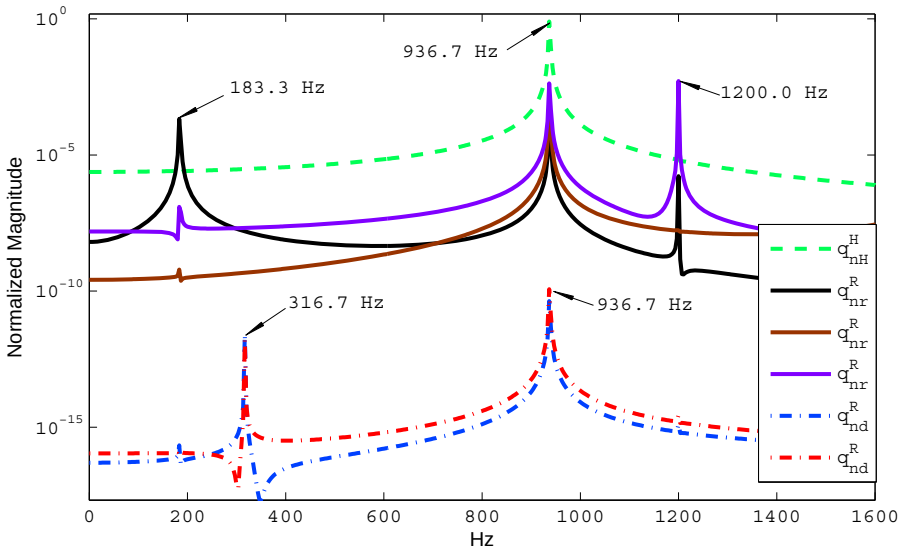

Figure 4.2: FFT of Free Responses when $\omega_3 = 0$

components at 936.7±120 Hz, which are 816.7 Hz and 1056.7 Hz, respectively. This confirms the gyroscopic splitting predicted in (4.9). Similarly, the rotor mode frequency in housing response q^H_{nr} has split from 1200 Hz in Fig. 4.2 into two frequency components at 1200 ± 120 Hz, which are 1080 Hz and 1320 Hz, respectively. This confirms the gyroscopic splitting predicted in (4.10).

4.2 Ground-Based Response

In this section, we will predict the ground-based response of the spinning rotor. In particular, we will investigate how the gyroscopic splitting affects ground-base response of a cyclic symmetric rotor through both theoretical predictions and numerical simulations.

4.2.1 Theoretical Analysis

As seen in Fig. 4.3, modal response of the rotor consists of two parts: response from the rotor-dominant modes (e.g., response at 183.3 Hz or 1200 Hz) and response from the housing-dominant modes with gyroscopic splitting. For rotor-dominant modes, the housing

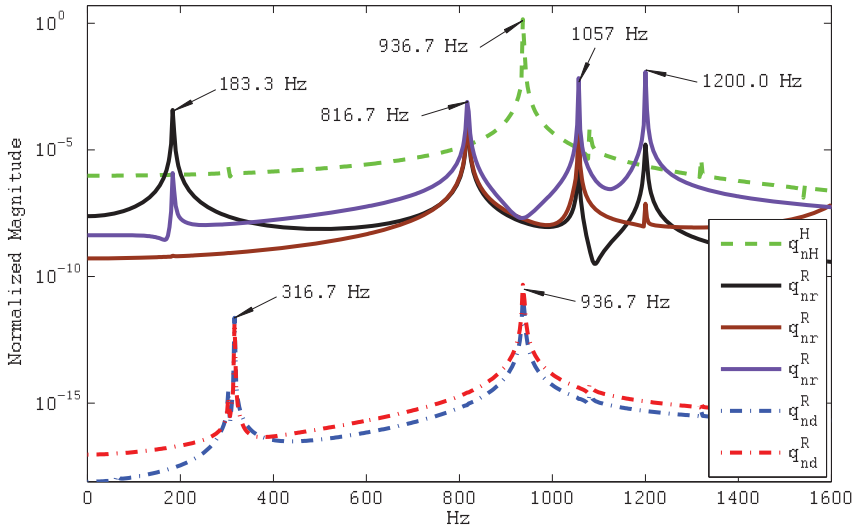

Figure 4.3: FFT of Free Responses when $\omega_3 = 7200$ RPM (120 Hz)

undergoes very small vibration and is negligible. Therefore, ground-based response of rotor-dominant modes can be predicted via [3], which studies a spinning, cyclic symmetric rotor with a rigid housing theoretically and experimentally. There is no need to repeat it here. The focus in this section is the ground-based response of the housing-dominant modes.

Without loss of generality, let us focus on a representative rotor mode $q_n^R(t)$ that has a significant response from a housing-dominant mode. Moreover, the housing-dominant mode has a natural frequency $\omega^{(H)}$, when $\omega_3 = 0$. (For example, $\omega^{(H)} = 936.7$ Hz from Fig. 4.2.) As the rotor spins, free vibration of the rotor mode presents gyroscopic splitting (4.9), and its rotor-based response becomes

$$q_n^R(t) = c_2 e^{j(\omega^{(H)} - \omega_3)t} + c_3 e^{j(\omega^{(H)} + \omega_3)t} + cc \tag{4.11}$$

where c_2 and c_3 are constants to be determined from the initial conditions, cc denotes complex conjugate.

Let the corresponding mode shape of the rotor be $\mathbf{W}^R(\tilde{\mathbf{r}}) \equiv \mathbf{W}^R(r, \theta, z)$. The rotor

response $\mathbf{W}^R_{nr}(\tilde{\mathbf{r}}, t)$ in the rotating frame xyz will be

$$\mathbf{W}^R(\tilde{\mathbf{r}}, t) \equiv \mathbf{W}^R_n(r, \theta, z) q^R_n(t) \quad \text{for } xyz \tag{4.12}$$

and the rotor response $\mathbf{W}^G_{nr}(\tilde{\mathbf{r}}, t)$ in the rotating in the fixed coordinates XYZ will be

$$\mathbf{W}^G(\mathbf{r}, t) \equiv \mathbf{W}^R_n(r, -\omega_3 t, z) q^R_n(t) \quad \text{for } XYZ \tag{4.13}$$

For a cyclic symmetric rotor, its mode shapes $\mathbf{W}^R_n(\tilde{\mathbf{r}})$ take a special form [3]. To reveal the special form concisely, we need to switch to complex mode shapes $\hat{\mathbf{W}}^R_n(\tilde{\mathbf{r}})$ for a moment. After the special form is explained, we will relate the complex mode shapes $\hat{\mathbf{W}}^R_n(\tilde{\mathbf{r}})$ back to the real mode shape $\mathbf{W}^R_n(\tilde{\mathbf{r}})$ to finish the derivation of ground-based response.

Let us assume that the rotor consists of N identical substructures, each spanning an angle of $2\pi/N$. Let $\mathbf{W}^{(i)}(\tilde{\mathbf{r}})$ denote the mode shape $\mathbf{W}^R(\tilde{\mathbf{r}})$ at the i-th substructure. According to [3], mode shapes at two neighboring substructures will differ by a constant phase angle; that is,

$$\hat{\mathbf{W}}^{(i+1)}(\tilde{\mathbf{r}}) = \hat{\mathbf{W}}^{(i)}(\tilde{\mathbf{r}}) e^{j2\pi n/N}; \quad n \in (1, 2, 3, ..., N) \tag{4.14}$$

Hence, one can use the phase angle $2\pi n/N$ or only the number n to characterize a vibration mode of the cyclic symmetric rotor. This number n is called *phase index*.

Also, vibration mode shapes of a stationary, cyclic symmetric rotor can be expanded in terms of a Fourier series [3]:

$$\hat{\mathbf{W}}^R_n(\tilde{\mathbf{r}}) = \sum_{k=n+\mathbf{M}(N)} \hat{\mathbf{A}}_k(r, z) e^{jk\theta} \tag{4.15}$$

where $\mathbf{M}(N)$ denotes an integer multiple of N and $\hat{\mathbf{A}}_k(r, z)$ are the Fourier coefficients. Equation (4.15) implies that only 1 out of every N Fourier coefficients is nontrivial for a cyclic symmetric rotor with N substructures.

The complex mode shapes $\hat{\mathbf{W}}^R_n(\tilde{\mathbf{r}})$ are related to the real mode shape $\mathbf{W}^R_n(\tilde{\mathbf{r}})$ as follows. For some n, $e^{j2\pi n/N}$ in (4.15) is a real number (e.g., $N = 4$ and $n = 2$). In this case, the complex mode shape $\hat{\mathbf{W}}^R_n(\tilde{\mathbf{r}})$ is a real function, and is identical to the real mode shape $\mathbf{W}^R_n(\tilde{\mathbf{r}})$. Moreover, this mode will have a distinct natural frequency. For other n, $e^{j2\pi n/N}$ in (4.15) is a complex number (e.g., $N = 3$ and $n = 1$). In this case, the two complex

modes $\hat{\mathbf{W}}_n^R(\tilde{\mathbf{r}})$ and $\hat{\mathbf{W}}_{N-n}^R(\tilde{\mathbf{r}})$ corresponding to phase indices n and $N-n$ not only are complex conjugate but also have repeated natural frequencies. Therefore, the real mode shape $\mathbf{W}_n^R(\tilde{\mathbf{r}})$ is a linear combination of $\hat{\mathbf{W}}_n^R(\tilde{\mathbf{r}})$ and $\hat{\mathbf{W}}_{N-n}^R(\tilde{\mathbf{r}})$ [1].

Substituting (4.11) and (4.15) into (4.12) results in the rotor response seen by a rotor-based observer

$$\mathbf{W}_{nr}^R(\tilde{\mathbf{r}},t) = \sum_{k=n+\mathbf{M}(N)} \mathbf{A}_k[e^{j[(\omega^{(H)}+\omega_3)t+k\theta]} + e^{j[(\omega^{(H)}-\omega_3)t+k\theta]}] + cc \tag{4.16}$$

By replacing $\theta = -\omega_3 t$ in (4.16) (cf. (4.13)), we obtain the rotor response seen by a ground-based observer

$$\mathbf{W}_{nr}^G(\tilde{\mathbf{r}},t) = \sum_{k=n+\mathbf{M}(N)} \mathbf{A}_k[e^{j(\omega^{(H)}-(k-1)\omega_3)t} + e^{j(\omega^{(H)}-(k+1)\omega_3)t}] + cc \tag{4.17}$$

Equation (4.17) indicate that the rotor's ground-based response will have frequency components $\omega^{(H)} - (k+1)\omega_3$ and $\omega^{(H)} - (k-1)\omega_3$, where $k = n + \mathbf{M}(N)$. The presence of these frequency components manifests the coupling effect between the rotor and housing, because the phase index n belongs to the rotor and the natural frequency $\omega^{(H)}$ comes from the housing dominate mode.

There are two things worth noting for (4.17). First, (4.17) is derived with the assumption of a real mode shape. For distinct modes, (4.17) can be used directly. For repeated modes, (4.17) needs to include both phase indices n and $N-n$ to account for the linear combination of two complex modes $\hat{\mathbf{W}}_n^R(\tilde{\mathbf{r}})$ and $\hat{\mathbf{W}}_{N-n}^R(\tilde{\mathbf{r}})$. Second, whether or not the ground-based response will appear with all the frequency components $\omega^{(H)}-(k+1)\omega_3$ and $\omega^{(H)}-(k-1)\omega_3$ will depend on the excitation. If a frequency component is not excited, it will not appear in the ground-based response.

4.2.2 Numerical Confirmation

For the benchmark numerical example, there are four identical substructures. Therefore, $N = 4$. Moreover, the (1,1) mode is the only elastic mode that presents significant gyroscopic splitting. The phase index of (1,1) mode is $n = 1$ or $n = 3$. According to (4.17), the rotor's

[1] Please refer to Appendix B for detail

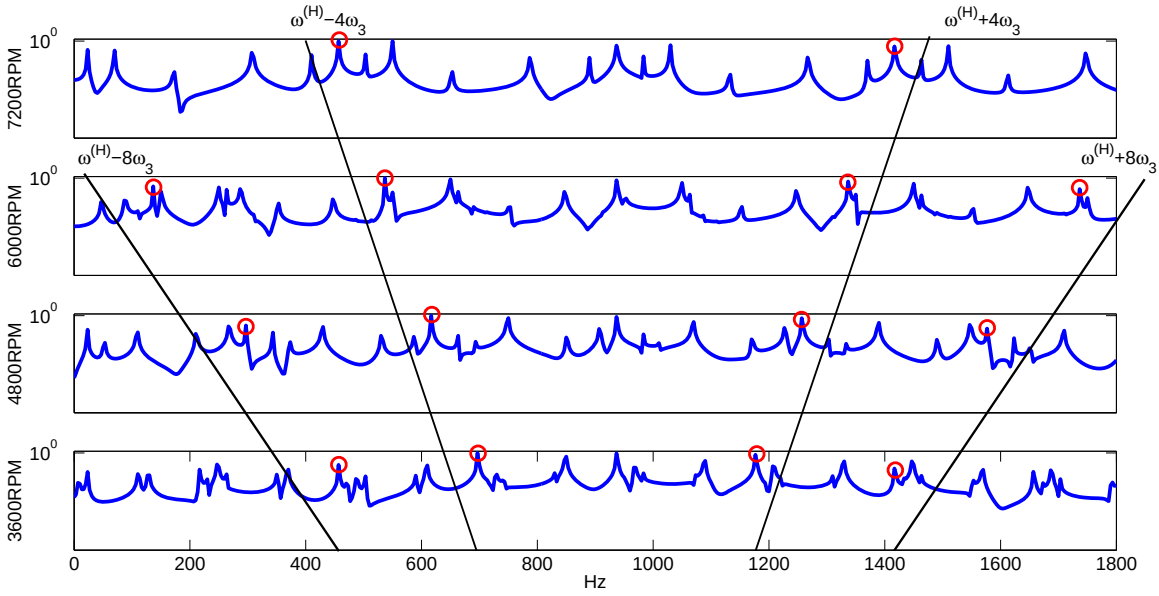

Figure 4.4: Waterfall Plot of Ground-based Response of the Rotor

response seen by a ground-based observer should have frequency components $\omega^{H_0} \pm 2\omega_3$, $\omega^{H_0} \pm 4\omega_3$, $\omega^{H_0} \pm 6\omega_3$, and so on.

Figure 4.4 shows the waterfall plot of simulated rotor response seen from a ground-based observer. As seen in Fig. 4.4, the ground-based response contains multiple frequency branches of various frequency components. As explained earlier, many of these frequencies components are rotor modes and thus not related to gyroscopic splitting of the housing mode; therefore, they have been well studied in detail in [3]. The current focus is to look for harmonic branches arising from the combination of gyroscopic splitting and the cyclic symmetry patterns occurring at $\omega^{H_0} \pm 2\omega_3$, $\omega^{H_0} \pm 4\omega_3$, $\omega^{H_0} \pm 6\omega_3$, and so on. These frequency branches symbolize coupled vibration of the rotor and the housing.

With ω^{H_0} being 936.7 Hz, we can easily identify frequency branches $\omega^{H_0} \pm 2\omega_3$, $\omega^{H_0} \pm 4\omega_3$, and $\omega^{H_0} \pm 6\omega_3$, which are denoted by the thin solid lines. Figure 4.4 clearly shows that rotor response presents significant peaks at those frequencies as the spin speed increases. This confirms the theoretical predictions in (4.17).

Chapter 5

CLOSED-FORM SOLUTIONS

For a stationary cyclic symmetric rotor, the vibration mode shapes are twofold, i.e., the repeated modes and distinct modes which are governed by different phase indices n_r and n_d, respectively. Literature [27] discusses in great detail that repeated modes and distinct modes are completely decoupled in the centrifugal softening matrix and gyroscopic matrix in the formulation of the spinning rotor. (cf. (2.15) and (2.18)).

With certain kinematic assumptions, the rotor-bearing deformation modal matrix $\mathbf{B}^R$ (2.39) can be simplified and thus the repeated modes and distinct modes are decoupled in $\mathbf{K}^B(t)$ (2.41). In such case, (2.50) can be simplified to have constant coefficients by a coordinate transformation and thus traditional analyses in time invariant linear systems, such as eigenvalues and eigenvectors, state-space, or response function techniques, are sufficient to derive the closed-form solutions of the system.

In this section, the mathematics of matrix exponential will be extensively used. The relevant proofs can be found in [52].

5.1 Kinematic Assumption

In order to derive the closed-form solution, two kinematic assumptions are made.

1. the rotor consists of two parts, a rigid hub and the flexible parts. The rigid hub is assembled to stationary housing via bearings

2. The mode shape of flexible parts is assumed to be entirely out-of-plane.

5.2 Equation of Motion

In order to easily keep track on the derivation of closed-form solutions, let us quickly review the formulation of the equations of motion of the system. Please refer to Chap. 2 *Reduced*

Order Model for detail of the derivation. Based on (2.50), the equations of motion governing the free vibration of a spinning cyclic symmetric rotor coupled to the housing via bearings takes the mathematical form.

$$\ddot{\mathbf{q}} + \mathbf{G}\dot{\mathbf{q}} + \left[\mathbf{K} + \mathbf{K}^B(t)\right]\mathbf{q} \;=\; 0 \tag{5.1}$$

In (5.1),

$$\mathbf{G} = \begin{bmatrix} \mathbf{0} & \mathbf{0} \\ \mathbf{0} & \mathbf{G}_{22}(n,m) \end{bmatrix} \tag{5.2}$$

with $\mathbf{G}_{22}(n,m) = 2\omega_3 g_{nm} = -2\omega_3 g_{mn}$, where $g_{nm} \equiv \mathbf{k} \cdot \int \left[\mathbf{W}_m^R(\tilde{\mathbf{r}}) \times \mathbf{W}_n^R(\tilde{\mathbf{r}})\right] dm$. Also,

$$\mathbf{K} = \begin{bmatrix} \boldsymbol{\omega}^H & \mathbf{0} \\ \mathbf{0} & \boldsymbol{\omega}^R - \omega_3^2 \mathbf{K}_\lambda(n,m) \end{bmatrix} \tag{5.3}$$

where $\boldsymbol{\omega}^H \equiv \text{diag}\left[\left\{\omega_1^H\right\}^2, \left\{\omega_2^H\right\}^2, \ldots, \left\{\omega_{n_H}^H\right\}^2\right]$, $\boldsymbol{\omega}^R \equiv \text{diag}\left[\left\{\omega_1^R\right\}^2, \left\{\omega_2^R\right\}^2, \ldots, \left\{\omega_{n_R}^R\right\}^2\right]$, and $\mathbf{K}_\lambda(n,m) = \lambda_{nm} \equiv \delta_{mn} - \int W_{mz}^R(\tilde{\mathbf{r}}) W_{nz}^R(\tilde{\mathbf{r}}) dm$. As detailed in Sec. 2.1 *Coordinate Systems*, the equation of motion is derived under two coordinate systems: a ground-based system XYZ and a rotor-based system xyz. ω_3 is defined as the spinning speed. Let $\mathbf{I}$, $\mathbf{J}$, and $\mathbf{K}$ be the unit vectors of XYZ and $\mathbf{i}$, $\mathbf{j}$, and $\mathbf{k}$ be the unit vectors of xyz. The coordinate transformation between the two coordinates can be found in (2.2) as

$$\begin{pmatrix} \mathbf{i} \\ \mathbf{j} \\ \mathbf{k} \end{pmatrix} = \mathbf{R}(t) \begin{pmatrix} \mathbf{I} \\ \mathbf{J} \\ \mathbf{K} \end{pmatrix} \tag{5.4}$$

where $\mathbf{R}(t)$ is a coordinate transformation matrix given by

$$\mathbf{R}(t) = \begin{bmatrix} \cos(\omega_3 t) & -\sin(\omega_3 t) & 0 \\ \sin(\omega_3 t) & \cos(\omega_3 t) & 0 \\ 0 & 0 & 1 \end{bmatrix} \tag{5.5}$$

The following explains how $\mathbf{K}^B(t)$ is derived. Let us assume $\mathbf{r}_{A'}$ is the bearing position of the housing while $\tilde{\mathbf{r}}_A$ is that of the rotor. According to (2.31), we can define a linear housing-bearing deformation modal matrix $\mathbf{W}^H \equiv [\mathbf{W}_1^H(\mathbf{r}_{A'}), \mathbf{W}_2^H(\mathbf{r}_{A'}), \cdots, \mathbf{W}_{n_H}^H(\mathbf{r}_{A'})]$ and the corresponding angular deformation modal matrix $\boldsymbol{\alpha}^H \equiv [\boldsymbol{\alpha}_1^H(\mathbf{r}_{A'}), \boldsymbol{\alpha}_2^H(\mathbf{r}_{A'}), \cdots, \boldsymbol{\alpha}_{n_H}^H(\mathbf{r}_{A'})]$.

Then, from (2.38), the linear and angluar bearing deformations contributed by the housing, i.e., the housing-bearing deformation modal matrix is defined as

$$\mathbf{B}^H = \begin{bmatrix} \mathbf{W}^H \\ \boldsymbol{\alpha}^H \end{bmatrix} \tag{5.6}$$

Next, let us retain rotor modes in a sequential order where repeated mode pairs are retained prior to all distinct modes such that one can define the rotor-bearing deformation modal matrix (cf. (2.39)) as

$$\begin{aligned} \mathbf{B}^R &= \begin{bmatrix} \mathbf{W}^R_{1,1}(\tilde{\mathbf{r}}_A) & \mathbf{W}^R_{1,2}(\tilde{\mathbf{r}}_A) & \cdots & \mathbf{W}^R_{nr,1}(\tilde{\mathbf{r}}_A) & \mathbf{W}^R_{nr,2}(\tilde{\mathbf{r}}_A) & \mathbf{W}^R_{1}(\tilde{\mathbf{r}}_A) & \cdots & \mathbf{W}^R_{nd}(\tilde{\mathbf{r}}_A) \\ \boldsymbol{\beta}^R_{1,1}(\tilde{\mathbf{r}}_A) & \boldsymbol{\beta}^R_{1,2}(\tilde{\mathbf{r}}_A) & \cdots & \boldsymbol{\beta}^R_{nr,1}(\tilde{\mathbf{r}}_A) & \boldsymbol{\beta}^R_{nr,2}(\tilde{\mathbf{r}}_A) & \boldsymbol{\beta}^R_{1}(\tilde{\mathbf{r}}_A) & \cdots & \boldsymbol{\beta}^R_{nd}(\tilde{\mathbf{r}}_A) \end{bmatrix} \\ &= \begin{bmatrix} \mathbf{B}^{R,1/2}_1 & \cdots & \mathbf{B}^{R,1/2}_{nr} & \mathbf{B}^{R,nd} \end{bmatrix} \end{aligned} \tag{5.7}$$

where subscript nr denote the nrth repeated mode *pair* and the superscript $R, 1/2$ denotes that $\mathbf{B}^{R,1/2}_{nr}$ contains one pair of two rotor-bearing deformation modal vectors of the nrth repeated modes, $\mathbf{B}^{R,1}_{nr}$ and $\mathbf{B}^{R,2}_{nr}$, while superscript R, nd denotes that the rotor-bearing deformation matrix $\mathbf{B}^{R,nd}$ contains *all* nd's distinct modes. That is, in (5.7),

$$\begin{aligned} \mathbf{B}^{R,1/2}_{nr} &= \begin{bmatrix} \mathbf{W}^R_{nr,1} & \mathbf{W}^R_{nr,2} \\ \boldsymbol{\beta}^R_{nr,1} & \boldsymbol{\beta}^R_{nr,2} \end{bmatrix} \\ &= \begin{bmatrix} \mathbf{B}^R_{nr,1} & \mathbf{B}^R_{nr,2} \end{bmatrix} \end{aligned} \tag{5.8}$$

and

$$\begin{aligned} \mathbf{B}^{R,nd} &= \begin{bmatrix} \mathbf{W}^R_{1} & \cdots & \mathbf{W}^R_{nd} \\ \boldsymbol{\beta}^R_{1} & \cdots & \boldsymbol{\beta}^R_{nd} \end{bmatrix} \\ &= \begin{bmatrix} \mathbf{B}^R_{1} & \cdots & \mathbf{B}^R_{nd} \end{bmatrix} \end{aligned} \tag{5.9}$$

Next, let us define a reduced transformation matrix $\mathbf{R}'(t)$ to be the 2 by 2 matrix in $\mathbf{R}(t)$ containing only the time dependent entries; see (5.5) or (2.3). From (2.37), we can therefore define a 5×5 transformation matrix $\mathbf{T}(t)$ between the rotor and the housing at the bearing location as

$$\mathbf{T}(t) \equiv \mathbf{R}(t) \oplus \mathbf{R}'(t) \tag{5.10}$$

where $\oplus$ is the direct sum of $\mathbf{R}(t)$ and $\mathbf{R}'(t)$. $\mathbf{T}(t)$ satisfies the following property:

$$\frac{d}{dt}\mathbf{T} = \mathbf{S_T}\mathbf{T} = \mathbf{T}\mathbf{S_T} \tag{5.11}$$

In (5.11)

$$\mathbf{S_T} = \omega_3 \begin{bmatrix} 0 & -1 & 0 & 0 & 0 \\ 1 & 0 & 0 & 0 & 0 \\ 0 & 0 & 0 & 0 & 0 \\ 0 & 0 & 0 & 0 & -1 \\ 0 & 0 & 0 & 1 & 0 \end{bmatrix} \tag{5.12}$$

Finally, the housing-bearing-rotor modal matrix $\mathbf{B}^B(t)$ is defined the same as (2.40)

$$\mathbf{B}^B(t) = \begin{bmatrix} \mathbf{B}^H & \mathbf{T}(t)\mathbf{B}^R \end{bmatrix} \tag{5.13}$$

If the bearing is elastic with a 5×5 stiffness matrix $\tilde{\mathbf{K}}^B$, the generalized bearing stiffness $\mathbf{K}^B(t)$ associated with the bearing deformation, or the housing-bearing-housing modal matrix, $\mathbf{B}^B(t)$ will take the form (also see (2.41))

$$\mathbf{K}^B(t) \equiv \sum (\mathbf{B}^B(t))^T \tilde{\mathbf{K}}^B \mathbf{B}^B(t) \tag{5.14}$$

Note that $\mathbf{K}^B(t)$ is a periodic matrix with the period $2\pi/\omega_3$ resulting from the periodicity of $\mathbf{B}^B(t)$.

5.3 Simplification of the Time Varying Housing-bearing-rotor Modal Matrix $\mathbf{B}^B(t)$

In this section, we will show how $\mathbf{B}^B(t)$ can be simplified, given the kinematic assumptions in Sec. 5.1. When the flexible parts of the rotor only has out-of-plane motion, the boundary forces and moments of repeated modes and distinct modes have complete different characteristics. The former always have rocking moments exerting on the hub while the latter always have out-of-plane force that causes hub vibrating out-of-plane as well.

5.3.1 Boundary Forces and Moments

In order to derive the boundary forces and moments of the rotor modes, let us consider the position vector of the rotor $\tilde{\mathbf{r}}$ in a cylindrical coordinate, i.e., $\tilde{\mathbf{r}} = r\cos\theta\mathbf{e}_x + r\sin\theta\mathbf{e}_y + z\mathbf{e}_z =$

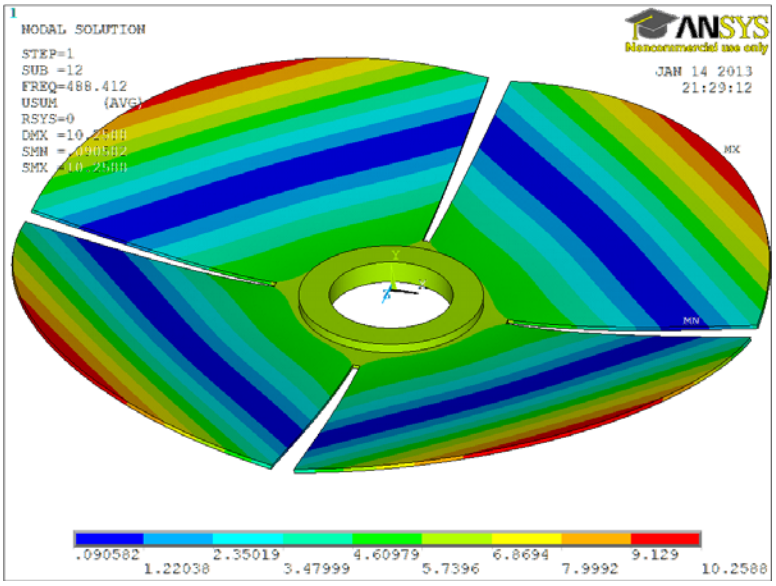

Figure 5.1: Mode Shape of a Distinct Rotor Mode with Phase Index $n = 4$. The Hub Moves Entirely Out-plane.

$\mathbf{b}(\tilde{\mathbf{r}})e^{j\theta} + \mathbf{b}^*(\tilde{\mathbf{r}})e^{-j\theta} + z\mathbf{e}_z$, where $\mathbf{b}(\tilde{\mathbf{r}}) \equiv r/2(\mathbf{e}_x - j\mathbf{e}_y)$ and $\mathbf{b}^*(\tilde{\mathbf{r}})$ are the complex conjugate pair.

According to [3], the boundary force and moment exerted by repeated modes or distinct modes at the interface between the rigid hub and flexible parts can be calculated by the formula as follows.

$$\mathbf{F} = 2\pi \int \mathbf{A}_0(r, z)d\mathbf{A}, \qquad n = N \tag{5.15}$$

and

$$\mathbf{M} = \mathbf{S}_1 + \mathbf{S}_2 + \mathbf{S}_3 \tag{5.16}$$

In (5.2)

$$\mathbf{S}_1 = 2\pi \int [\mathbf{b}(\tilde{\mathbf{r}}) \times \mathbf{A}_{-1}(r, z)]d\mathbf{A}, \qquad n = N - 1 \tag{5.17}$$

$$\mathbf{S}_2 = 2\pi \int [\mathbf{b}^*(\tilde{\mathbf{r}}) \times \mathbf{A}_1(r,z)] d\mathbf{A}, \quad n = 1 \tag{5.18}$$

$$\mathbf{S}_3 = 2\pi \int [z\mathbf{e}_z \times \mathbf{A}_0(r,z)] d\mathbf{A}, \quad n = N \tag{5.19}$$

where $\mathbf{A}_{0,-1,1}$ are the Fourier coefficients of rotor mode shapes (cf. (4.15)).

Since the vibration motion of the flexible part is assumed to have only out-of-plane motion (see Sec 6.2 *Kinematic Assumption*), i.e., $\mathbf{A}_k = A_{k,z}\mathbf{e}_z$, the repeated modes exerts only unbalanced inertia moments $\mathbf{S}_1$ or $\mathbf{S}_2$ whereas distinct modes exerts only unbalanced inertia force $\mathbf{F} = F_z\mathbf{e}_z$ at the boundary, which can be easily verified by substituting $\mathbf{A}_k = A_{k,z}\mathbf{e}_z$ into (5.15) to (5.19). Furthermore, since the hub is assumed rigid (also see Sec 6.2 *Kinematic Assumption*), the unbalanced inertia force $\mathbf{F} = F_z\mathbf{e}_z$ will cause the hub to have infinitesimal out-of-plane translation along the $\mathbf{e}_z$ direction. As a result, the rotor-bearing modal vector of distinct modes $\mathbf{B}^R_{nd}$ in (5.9) now becomes

$$\mathbf{B}^R_{nd} = B_{nd,z}\mathbf{e}_z \tag{5.20}$$

Fig. 5.1 shows the mode shape of a distinct mode with phase index $n = 4$ from FEA. As seen, the hub has entirely out-of-plane motion.

Similarly, since $\mathbf{S}_1$ or $\mathbf{S}_2$ are unbalanced moments containing either $\mathbf{e}_x$ or $\mathbf{e}_y$ components, the hub will have infinitesimal rocking motions. Thus, the rotor-bearing modal vectors of repeated modes $\mathbf{B}^R_{nr,1}$ and $\mathbf{B}^R_{nr,1}$ in (5.8) now only have $\mathbf{e}_x$ and $\mathbf{e}_y$ components.

$$\begin{aligned} \mathbf{B}^R_{nr,1} &= B^R_{nr,1,x}\mathbf{e}_x + B^R_{nr,1,y}\mathbf{e}_y \\ \mathbf{B}^R_{nr,2} &= B^R_{nr,2,x}\mathbf{e}_x + B^R_{nr,2,y}\mathbf{e}_y \end{aligned} \tag{5.21}$$

The rotor-bearing modal vectors of one repeated modes pair $\mathbf{B}^R_{nr,1}$ and $\mathbf{B}^R_{nr,1}$ are orthogonal to each other, which can be shown in detail as follows. To verify the orthogonality, let us substitute $\mathbf{A}_1 = A_{1,z}\mathbf{e}_z$ and $\mathbf{A}_{-1} = A_{-1,z}\mathbf{e}_z$ into (5.17) and (5.18) and notice that $\mathbf{A}_{-1}(r,z) = \mathbf{A}^*_1(r,z)$ are the complex conjugate pair because the repeated modes have phase indices $n = -1$ and $n = N - 1$ [27].

$$\begin{aligned}\mathbf{S}_1 &= 2\pi \int [\frac{r}{2}(-jA_{-1,z}\mathbf{e}_x - A_{-1,z}\mathbf{e}_y)]d\mathbf{A} = -S^* j\mathbf{e}_x - S^*\mathbf{e}_y, \quad n = N-1 \\ \mathbf{S}_2 &= 2\pi \int [\frac{r}{2}(jA_{1,z}\mathbf{e}_x - A_{1,z}\mathbf{e}_y)]d\mathbf{A} = Sj\mathbf{e}_x - S\mathbf{e}_y, \quad n = 1\end{aligned} \tag{5.22}$$

where $S \equiv 1/2 \int [rA_{1,z}]d\mathbf{A}$ is the complex unbalanced moment vector.

In order to arrive at the real moment vectors from the complex conjugate complex moments $\mathbf{S}_1$ and $\mathbf{S}_2$, we define a pair of real moment vectors.

$$\begin{aligned}\begin{bmatrix} \mathbf{S}^{\mathcal{R}} \\ \mathbf{S}^{\mathcal{I}} \end{bmatrix} &= \frac{\sqrt{2}}{2}\begin{bmatrix} 1 & 1 \\ -j & j \end{bmatrix}\begin{bmatrix} \mathbf{S}_1 \\ \mathbf{S}_2 \end{bmatrix} \\ &= \frac{\sqrt{2}}{2}\begin{bmatrix} Sj - S^*j \\ S + S^* \end{bmatrix}\mathbf{e}_x + \frac{\sqrt{2}}{2}\begin{bmatrix} -S - S^* \\ Sj - S^*j \end{bmatrix}\mathbf{e}_y\end{aligned} \tag{5.23}$$

where the superscripts $\mathcal{R}$ and $\mathcal{I}$ denote the real part and the imaginary part respectively.

Taking the vector product on $\mathbf{S}^{\mathcal{R}}$ and $\mathbf{S}^{\mathcal{I}}$ results in

$$\mathbf{S}^{\mathcal{R}} \cdot \mathbf{S}^{\mathcal{I}} = \frac{1}{2}[(S + S^*)(S - S^*)j - (S + S^*)(S - S^*)j] = 0 \tag{5.24}$$

From (5.23), $\mathbf{S}^{\mathcal{R}}$ and $\mathbf{S}^{\mathcal{I}}$ are orthogonal to each other because their vector product is equal to zero. Since the hub is assumed rigid, this orthogonal pair of moments $\mathbf{S}^{\mathcal{R}}$ and $\mathbf{S}^{\mathcal{I}}$ will respectively give rise to the hub orthogonal infinitesimal rocking motions. As a result, the rotor-bearing modal vectors of repeated modes $\mathbf{B}^R_{nr,1}$ and $\mathbf{B}^R_{nr,1}$ differ by a rigid body rotation along the z axis by $\pm\pi/2$. Conventionally, we define the sequential order of repeated modes such that $\mathbf{B}^R_{nr,1}$ and $\mathbf{B}^R_{nr,1}$ comply with the following equation.

$$\mathbf{B}^R_{nr,2} = \mathbf{T}(\frac{\pi}{2})\mathbf{B}^R_{nr,1} \tag{5.25}$$

where $\pi/2$ is substituted into (5.10) which denotes the rigid body rotation by $\pi/2$.

Fig. 5.2 shows a pair of repeated mode shapes with phase index $n = 1$ and $n = 3$ from FEA. As seen, the hub undergoes orthogonal infinitesimal in-plane rocking motions, respectively in the fist and second modes.

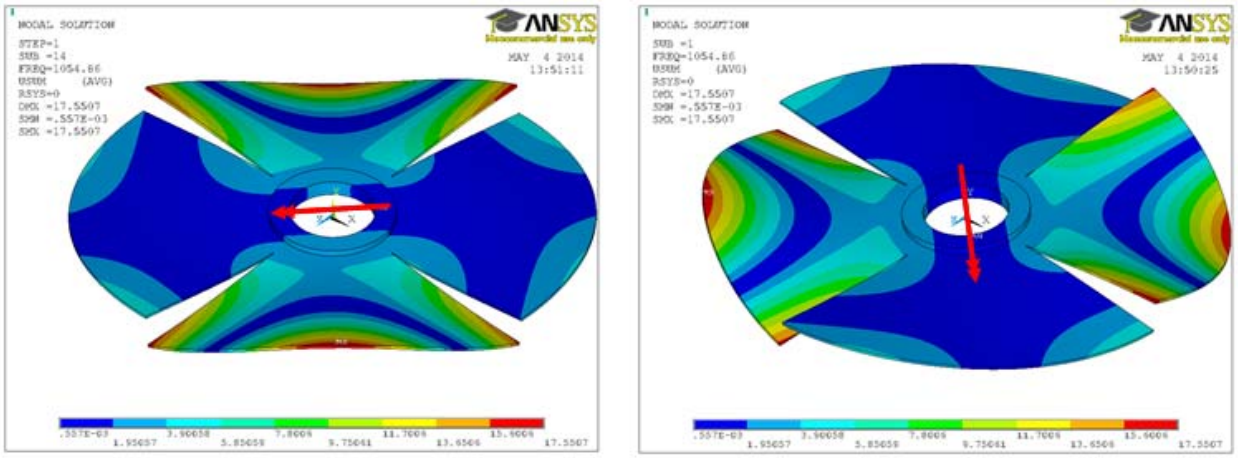

Figure 5.2: Mode Shape of a Pair of Repeated Modes with Phase Index $n = 1, 3$. The Hub Has Rocking In-plane Motions. The Red Double-headed Arrows Indicate the Directions of Rocking Motions. It is Clearly Seen that the Arrows are Orthogonal to One and the Other.

Substituting (5.20) into (5.9) and Premultiplying with (5.10) leads to

$$\begin{aligned}
\mathbf{T}(t)\mathbf{B}^{R,nd} &= \begin{bmatrix} \cos\omega_3 & -\sin\omega_3 & 0 & 0 & 0 \\ \sin\omega_3 & \cos\omega_3 & 0 & 0 & 0 \\ 0 & 0 & 1 & 0 & 0 \\ 0 & 0 & 0 & \cos\omega_3 & -\sin\omega_3 \\ 0 & 0 & 0 & \sin\omega_3 & \cos\omega_3 \end{bmatrix} \begin{bmatrix} 0 & & 0 \\ 0 & & 0 \\ B_{1,z} & \cdots & B_{nd,z} \\ 0 & & 0 \\ 0 & & 0 \end{bmatrix} \\
&= \begin{bmatrix} 0 & & 0 \\ 0 & & 0 \\ B_{1,z} & \cdots & B_{nd,z} \\ 0 & & 0 \\ 0 & & 0 \end{bmatrix} \\
&= \mathbf{B}^{R,nd}
\end{aligned} \tag{5.26}$$

The most important consequence of (5.25) is that we can see that the distinct modes do not contribute any time varying components to the bearing deformations. As a result, the housing-bearing-rotor modal matrix $\mathbf{B}^B(t)$ (5.13) now can be simplified.

$$\mathbf{B}^B(t) = \begin{bmatrix} \mathbf{B}^H & \mathbf{T}(t)\mathbf{B}_1^{R,1/2} & \cdots & \mathbf{T}(t)\mathbf{B}_{nr}^{R,1/2} & \mathbf{B}^{R,nd} \end{bmatrix} \tag{5.27}$$

In (5.27), $\mathbf{B}^B(t)$ contains two parts, the constant parts and time varying parts. The constant parts contains $\mathbf{B}^H$ and $\mathbf{B}_{nd}^R$. The time varying parts contains the rotor-bearing modal matrix of each paired repeated modes $\mathbf{B}_{nr}^{R,1/2}$.

5.4 Coordinate Transformation

Thus far, we have already finished all the preliminary derivations on bearing deformation and boundary forces and moments of repeated modes and distinct modes as the consequences of the kinematic assumptions. It is being shown in the previous section that only the repeated modes contribute to the time varying part of the housing-bearing-rotor modal matrix $\mathbf{B}^B(t)$. Furthermore, the rotor-bearing modal vectors $\mathbf{B}_{nr,1}^R$ and $\mathbf{B}_{nr,1}^R$ differ by a rigid body rotation along the z axis by $\pm\pi/2$ (5.25). Our goal now then is to find a real-valued, time variant, coordinate transformation $\mathbf{q} = \mathbf{Q}(t)\mathbf{q}'$ such that (5.1) can be transformed into a system of ordinary differential equations with *constant* coefficients. Let us assume such $\mathbf{Q}(t)$ exists, and hence it can be written as an exponential of a real-valued, constant, matrix $\mathbf{S}$, such that

$$\mathbf{Q}(t) = \exp[\mathbf{S}t] \tag{5.28}$$

To avoid the trivial case $\mathbf{Q} = \mathbf{I}$, $\mathbf{S}$ is assumed to be equal to a non-zero matrix.

$\mathbf{Q}(t)$ satisfies the following property.

$$\frac{d}{dt}\mathbf{Q}(t) = \mathbf{S}\mathbf{Q}(t) = \mathbf{Q}(t)\mathbf{S} \tag{5.29}$$

for $\mathbf{Q}(t)$ is a matrix exponential of $\mathbf{S}$.

5.4.1 Decomposition of $\mathbf{S}$

Based on (5.27), let us assume $\mathbf{S}$ admits a form

$$\mathbf{S} = \mathbf{S}^H \oplus \mathbf{S}^{R,2nr} \oplus \mathbf{S}^{R,nd} \tag{5.30}$$

In (5.30) $\mathbf{S}^H$ has the dimension $nH \times nH$, $\mathbf{S}^{R,2nr}$ has $2nr \times 2nr$, and $\mathbf{S}^{R,nd}$ has $nd \times nd$ where nH, nr, and nd are total numbers of retained housing modes, repeated rotor mode pairs, and distinct rotor modes, respectively.

It follows that $\mathbf{Q}(t) = \mathbf{Q}^H(t) \oplus \mathbf{Q}^{R,2nr}(t) \oplus \mathbf{Q}^{R,nd}(t) = \exp[(\mathbf{S}^H)t] \oplus \exp[(\mathbf{S}^{R,2nr})t] \oplus \exp[(\mathbf{S}^{R,nd})t]$, i.e., the coordinate transformation takes place on housing modes, repeated rotor mode pairs, and distinct rotor modes, respectively.

5.4.2 Time Derivatives of $\mathbf{q}'$

The the time derivatives of $\mathbf{q}'$ can be calculated as follows.

$$\begin{cases} \dot{\mathbf{q}} = \mathbf{Q}(t)\dot{\mathbf{q}}' + \mathbf{Q}(t)\mathbf{S}\mathbf{q}' \\ \ddot{\mathbf{q}} = \mathbf{Q}(t)\ddot{\mathbf{q}}' + 2\mathbf{Q}(t)\mathbf{S}\dot{\mathbf{q}}' + \mathbf{Q}(t)\mathbf{S}^2\mathbf{q}' \end{cases} \tag{5.31}$$

Substitution (5.31) into (5.1) and premultiply by the inverse $\mathbf{Q}^{-1}$ yields

$$\begin{aligned} \ddot{\mathbf{q}}' &+ \left[\mathbf{Q}^{-1}(t)\mathbf{G}\mathbf{Q}(t) + 2\mathbf{S}\right]\dot{\mathbf{q}}' \\ &+ \left[\mathbf{Q}^{-1}(t)\mathbf{K}\mathbf{Q}(t) + \mathbf{Q}^{-1}(t)\mathbf{G}\mathbf{Q}(t)\mathbf{S} + \mathbf{Q}^{-1}(t)\mathbf{K}^B(t)\mathbf{Q}(t) + \mathbf{S}^2\right]\mathbf{q}' = 0 \end{aligned} \tag{5.32}$$

It follows that the following equations have to be satisfied for (5.32) to have constant coefficients.

$$\begin{cases} \mathbf{Q}^{-1}(t)\mathbf{K}^B(t)\mathbf{Q}(t) = \mathbf{C}_1 \\ \mathbf{Q}^{-1}(t)\mathbf{K}\mathbf{Q}(t) = \mathbf{C}_2 \\ \mathbf{Q}^{-1}(t)\mathbf{G}\mathbf{Q}(t) = \mathbf{C}_3 \end{cases} \tag{5.33}$$

where $\mathbf{C}_i,\ i = 1, 2, 3$ are non-singular constant matrices.

5.5 Existence of $\mathbf{Q}(t)$

To find $\mathbf{Q}$ let us plug (5.14) into the first equation in (5.33).

$$\mathbf{Q}^{-1}(t)(\mathbf{B}^B(t))^T\tilde{\mathbf{K}}^B\mathbf{B}^B(t)\mathbf{Q}(t) = \mathbf{C}_1 \tag{5.34}$$

For (5.34) to be valid, the following two equations have to be satisfied.

$$\begin{cases} \mathbf{B}^B(t)\mathbf{Q}(t) = \tilde{\mathbf{C}} \\ \mathbf{Q}^{-1}(t)(\mathbf{B}^B(t))^T = \hat{\mathbf{C}} \end{cases} \tag{5.35}$$

where $\hat{\mathbf{C}}$ and $\tilde{\mathbf{C}}$ are two non-singular constant matrices. One thing worth noticing is that if $\mathbf{Q}(t)$ is an orthonormal matrix satisfying $\mathbf{Q}^T = \mathbf{Q}^{-1}$ the two equations in (5.35) will be both satisfied and $\hat{\mathbf{C}} = \tilde{\mathbf{C}}^T$. To this end, we will prove such a $\mathbf{Q}(t)$ which satisfies the first equation in (5.35) exists and $\mathbf{Q}(t)$ is an orthonormal matrix such that the second equation is trivially satisfied.

Taking the time derivative on both sides of the first equation in (5.35) and noticing $\tilde{\mathbf{C}}$ is a constant matrix gives us an auxiliary equation.

$$\begin{aligned} \frac{d}{dt}\left(\mathbf{B}^B\mathbf{Q}\right) &= \frac{d}{dt}\tilde{\mathbf{C}} \\ \dot{\mathbf{B}}^B\mathbf{Q} + \mathbf{B}^B\dot{\mathbf{Q}} &= \mathbf{0} \\ \left(\dot{\mathbf{B}}^B + \mathbf{B}^B\mathbf{S}\right)\mathbf{Q} &= \mathbf{0} \\ \dot{\mathbf{B}}^B &= -\mathbf{B}^B\mathbf{S} \end{aligned} \tag{5.36}$$

In (5.36) $\dot{\mathbf{B}}^B$ is

$$\begin{aligned} \dot{\mathbf{B}}^B &= \begin{bmatrix} \mathbf{0} & \mathbf{T}\mathbf{S}_\mathbf{T}\mathbf{B}^R \end{bmatrix} \\ &= \mathbf{T}\begin{bmatrix} \mathbf{0} & \mathbf{S}_\mathbf{T}\mathbf{B}^R \end{bmatrix} \end{aligned} \tag{5.37}$$

where (5.11), (5.12), and (5.13) are used. Plug in (5.13) and (5.37) into (5.36) to arrive at the final auxiliary equation

$$\begin{aligned} \mathbf{T}\begin{bmatrix} \mathbf{0} & \mathbf{S}_\mathbf{T}\mathbf{B}^R \end{bmatrix} &= \begin{bmatrix} \mathbf{B}^H & \mathbf{T}\mathbf{B}^R \end{bmatrix}\mathbf{S} \\ \mathbf{T}\begin{bmatrix} \mathbf{0} & \mathbf{S}_\mathbf{T}\mathbf{B}^R \end{bmatrix} &= \mathbf{T}\begin{bmatrix} \mathbf{T}^T\mathbf{B}^H & \mathbf{B}^R \end{bmatrix}\mathbf{S} \\ \begin{bmatrix} \mathbf{0} & \mathbf{S}_\mathbf{T}\mathbf{B}^R \end{bmatrix} &= \begin{bmatrix} \mathbf{T}^T\mathbf{B}^H & \mathbf{B}^R \end{bmatrix}\mathbf{S} \end{aligned} \tag{5.38}$$

Eqn. (5.38) is the master equation we will solve for $\mathbf{S}$ (and thus for $\mathbf{Q}$) provided that $\mathbf{B}$ is known. Before we really go into solving (5.38), let us apply the composition of $\mathbf{S}$ (5.30) to (5.38) first.

If we plug (5.7) and (5.30) into (5.38) we arrive at three separate equations

$$\begin{cases} \mathbf{0} = -\mathbf{T}^T\mathbf{B}^H\mathbf{S}^H \\ \mathbf{S_T}\left[\mathbf{B}_1^{R,1/2}\cdots\right] = -\left[\mathbf{B}_1^{R,1/2}\cdots\right]\mathbf{S}^{R,2nr} \\ \mathbf{S_T}\mathbf{B}^{R,nd} = -\mathbf{B}^{R,nd}\mathbf{S}^{R,nd} \end{cases} \tag{5.39}$$

5.5.1 Existence of $\mathbf{S}^H$ *and* $\mathbf{S}^{R,nd}$

From (5.39) it immediately follows that $\mathbf{S}^H = \mathbf{0}$, i.e., $\mathbf{Q}^H(t) = e^{\mathbf{0}} = \mathbf{I}$ is an identity matrix. Furthermore, substitution of (5.26) into $\mathbf{S_T}\mathbf{B}^{R,nd}$ leads to

$$\mathbf{S_T}\mathbf{B}^{R,nd} = \omega_3 \begin{bmatrix} 0 & -1 & 0 & 0 & 0 \\ 1 & 0 & 0 & 0 & 0 \\ 0 & 0 & 0 & 0 & 0 \\ 0 & 0 & 0 & 0 & -1 \\ 0 & 0 & 0 & 1 & 0 \end{bmatrix} \begin{bmatrix} 0 & & 0 \\ 0 & & 0 \\ B_{1,z} & \cdots & B_{nd,z} \\ 0 & & 0 \\ 0 & & 0 \end{bmatrix} = \mathbf{0} \tag{5.40}$$

It follows from (5.40) and the third equation in (5.39) that $\mathbf{S}^{R,nd} = \mathbf{0}$ since $\mathbf{B}^{R,nd}$ is a non zero matrix. Therefore, $\mathbf{Q}^{R,nd}(t) = e^{\mathbf{0}} = \mathbf{I}$.

5.5.2 Existence of $\mathbf{S}^{R,2nr}$

From the second equation in (5.39) we can see that the transformation $\mathbf{S}^{R,2nr}$ should take place between each paired $\mathbf{B}^{R,1/2}$. Therefore, it suggests $\mathbf{S}^{R,2nr}$ admit a form

$$\mathbf{S}^{R,2nr} = blckdiag\left(\mathbf{S}_i^{R,1/2}\right), \quad i = 1, 2, 3, \cdots, nr \tag{5.41}$$

where *blckdiag* denotes that $\mathbf{S}^{R,2nr}$ is a block diagonal matrix composed of $\mathbf{S}_i^{R,1/2}$.
$\mathbf{S}_i^{R,1/2}$ is a 2 by 2 matrix corresponding to each repeated mode pair $\mathbf{B}_i^{R,1/2}$ in (5.39). Substitution (5.41) into the second equation of (5.39) leads to nr's separated equations.

$$\mathbf{S_T}\mathbf{B}_i^{R,1/2} = -\mathbf{B}_i^{R,1/2}\mathbf{S}_i^{R,1/2}, \quad i = 1, 2, 3, \cdots nr \tag{5.42}$$

For simplicity, let us drop the superscript $R, 1/2$ for now. In (5.42), since $\mathbf{B}_i$ are comprised of two linearly independent bearing deformation vectors contributed by ith repeat mode

pair it is always possible to find a left inverse $\mathbf{B}_i^\dagger = (\mathbf{B}_i^T\mathbf{B}_i)^{-1}\mathbf{B}_i^T$ such that

$$\mathbf{B}_i^\dagger \mathbf{B}_i = \mathbf{I}_{2\times 2} \tag{5.43}$$

Substitution (5.43) into (5.42) leads to

$$-\mathbf{B}_i^\dagger \mathbf{S_T} \mathbf{B}_i = \mathbf{S}_i \tag{5.44}$$

Thus we can find every $\mathbf{S}_i$ by the same procedure from (5.42) to (5.44). In fact, it is shown in (5.25) that $\mathbf{B}_i$ are comprised by two orthogonal vectors, i.e., $\mathbf{B}_i^T\mathbf{B}_i = c_i\mathbf{I}$ for some constant $c_i > 0$, such that

$$\mathbf{B}_i^\dagger = (\mathbf{B}_i^T\mathbf{B}_i)^{-1}\mathbf{B}_i^T = \frac{1}{c_i}\mathbf{B}_i^T \tag{5.45}$$

As a result, (5.44) becomes $-1/c_i\mathbf{B}_i^T\mathbf{S_T}\mathbf{B}_i$ which is a skew symmetric matrix since $\mathbf{S_T}$ is skew symmetric.

Because $c\mathbf{B}_i^T\mathbf{S_T}\mathbf{B}_i$ is a 2 by 2 skew symmetric matrix and $\mathbf{B}_i^T\mathbf{B}_i = c_i\mathbf{I}$ so (5.44) admits the form

$$\mathbf{S}_i = -\frac{1}{c_i}\mathbf{B}_i^T\mathbf{S_T}\mathbf{B}_i = \pm\begin{bmatrix} 0 & \omega_3 \\ -\omega_3 & 0 \end{bmatrix} \tag{5.46}$$

We can determine the sign by properly define the sequential order that the repeated modes are retained. If we adopt the conventional sequential ordering defined in (5.25), we will have + sign. Consequently, $\mathbf{Q}^{R,2nr}$ becomes

$$\begin{aligned} \mathbf{Q}^{R,2nr} &= \exp[(\mathbf{S}^{R,2nr})t] \\ &= \exp[blckdiag\left(\mathbf{S}_i^{R,1/2}\right)t] \\ &= blckdiag\left(\begin{bmatrix} \cos\omega_3 t & \sin\omega_3 t \\ -\sin\omega_3 t & \cos\omega_3 t \end{bmatrix}_i\right) \qquad i = 1,2,3,\cdots,nr \end{aligned} \tag{5.47}$$

Altogether, the coordinate transformation $\mathbf{Q}(t)$ is thus found as

$$\begin{aligned} \mathbf{Q}(t) &= \mathbf{Q}^H \oplus \mathbf{Q}^{R,2nr} \oplus \mathbf{Q}^{R,nd} \\ &= \mathbf{I}_{nH\times nH} \oplus blckdiag\left(\begin{bmatrix} \cos\omega_3 t & \sin\omega_3 t \\ -\sin\omega_3 t & \cos\omega_3 t \end{bmatrix}_i\right) \oplus \mathbf{I}_{nd\times nd} \qquad i = 1,2,3,\cdots,nr \end{aligned} \tag{5.48}$$

5.6 Commutativity between Q, K, *and* G

Thus far, we have proved the first equation in (5.33). If we could prove the last two equations, the transformed equations of motion (5.32) will have constant coefficients. From (5.32), the most intuitive way to have $\mathbf{Q}$ satisfy the last two equations would be that $\mathbf{Q}$ is commutative with $\mathbf{K}$ and $\mathbf{G}$. In this case, the last two equations in (5.33) will be satisfied as such.

$$\begin{cases} \mathbf{Q}^{-1}(t)\mathbf{K}\mathbf{Q}(t) = \mathbf{Q}^{-1}(t)\mathbf{Q}(t)\mathbf{K} = \mathbf{K} \\ \mathbf{Q}^{-1}(t)\mathbf{G}\mathbf{Q}(t) = \mathbf{Q}^{-1}(t)\mathbf{Q}(t)\mathbf{G} = \mathbf{G} \end{cases} \tag{5.49}$$

It is possible to do so because the coordinate transformation $\mathbf{Q}(t)$ (5.48), the stiffness softening matrix $\mathbf{K}_\lambda$ (5.2), and the gyroscopic matrix $\mathbf{G}_{22}$ (5.3) both admit patterned structures associated with the repeated modes. From (5.48), the housing modes, repeated modes, and distinct modes are all decoupled in $\mathbf{Q}$. Similarly, they are also decoupled in $\mathbf{K}_\lambda$ and $\mathbf{G}_{22}$ based on (5.2) and (5.3) and [27]. That is, the housing modes, repeated modes, and distinct modes constitute three independent subspaces. Therefore, we can write $\mathbf{K}$ and $\mathbf{G}$ as the direct summation of the subspaces (cf. (5.48)).

$$\begin{cases} \mathbf{K} = \mathbf{0}^H \oplus [\boldsymbol{\omega}^{R,2nr} - \mathbf{K}_\lambda^{2nr}] \oplus [\omega^{R,nd} - \mathbf{K}_\lambda^{nd}] \\ \mathbf{G} = \mathbf{0}^H \oplus \mathbf{G}_{22}^{2nr} \oplus \mathbf{G}_{22}^{nd} \end{cases} \tag{5.50}$$

As a result, the matrix multiplication $\mathbf{K}\mathbf{Q}(t)$ and $\mathbf{G}\mathbf{Q}(t)$ occur at individual subspaces. Since the transformation between the housing modes and distinct modes are trivial (both of $\mathbf{Q}^H$ and $\mathbf{Q}^{R,nd}$ are identity matrices), it is sufficient to prove that commutativity occurs at the repeated modes. Let us also decompose $\mathbf{G}$ and $\mathbf{K}$ into three subspaces separating housing, distinct, and repeated modes as follow.

$$\mathbf{G} = \mathbf{0} \oplus \mathbf{G}^{nd} \oplus \mathbf{G}^{2nr} \tag{5.51}$$

and

$$\mathbf{K} = \boldsymbol{\omega}^H \oplus [\boldsymbol{\omega}^{R,nd} - \omega_3^2\mathbf{K}_\lambda^{nd}] \oplus [\boldsymbol{\omega}^{R,2nr} - \omega_3^2\mathbf{K}_\lambda^{2nr}] \tag{5.52}$$

where $\mathbf{G}^{,nd} \oplus \mathbf{G}^{2nr}$ is the decomposition of $\mathbf{G}_{22}$ in (5.2), $[\boldsymbol{\omega}^{R,nd} - \omega_3^2\mathbf{K}_\lambda^{nd}] \oplus [\boldsymbol{\omega}^{R,2nr} - \omega_3^2\mathbf{K}_\lambda^{2nr}]$ is the decomposition of (5.3) and $\boldsymbol{\omega}^H$ is equal to $\boldsymbol{\omega}^H$ (5.3).

First of all, $\boldsymbol{\omega}^{R,2nr}\mathbf{Q}^{R,2nr} = \mathbf{Q}^{R,2nr}\boldsymbol{\omega}^{R,2nr}$ is trivially satisfied because each paired repeated modes have same natural frequency so it follows that $\boldsymbol{\omega}^{R,2nr}\mathbf{Q}^{R,2nr} = \omega_{nr}^{R}\mathbf{I}\mathbf{Q}^{R,2nr} = \mathbf{Q}^{R,2nr}\omega_{nr}^{R}\mathbf{I} = \mathbf{Q}^{R,2nr}\boldsymbol{\omega}^{R,2nr}$.

Next, the commutativity between $\mathbf{K}_{\lambda}^{2nr}$, $\mathbf{G}_{22}^{2nr}$ and $\mathbf{Q}^{R,2nr}$ is proved as follows. Let us first examine the structure of $\mathbf{K}_{\lambda}^{2nr}$ and $\mathbf{G}_{22}^{2nr}$ associated with repeated modes. Also, let us define a pair of real repeated modes $\mathbf{W}^{p,\mathcal{R}}$ and $\mathbf{W}^{p,\mathcal{I}}$ by the pth paired complex modes $\mathbf{W}_{n=1}^{p,\mathcal{C}}$ and $\mathbf{W}_{n=N-1}^{p,\mathcal{C}}$ with phase indices $n = 1$ and $n = N - 1$.

$$\begin{bmatrix} \mathbf{W}^{p,\mathcal{R}} \\ \mathbf{W}^{p,\mathcal{I}} \end{bmatrix} = \frac{\sqrt{2}}{2}\begin{bmatrix} 1 & 1 \\ -j & j \end{bmatrix}\begin{bmatrix} \mathbf{W}_{n}^{p,\mathcal{C}} \\ \mathbf{W}_{-n}^{p,\mathcal{C}} \end{bmatrix} \qquad p \in nr \tag{5.53}$$

Please note that since phase indices $n = 1$ and $n = N-1$ presenting the complex conjugate pairs, the subscripts are replaced with n and $-n$ for simplicity. Also, the superscripts $\mathcal{R}$ and $\mathcal{I}$ are replaced with 1 and 2 as well. That is, $\mathbf{W}^{p,\mathcal{R}} = \mathbf{W}^{p_1}$ and $\mathbf{W}^{p,\mathcal{I}} = \mathbf{W}^{p_2}$.

Also, vibration mode shapes of a stationary, cyclic symmetric rotor can be expanded in terms of a Fourier series [3] (also see (4.15)):

$$\mathbf{W}^{R}(\tilde{\mathbf{r}}) = \sum_{k=n+\mathbf{M}(N)} \mathbf{A}_k(r,z)e^{jk\theta} \tag{5.54}$$

where $\mathbf{M}(N)$ denotes an integer multiple of N and $\mathbf{A}_k(r,z)$ are the Fourier coefficients.

5.6.1 Commutativity between $\mathbf{K}_{\lambda}^{2nr}$ and $\mathbf{Q}^{R,2nr}$

With (5.53), $\mathbf{K}_{\lambda}^{2nr}$ can be calculated in terms of two arbitrary repeated mode pairs p and q where $p, q \in nr$. $\mathbf{K}_{\lambda}(p_1, q_2)$ and $\mathbf{K}_{\lambda}(p_2, q_1)$ are calculated as follows.

$$\begin{aligned} \mathbf{K}_{\lambda}(p_1,q_2) = \lambda_{p_1q_2} &\equiv \delta_{p_1q_2} - \int W_z^{p_1}(\tilde{\mathbf{r}})W_z^{q_2}(\tilde{\mathbf{r}})dm \\ &= -\frac{1}{2}\int [jW_{-n,z}^{p,\mathcal{C}}W_{n,z}^{q,\mathcal{C}} - jW_{n,z}^{p,\mathcal{C}}W_{-n,z}^{q,\mathcal{C}}]dm \end{aligned} \tag{5.55}$$

and

$$\begin{aligned} \mathbf{K}_{\lambda}(p_2,q_1) = \lambda_{p_2q_1} &\equiv \delta_{p_2q_1} - \int W_z^{p_2}(\tilde{\mathbf{r}})W_z^{q_1}(\tilde{\mathbf{r}})dm \\ &= -\frac{1}{2}\int [jW_{n,z}^{p,\mathcal{C}}W_{-n,z}^{q,\mathcal{C}} - jW_{-n,z}^{p,\mathcal{C}}W_{n,z}^{q,\mathcal{C}}]dm \end{aligned} \tag{5.56}$$

In substitution of (5.53) into (5.55) and (5.56), terms associated with $\int W^{\mathcal{C}}_{n,z} W^{\mathcal{C}}_{n,z} dm$ or $\int W^{\mathcal{C}}_{-n,z} W^{\mathcal{C}}_{-n,z} dm$ vanish because every repeated mode pair has phase index $2n \neq M(N)$ resulting $\int e^{jk\theta} = 0, \;\; k \neq 0$ in (5.54).

There are two different scenarios between p and q; that is, $p \neq q$ or $p = q$. For the first scenario, $p \neq q$, from (5.55) and (5.56), it immediately follows that $\lambda_{p_1 q_2} = -\lambda_{p_2 q_1}$. Furthermore, for the second scenario, $p = q$, it follows that $\lambda_{p_1 q_2} = \lambda_{p_2 q_1} = 0$.

Since repeated modes only differ by a rigid body rotation the integrations of $\mathbf{K}_\lambda(p_1, q_1)$ and $\mathbf{K}_\lambda(p_2, q_2)$ between mode p_1 and q_1 and that between p_2 and q_2 are identical. As a result, $\lambda_{p_2 q_2} = \lambda_{p_1 q_1}$ for $p \neq q$ or $p = q$.

In sum, $\mathbf{K}^{2nr}_\lambda$ only contains two types of block matrices. When the block matrix is at off diagonal, it admits the form

$$\begin{bmatrix} a & -b \\ b & a \end{bmatrix} \tag{5.57}$$

and when it is at diagonal, it admits the form

$$\begin{bmatrix} c & 0 \\ 0 & c \end{bmatrix} \tag{5.58}$$

for some constants a, b, and c.

It can be easily shown that (5.57) and (5.58) commute with the block matrix in $\mathbf{Q}^{R,2nr}$ (5.47) and therefore $\mathbf{K}^{2nr}_\lambda$ commutes with $\mathbf{Q}^{2nr}$.

Hence, the proof of the commutativity between $\mathbf{K}^{2nr}_\lambda$ and $\mathbf{Q}^{R,2nr}$ is complete. Furthermore, the proof can be verified numerically by using the benchmark model. Table 5.1 shows the numerically computed $\mathbf{K}^{2nr}_\lambda$ of 3 representative pairs of repeated modes, including one paired rocking modes, one paired translational modes, and one paired elastic (1,0) modes[1] obtained from the FEA rotor model in Fig. 3.5.

It is clearly shown in Table 5.1 that the block matrices between each pair of repeated modes in $\mathbf{K}^{2nr}_\lambda$ admit the form described in (5.57) and (5.58) despite of minor numerical error.

[1]Here adopts the same notation of modes from Chap. 3 and Chap. 4.

Table 5.1: Numerical Values of $\mathbf{K}_{\lambda}^{2nr}$ of Representative Repeated Modes. The Numerical values are Rounded to Three Effective Digits.

Mode Type	Rocking Mode about x	Rocking Mode about y	Translation in x	Translation in y	(1,1) Mode 1	(1,1) Mode 2
Rocking Mode about x	2.74e-04	-2.17e-14	0.00e+00	0.00e+00	2.59e-04	-3.15e-04
Rocking Mode about y	-2.17e-14	2.74e-04	0.00e+00	0.00e+00	3.15e-04	2.56e-04
Translation in x	0.00e+00	0.00e+00	1.00e+00	0.00e+00	0.00e+00	0.00e+00
Translation in y	0.00e+00	0.00e+00	0.00e+00	1.00e+00	0.00e+00	0.00e+00
(1,1) Mode 1	2.59e-04	3.15e-04	0.00e+00	0.00e+00	9.22e-04	1.82e-09
(1,1) Mode 2	-3.15e-04	2.59e-04	0.00e+00	0.00e+00	1.82e-09	9.22e-004

5.6.2 Commutativity between $\mathbf{G}_{22}$ *and* $\mathbf{Q}^{R,2nr}$

Proof of the commutativity in this section is analogue to what has been done in the last section. First of all, we calculate $\mathbf{G}_{22}(p_1, q_2)$ and $\mathbf{G}_{22}(p_2, q_1)$ as follows.

$$\begin{aligned}\mathbf{G}_{22}(p_1, q_2) = g_{p_1 q_2} &\equiv \frac{\mathbf{k}}{2} \cdot \int \mathbf{W}^{q_2}(\tilde{\mathbf{r}}) \times \mathbf{W}^{p_1}(\tilde{\mathbf{r}}) dm \\ &= \frac{\mathbf{k}}{2} \cdot \int [-j\mathbf{W}_n^{q,\mathcal{C}} \times \mathbf{W}_{-n}^{p,\mathcal{C}} + j\mathbf{W}_{-n}^{q,\mathcal{C}} \times \mathbf{W}_n^{p,\mathcal{C}}] dm\end{aligned} \tag{5.59}$$

and

$$\begin{aligned}\mathbf{G}_{22}(p_2, q_1) = g_{p_2 q_1} &\equiv \frac{\mathbf{k}}{2} \cdot \int \mathbf{W}^{q_1}(\tilde{\mathbf{r}}) \times \mathbf{W}^{p_2}(\tilde{\mathbf{r}}) dm \\ &= \frac{\mathbf{k}}{2} \cdot \int [j\mathbf{W}_n^{q,\mathcal{C}} \times \mathbf{W}_{-n}^{p,\mathcal{C}} - j\mathbf{W}_{-n}^{q,\mathcal{C}} \times \mathbf{W}_n^{p,\mathcal{C}}] dm\end{aligned} \tag{5.60}$$

It follows that from (5.59) and (5.60) $g_{p_1 q_2} = -g_{p_2 q_1}$ for either $p = q$[2] or $p \neq q$. Consequently, the block matrices of $\mathbf{G}_{22}^{2nr}$ all take the form similar to (5.57). In particular, when block matrix is at off diagonal, it is exactly the same with (5.57). When it is at diagonal, it is the same with (5.57) except $a = 0$ because $\mathbf{G}_{22}^{2nr}$ is skew symmetric. As a result, $\mathbf{G}_{22}^{2nr}$ commutes with $\mathbf{Q}^{2nr}(t)$ sharing the same reason with that $\mathbf{K}_{\lambda}^{2nr}$ does with $\mathbf{Q}^{2nr}(t)$.

Similarly, the proof can be verified numerically by using the benchmark model once again. Table 5.2 shows the numerically computed $\mathbf{G}_{22}^{2nr}$ of the same representative pairs

[2]The case $p = q$ is trivial to prove because $\mathbf{G}_{22}^{2nr}$ is skew symmetric.

Table 5.2: Numerical Values of $\mathbf{G}_{22}^{2nr}$ of Representative Repeated Modes. The Numerical values are Rounded to Three Effective Digits.

Mode Type	Rocking Mode about x	Rocking Mode about y	Translation in x	Translation in y	(1,1) Mode 1	(1,1) Mode 2
Rocking Mode about x	0.00e+00	-2.74e-04	-4.12e-17	0.00e+00	-2.16e-04	-1.77e-04
Rocking Mode about y	2.74e-04	0.00e+00	0.00e+00	-4.12e-17	1.77e-04	-2.16e-04
Translation in x	4.12e-17	0.00e+00	0.00e+00	-1.00e-00	5.95e-11	1.14e-10
Translation in y	0.00e+00	4.12e-17	1.00e-00	0.00e+00	1.71e-10	-1.97e-10
(1,1) Mode 1	2.16e-04	-1.77e-04	-5.95e-11	-1.71e-10	0.00e+00	-6.65e-04
(1,1) Mode 2	1.77e-04	2.16e-04	-1.14e-10	1.97e-10	6.65e-04	0.00e+00

of repeated modes. It is clearly shown in Table 5.2 that the block matrices of $\mathbf{G}_{22}^{2nr}$ also comply with (5.57).

5.7 Discussions

5.7.1 Discussion on Transformed Equations of Motion

In the previous two sections, $\mathbf{Q}(t)$ in (5.48) has been proved transform the equations of motion (5.1) into constant coefficients (5.32). To find the explicit form of the transformed equations we notice that (5.32) have constant coefficients. Thus, one can substitute any convenient time t into (5.32) to obtain the explicit form. One such time will be the reference time $t = 0$. By substituting $t = 0$ into (5.28) and (5.32) leads to the transformed equations of motion.

$$\begin{cases} \ddot{\mathbf{q}}' = -\left[\mathbf{G} + 2\mathbf{S}\right]\dot{\mathbf{q}}' - \left[\mathbf{K} + \mathbf{GS} + \mathbf{K}^B(0) + \mathbf{S}^2\right]\mathbf{q}' \\ \mathbf{q} = \mathbf{Q}(t)\mathbf{q}' \end{cases} \tag{5.61}$$

In the first equation of (5.61), all the coefficients are constant. In particular, $\mathbf{K}^B(0)$ is constant because $t = 0$ is specified. Also, $\mathbf{S}$ is defined in (5.30).

There are several things worth discussing regarding (5.61). First of all, since the first equation in (5.61) has constant coefficients, it can be solved as eigenvalue problems to obtain $\mathbf{q}'$.

Secondly, let us consider the case when spin speed ω_3 is slow. When ω_3 is slow $\mathbf{K}_\lambda$ in $\mathbf{K}$, $\mathbf{G}$, $\mathbf{S}$, and $\mathbf{S}^2$ are small and can be ignored. In this regard, (5.61) can be reduced to have approximate solutions $\mathbf{q}^*$ by solving the reduced equations of motion.

$$\begin{cases} \ddot{\tilde{\mathbf{q}}} = -\left[\tilde{\mathbf{K}} + \mathbf{K}^B(0)\right] \tilde{\mathbf{q}} \\ \mathbf{q}^* = \mathbf{Q}(t)\tilde{\mathbf{q}} \end{cases} \tag{5.62}$$

where

$$\tilde{\mathbf{K}} = \begin{bmatrix} \boldsymbol{\omega}^H & \mathbf{0} \\ \mathbf{0} & \boldsymbol{\omega}^R \end{bmatrix} \tag{5.63}$$

From (5.62) and (5.63), we notice that $\tilde{\mathbf{q}}$ is the response of the system when it is at rest. By solving (5.62) we obtain the eigenvalues of the system. Generally speaking, when the rotor is at rest, the system has two major groups of eigenvalues, the rotor-dominant modes $\tilde{\omega}^{(R)}$ and housing dominant modes $\tilde{\omega}^{(H)3}$. Let us consider a housing-dominant mode $\tilde{\omega}^{(H)}$ with rotor response of paired repeated modes $\tilde{q}_1^R$ and $\tilde{q}_2^R$ with some arbitrary amplitudes and phases.

$$\begin{aligned} \tilde{q}_1^R &= A\cos(\tilde{\omega}^{(H)}t + \psi) \\ \tilde{q}_2^R &= B\cos(\tilde{\omega}^{(H)}t + \phi) \end{aligned} \tag{5.64}$$

To obtain the approximated response $q_1^{R^*}$ and $q_2^{R^*}$ we apply (5.48) to inverse transform (5.65) with manipulation of trigonometric identity.

---

[3]First introduced in Subsec. 4.1.1

$$\begin{bmatrix} q_1^{R^*} \\ q_2^{R^*} \end{bmatrix} = \begin{bmatrix} \cos\omega_3 t & \sin\omega_3 t \\ -\sin\omega_3 t & \cos\omega_3 t \end{bmatrix} \begin{bmatrix} \tilde{q}_1^R \\ \tilde{q}_2^R \end{bmatrix} \tag{5.65}$$

$$= \begin{bmatrix} \cos\omega_3 t & \sin\omega_3 t \\ -\sin\omega_3 t & \cos\omega_3 t \end{bmatrix} \begin{bmatrix} A\cos(\tilde{\omega}^H t + \psi) \\ B\cos(\tilde{\omega}^H t + \phi) \end{bmatrix}$$

$$= \begin{bmatrix} C\cos(\tilde{\omega}^H t - \omega_3 t + \psi) + C\cos(\tilde{\omega}^H t + \omega_3 t + \psi) \\ -C\sin(\tilde{\omega}^H t + \omega_3 t + \phi) + C\sin(\tilde{\omega}^H t - \omega_3 t + \phi) \end{bmatrix}$$

$$+ \begin{bmatrix} D\sin(\tilde{\omega}^H t + \omega_3 t + \psi) - D\sin(\tilde{\omega}^H t - \omega_3 t + \psi) \\ D\cos(\tilde{\omega}^H t - \omega_3 t + \phi) + D\cos(\tilde{\omega}^H t - \omega_3 t + \phi) \end{bmatrix} \tag{5.66}$$

where $C = A/2$ and $D = B/2$.

As seen in (5.66), the housing dominant mode has the frequency splitting $\pm\omega_3$ for the rotor response of a pair of repeated modes, which agree with the numerical simulation and the perturbed solutions obtained in Sec. 4.1. Furthermore, since the frequency splitting $\pm\omega_3$ results from the coordinate transformation $\mathbf{Q}(t)$, the theoretical analysis done in Sec. 4.1 also correctly refers to the splitting as the *Gyroscopic Splitting*[4].

Lastly, the transformed system of equations (5.62) is a gyroscopic system with constant coefficients. As discussed in Sec. 3.1, such a system is stable unless the stiffness matrix loses the positive definiteness. Therefore, the instability tends to occur at extremely high speed after the stiffness matrix loses the positive definiteness due to centrifugal softening effects. In Sec. 3.2, the benchmark example has all the instabilities occur at extremely high spin speed. It is confirmed that the mechanism of instabilities are indeed due to the loss of positive definiteness.

5.7.2 Numerical Verification

In order to verify the closed-form solutions, we perform two numerical simulations employing the benchmark model. In the first simulation, the instabilities of the equations of motion and

[4]In Sec. 4.1, the frequency splitting $\pm\omega_3$ was referred to as the *Gyroscopic Splitting* because the perturbed solutions originated from the gyroscopic matrix of the coordinate transformation $\mathbf{T}(t)$ in (2.37), Subsec. 2.6.1.

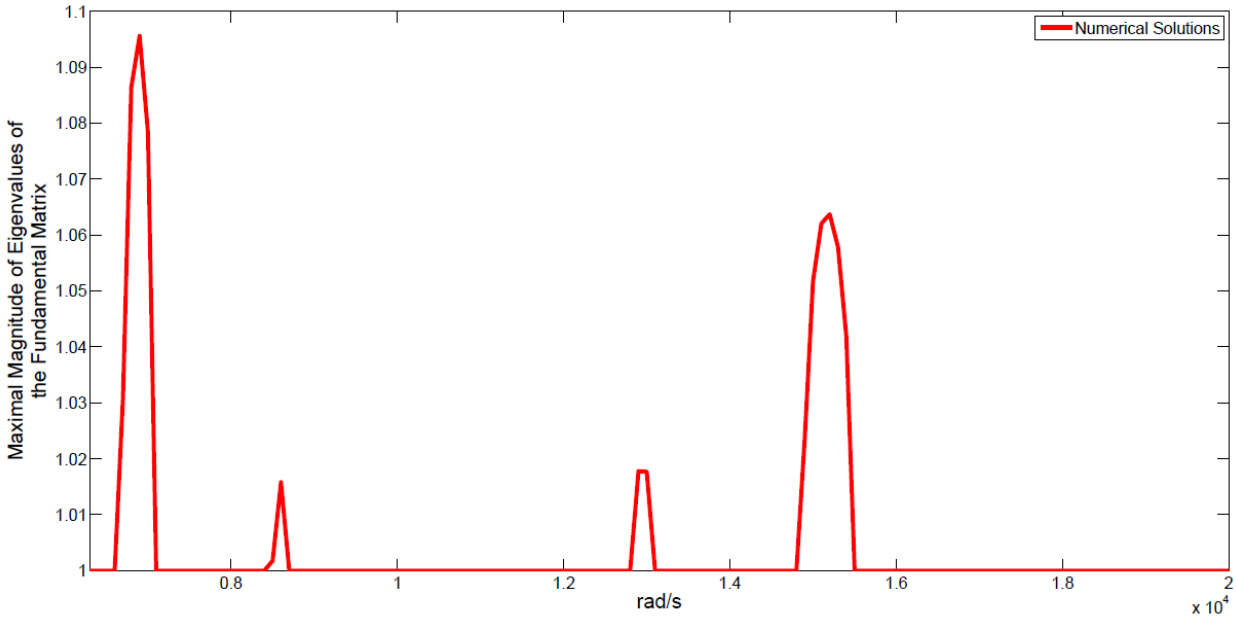

Figure 5.3: Numerical Instabilities Predicted by Solving the Periodic Equation of Motion Numerically. The Instabilities are Determined by Unity of the Maximal Magnitude of Eigenvalues of the Fundamental Matrix. 34 Modes are Retained.

the transformed equations are compared with each other. The former is numerical integrated over one period to obtain the eigenvalues of the fundamental matrix while the latter is solved to obtain eigenvalues of the time invariant gyroscopic system. As aforementioned, the instabilities of the equations of motion depend on the unity of the eigenvalues of the fundamental matrix. In contrast to the time variant system, the instabilities of the time invariant system can be determined by the positiveness of real part of eigenvalues. Figure 5.3 and Fig. 5.4 show the absolute value of the maximal eigenvalue of the fundamental matrix and that of the transformed equations respectively. Both Fig. 5.3 and Fig. 5.4 show exactly the same instabilities with identical bandwidth and spin speeds where they occur.

In the second simulation, the FFT of free responses are compared. In order to justify the simulation, both the equations of motion (5.1) and transformed equations (5.61) are solved by the same numerical scheme, given the same initial conditions $\mathbf{q}(0)$. Eqn. (5.1) is integrated numerically to obtain time domain responses whose FFT are later calculated

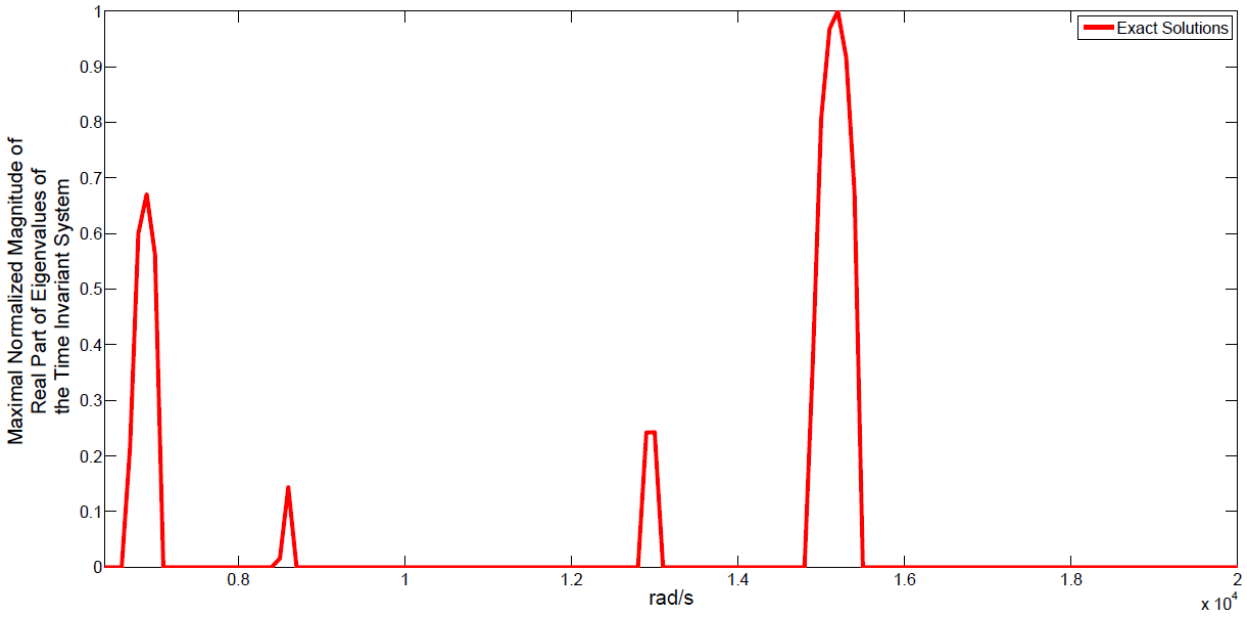

Figure 5.4: Exact Instabilities Predicted by Solving the Eigenvalue Problem of the Transformed, Time Invariant Equation of Motion. The Instabilities are Determined by Positiveness of the Maximal Magnitude of Real Part of Eigenvalues of the Time Invariant System. Identical 34 Modes are Retained.

to obtain frequency domain response following the same method introduced in Chap. 4. On the other hand, the FFT of the responses of (5.61) are obtained in three steps. First of all, the transformed equations are also integrated numerically using the same numerical scheme with identical accuracy to obtain transformed, time domain, responses. Next, the responses are inversely transformed by means of (5.61). Finally, the FFT of the responses are calculated in the same manner with (5.1). Figure 5.5 shows the FFT of a representative housing response of both equations respectively. It is evident that the FFT are on top of each other of all spin speeds. Furthermore, the FFT of the rotor-dominant mode $\omega^{(R)}$ remains unchanged with respect to spin speed, which agrees well with the analytical derivation in Subsec. 4.1.1. Similarly, Fig. 5.6 shows the FFT of a representative rotor response. The FFT once again match each other. In addition, the gyroscopic splitting [5] is observed on

[5]First defined in Subsec. 4.1.1.

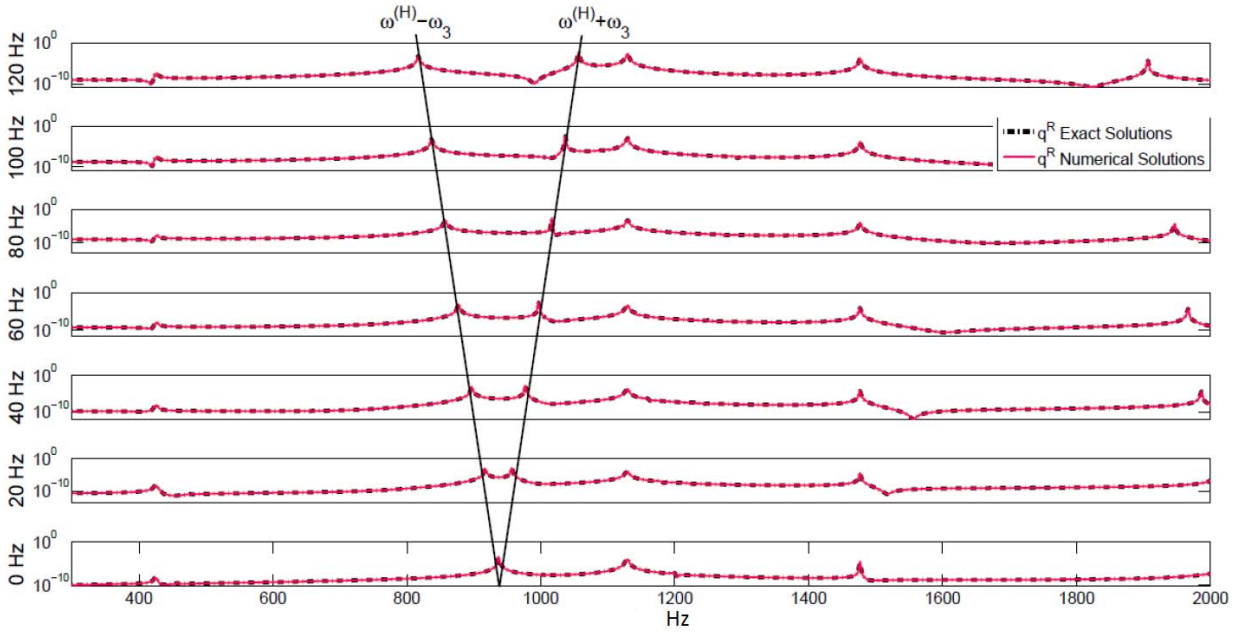

Figure 5.5: FFT of a Housing Response. Comparison between the Numerical and Exact Solutions Reveals the Same FFT solutions. The Gyroscopic Splitting Appears at the Housing-dominant Mode $\omega^{(H)}$. 34 Modes are Retained.

both FFT, which also agrees with the analytical derivation.

In summary, the two numerical simulations successfully verify that (5.1) and (5.61) are indeed equivalent by showing their identical solutions in terms of instabilities and free responses.

5.8 Further Discussion

The discussion thus far not only shows that the benchmark model has the close solutions but bring rise to other aspects of general spinning cyclic symmetric rotor-bearing-housing systems that worth further exploration. The first is the instability at low spin speed. It is proved in the previous sections that if the periodic coefficients in (5.13) completely originate from the repeated modes the equations of motion can be transformed to have constant coefficients by the use of techniques illustrated foregoing. Also, the transformed system is

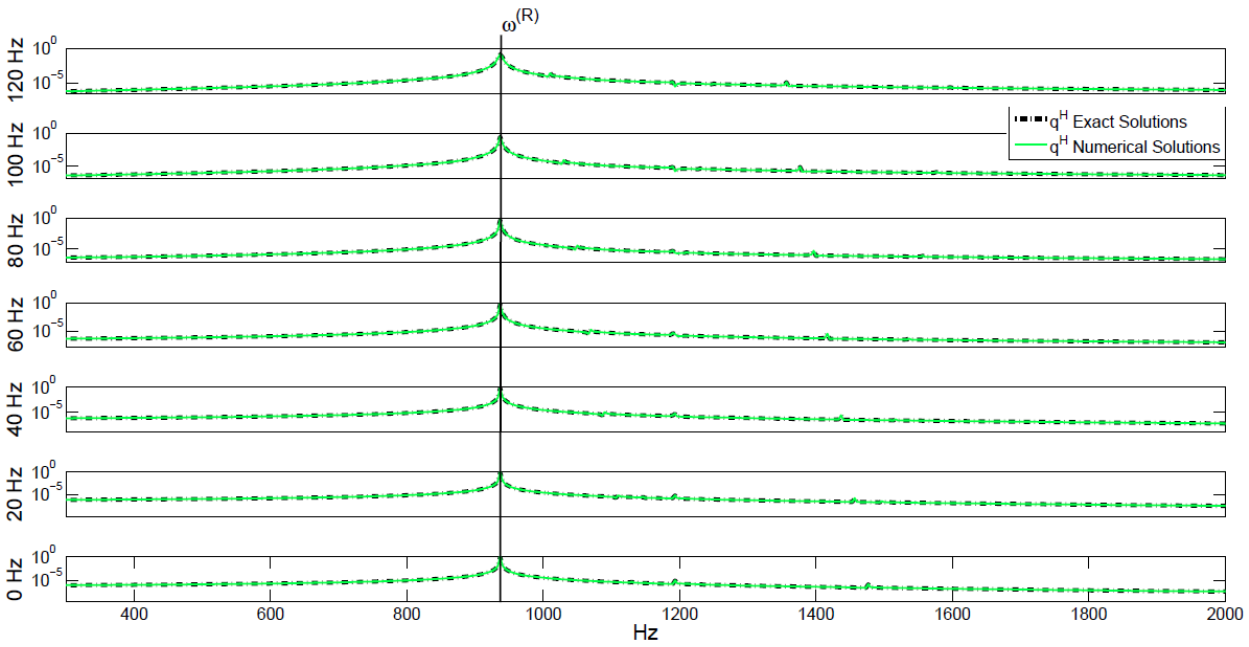

Figure 5.6: FFT of a Rotor Response. Comparison between the Numerical and Exact Solutions Reveal the Same FFT solutions. The Rotor-dominant Mode $\omega^{(R)}$ Appears Unchanged in the Housing Response. 34 Modes are Retained.

a time invariant gyroscopic system which is generally stable at low spin speed. In other words, it is possible for a general spinning, cyclic symmetric rotor-bearing-housing system to have instabilities occur at low spinning speed only when the distinct modes contribute to the periodic coefficients as well. The second is the bearing types. In the development of closed-form solutions, the bearing types are not specified throughout the entire process. Thus, the closed-form solutions are tenable as long as the kinematics assumptions in the early section are still satisfied regardless of bearing types. Therefore, the benchmark model serves as a good example to examine other cyclic symmetric rotor-bearing-housing systems which have different bearing types, such as fluid dynamic bearings, enabling richer dynamic behaviors including periodic damping coefficients where heavy numerical computations are expected. The third is the housing geometry. Similar to bearing types, the housing geometry is not specified in the proof either. Consequently, the square plate in the benchmark can be

replaced with housings with other geometries. One interesting application will be examining the effects of asymmetric housing.

Chapter 6

EXPERIMENTAL STUDY

In order to verify the prediction of the ground-based responses of the system in Subsec. 4.2.1 and 4.2.2, Chapter 4, we conduct experiment study as follows. The experimental study includes three major components. First, we will explain experimental setup and excitation methods. Then we will present experimental results when the rotor is stationary. In particular, frequency response functions (FRFs) are obtained using an automatic hammer and a piezoelectric actuator, respectively. Comparison of the two FRFs helps identify housing-dominant modes, and their mode shapes are subsequently identified. Finally, we conduct experiments to measure ground-based response when the rotor spins at various speeds. Waterfall plots are obtained to confirm evolution of the housing-dominant modes with respect to the spin speed as predicted.

6.1 Experimental Setup

Figure 6.1 shows the rotor-bearing-housing system used in the experiment study. The system is to mimic the benchmark numerical model above as much as possible. The experimental setup consists of three components: a square housing, a spindle motor with ball bearings, and a slotted disk.

The housing is a square plate with a thickness of 4.7 mm and equal width and length of 120 mm. Material of the square plate is Aluminum with Young's modulus of 69 GPa and density of 2700 kg/m^3. The housing has a large circular hole with a diameter of 38 mm at the center to seat the spindle motor. The housing also has four small circular holes at four corners. These small holes have a diameter of 7.26 mm and are located 9.4 mm away from their surrounding edges. The square housing is then supported at the four small circular holes and fastened to an isolation table via four bolts and washers with a pre-load of 4 N-m. The spindle motor is then mounted onto the square housing via three screws with pre-load

of 50 mN-m.

The slotted disk has an inner diameter of 25 mm, an outer diameter of 95 mm, and a thickness of 0.97 mm. Material of the disk is Aluminum with Young's modulus of 69 GPa and density of 2700 kg/m^3. The disk has four evenly spaced radial slots, each of which has length of 15.8 mm and two semi-circular ends of 1.6 mm radius. Since measurements will be made at the outer rim where displacement is the largest, the radial slots do not extend to the outer rim (cf. Fig. 3.6) in order to ensure continuous measured response. The slotted disk is then clamped onto the spindle motor through the central hole.

Figure 6.2 shows the experimental setup. The setup consists of an automatic hammer, a PZT-based piezoelectric actuator, a laser Doppler vibrometer (LDV), an accelerometer, and a spectrum analyzer. The hammer excites the rotor whereas the PZT actuator excites the housing providing two different ways to generate input excitations. The LDV and accelerometer measure response of the rotor and housing, respectively. As introduced in Chapter 1, the conventional excitation method in measuring ground-based response of the system, i.e., using the automatic hammers, may not be sufficient to excite the housing. Therefore, we use piezoeletric (PZT) actuators to excite the system besides the hammers. As result, the swept sine analysis is chosen to be compatible to the use of PZT actuators. Consequently, there are two modes to conduct the experiments.

The first mode is to use the hammer and LDV together. In this mode, the hammer is fixed in the space and taps at the inner rim of the rotor while the LDV aims at the outer rim of the rotor. A load cell at the tip of the hammer measures the excitation force and the LDV measures out-of-plane velocity of the outer rim. Both signals are fed into the spectrum analyzer to obtain an input-output relationship in the frequency domain. We will call this relationship a frequency response function (FRF) for convenience, although FRF does not theoretically exist for such a system because the equation of motion has time-dependent coefficients [3].

The second mode is to use the PZT actuator and LDV. The PZT actuator is attached to the bottom of the housing and driven by a sinusoidal source from the analyzer. At the same time, the LDV measures the velocity at the outer rim. Both the source signal and measured velocity are fed into the spectrum analyzer. A frequency response function is obtained as

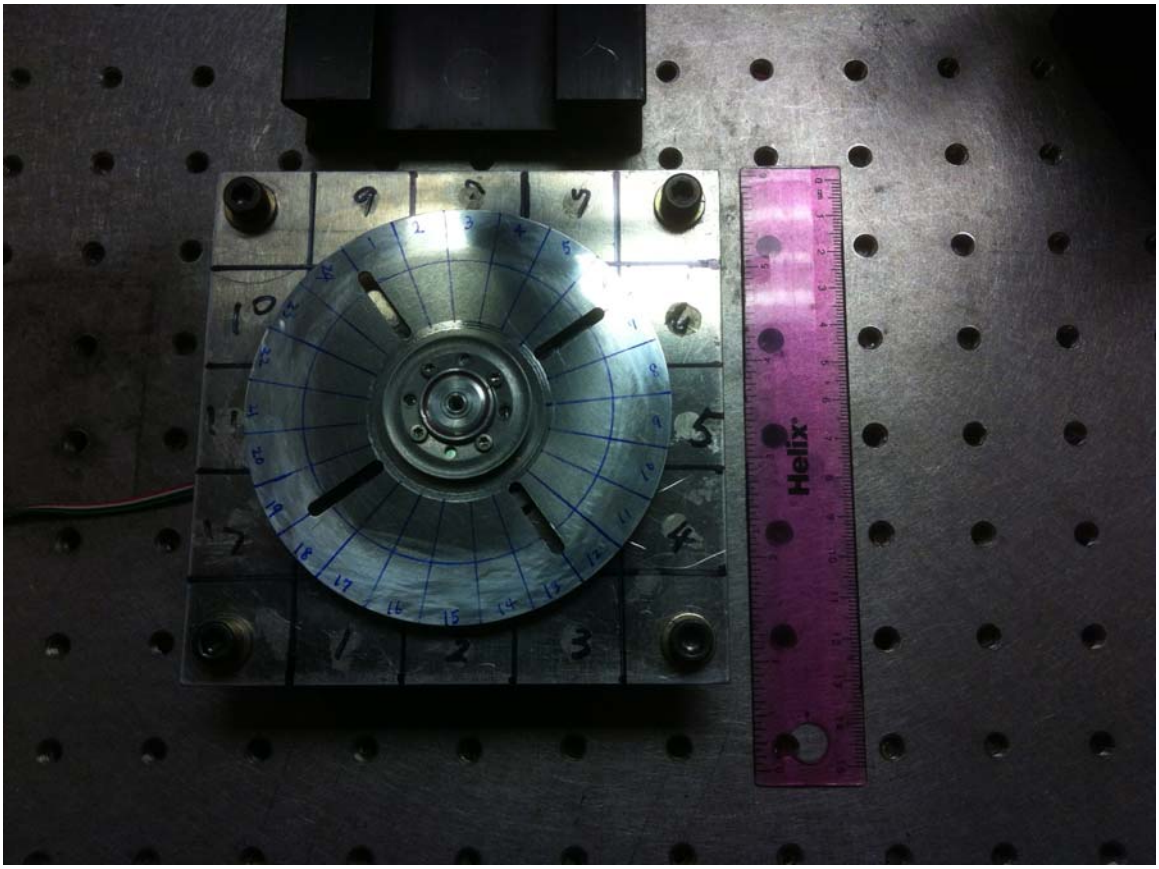

Figure 6.1: The Assembled System: The Slotted Disk, Spindle Motor, and Square Plate

the PZT actuator scans through the frequency domain to complete a swept sine analysis. If the response of the housing is needed, the accelerometer measurement is used in lieu of the LDV measurement.

6.2 Measured Response of Stationary Rotor

Also mentioned in Chapter 1, the ground-based response of a spinning cyclic symmetric rotor-bearing-housing system contain abundant frequency components. In order to facilitate data analysis on experiments on the spinning system, the characteristics of the stationary system should be studied first.

The purpose of this part of the experiment is to identify housing-dominant modes of

the rotor-bearing-housing system in Fig. 6.1 while the rotor is stationary. Two different methods are used to measure FRFs: the automatic impact hammer and the PZT actuator.

Figure 6.4 shows two FRFs obtained from the experiments. The top FRF is obtained via the hammer on rotor and LDV on rotor, whereas the bottom FRF is via the PZT on housing and LDV on rotor. Generally speaking, housing-dominant modes are more difficult to excite from the rotor than the housing. With this clue in mind, we note that the top FRF with rotor excitation has one clear peak near 1400 Hz, denoted by $\Omega^{(R)}$, which corresponds to a rotor-dominant mode. In contrast, there are two small and round peaks near 1300 Hz, denoted by $\Omega_L^{(H)}$ and $\Omega_H^{(H)}$. The magnitude of these two modes is roughly 1 order-of-magnitude less than that of the rotor mode $\Omega^{(R)}$. They could very well be two housing-dominant modes. Moreover, the bottom FRF with housing excitation shows a strong $\Omega_L^{(H)}$ resonance peak further enhancing the likelihood of $\Omega_L^{(H)}$ being a housing-dominant mode.

To prove that $\Omega_L^{(H)}$ and $\Omega_H^{(H)}$ are two housing-dominant modes, we measured mode shapes experimentally as follows.

For the disk, its outer rim is partitioned into twenty-four divisions evenly in the hoop direction. The automatic hammer taps at a fixed position on the inner rim, while the LDV measures the disk response of each division at the outer rim. An FRF is then obtained for each division, and its magnitude and phase at $\Omega_L^{(H)}$ and $\Omega_H^{(H)}$ are mapped out to extract the mode shape along the outer rim.

To measure mode shapes of the plate, we use an accelerometer instead of LDV to reach the plate beneath the disk (see Fig. 6.1). The plate is meshed into twenty equal grids, and the accelerometer is attached to each grid point. Measured FRF from the automatic hammer and acceleration from each grid then gives the mode shapes via the magnitude and phase at $\Omega_L^{(H)}$ and $\Omega_H^{(H)}$.

Figure 6.5 and Fig. 6.6 show the extracted mode shapes for $\Omega_L^{(H)}$ and $\Omega_H^{(H)}$, respectively, with the plate's mode shape on the left and the disk's on the right. The magnitudes of the plate's mode shape and the disk's mode shape are normalized respectively because they have different units. (Please note that the plate and disk are measured in terms of acceleration and velocity respectively.) Based on the measured mode shapes at each division (for disk) and grid point (for plate), Matlab® is used to generate the contour plots shown in Fig. 6.5

and Fig. 6.6 via interpolation. Moreover, the orientation of the plate and disk (e.g., the slots) in Fig. 6.5 and Fig. 6.6 is identical to that of the assembled system physically shown in Fig. 6.1. Note that these two modes are housing-dominant modes, because the plate's mode shapes are much larger after we compare with those of other modes.

There are several issues worth noting in Fig. 6.5 and Fig. 6.6. First of all, phenomena of rotor-housing coupling, such as the frequency splitting in the form of $\Omega^{(H)} \pm (1-k)\omega_3$, result from the rotor's features in the circumferential direction. Despite that the slotted disk in the experiment is somewhat different from the benchmark numerical model (cf. Fig. 3.6), their features in the circumferential direction are identical. For example, both slotted disks have the same phase index and the same mode shape distribution in the circumferential direction. Therefore, the slotted disk in the experiment can be used to verify the theoretical predictions above without any problem.

Second, $\Omega_L^{(H)}$ and $\Omega_H^{(H)}$ modes are characterized by one nodal diameter in the disk and one nodal line in the plate. As a result, the two opposite halves of the plate (or disk) vibrate in an out-of-phase manner, leading to in-plane deformations of the bearings. As demonstrated in the benchmark numerical model, gyroscopic splitting occurs in those housing-dominant modes whose mode shapes of rotors and housings cause bearings in-plane deformation. Therefore, $\Omega_L^{(H)}$ and $\Omega_H^{(H)}$ modes should present frequency splitting $\Omega^{(H)} \pm (1-k)\omega_3$.

Finally, the nodal diameters and nodal lines of $\Omega_L^{(H)}$ and $\Omega_H^{(H)}$ have a phase shift between each other. For example, the nodal diameter of $\Omega_L^{(H)}$ and $\Omega_H^{(H)}$ is along 50° and 120°, respectively. This phenomenon results from asymmetry of the spindle motor and is explained in detail as follows.

Theoretically, the housing in Fig. 6.1 is square and should have two house-dominant modes with repeated natural frequencies. The two repeated modes can be linearly combined in any way, forming a nodal line of arbitrary orientation on the plate. In the experiment, however, the flange of the spindle motor has a cutout to facilitate assembly and electrical routing; see Fig. 6.3 The cutout forms a small perturbation destroying the symmetry of the housing and split the repeated modes in frequency. Therefore, the two housing-dominant modes $\Omega_L^{(H)}$ and $\Omega_H^{(H)}$ now have slightly different frequency as shown in Fig. 6.4. Moreover,

the linear combination cannot be formed arbitrarily, and the nodal line has a fixed orientation. This also explains why $\Omega_H^{(H)}$ mode was not excited in Fig. 6.4 because the PZT actuator was on the nodal line of the $\Omega_H^{(H)}$ mode.

6.3 Measured Response of Spinning Rotor

In the spin test, we aim to obtain waterfall plots consisting of FRFs measured at various spin speeds. The measurements are focused on the two housing-dominant modes.

The goal is to verify that $\Omega_L^{(H)}$ and $\Omega_H^{(H)}$ will split into multiple frequency components $\pm(1-k)\omega_3$. Since the rotor has four evenly spaced slots, the rotor consists of four identical substructures. Therefore, $N = 4$. The disk of $\Omega_L^{(H)}$ and $\Omega_H^{(H)}$ modes has one nodal-diameter. As a result, $n = 1$ or $n = 3$. A quick calculation of $1 - k = 1 - M(N) - n$, where $M(N)$ is multiples of N, shows that the frequency splitting should occur at $\pm 0\omega_3$, $\pm 2\omega_3$, $\pm 4\omega_3$, and so on. This is consistent with the benchmark numerical model above.

Figure 6.7 shows a waterfall plot consisting of multiple FRFs obtained by hammer excitation (on rotor) and LDV pickup (from rotor) with spin speed from 0 to 6000 rpm. The housing dominant modes $\Omega_L^{(H)}$ and $\Omega_H^{(H)}$ do split into primary branches $\Omega_{L-\delta}^{(H)}$ and $\Omega_{H+\delta}^{(H)}$ as well as secondary branches $\Omega_{L-\delta}^{(H)} + 4\omega_3$ and $\Omega_{H+\delta}^{(H)} \pm 4\omega_3$. All the branches are denoted with asymptotes (solid and dash lines) to indicate corresponding frequency splitting. Moreover, peaks of resonance are shown in red circles. Let us analyze the experimental results in detail as follows.

First of all, let us focus on the primary branches. According to the predictions, the primary branches of the housing-dominant modes should take the form of $\Omega^{(H)} \pm 0\omega_3$, i.e., the frequency should not depend on spin speed. In the experiment, however, the primary branch $\Omega_H^{(H)}$ deviates slightly forward and $\Omega_L^{(H)}$ slightly backward as the spin speed changes. Therefore, we use the notation $\Omega_{L-\delta}^{(H)}$ and $\Omega_{H+\delta}^{(H)}$ to denote the slight speed dependence δ, which did not appear in the theoretical predictions. Nevertheless, the value of δ is very small, generally less than 5% of the natural frequency of the housing-dominant modes. For example, when spin speed is 6000 rpm, δ is around 40 Hz for $\Omega_L^{(H)}$ and is 28 Hz for $\Omega_H^{(H)}$.

Although it is not clear exactly what causes the speed dependence δ, a possible source is asymmetry. As explained earlier, $\Omega_L^{(H)}$ and $\Omega_H^{(H)}$ have different natural frequencies because

of the spindle motor asymmetry. Absence of repeated modes may cause the gyroscopic splitting to deviate slightly from $\pm 1\omega_3$. Accordingly, the ground-based response of the rotor could also deviate from the predicted frequency splitting $(1-k)\omega_3$.

Now, let us focus on the secondary branches. With the presence of speed dependence δ, the frequency splitting now becomes $\Omega^{(H)}_{L-\delta} \pm (1-k)\omega_3$ and $\Omega^{(H)}_{H+\delta} \pm (1-k)\omega_3$ for the ground-based rotor response. According to Fig. 6.7, we see two forward branches $\Omega^{(H)}_{L-\delta} + 4\omega_3$ and $\Omega^{(H)}_{H+\delta} + 4\omega_3$ as well as one backward branch $\Omega^{(H)}_{H+\delta} - 4\omega_3$.

Let us focus on the forward branches $\Omega^{(H)}_{L-\delta} + 4\omega_3$ and $\Omega^{(H)}_{H+\delta} + 4\omega_3$ for now. Since their magnitude is much smaller than that of primary branches, these secondary branches may not be distinguishable all the time. For example, between 4800 rpm and 6000 rpm, $\Omega^{(H)}_{H+\delta} + 4\omega_3$ is close to the primary branch of a nearby rotor-dominant mode. Therefore, $\Omega^{(H)}_{H+\delta} + 4\omega_3$ is not recognizable due to its small magnitude compared with the nearby rotor-dominant mode. In this case, we label the secondary branch with a dash line.

For the forward branches, the predictions $\Omega^{(H)}_{L-\delta} \pm (1-k)\omega_3$ and $\Omega^{(H)}_{H+\delta} \pm (1-k)\omega_3$ are quite accurate. Even when the spin speed is 6000 rpm, the measured frequency split between the primary and secondary branches agrees so well with the theoretical prediction $4\omega_3$ that the error is within 1%.

For the backward splitting, only one backward branch $\Omega^{(H)}_{H+\delta} - 4\omega_3$ is observed and its magnitude is quite small. It has the same features as the forward branches. For example, part of the backward branch is not observable, and the splitting $-4\omega_3$ is extremely accurate.

The other backward branch $\Omega^{(H)}_{L-\delta} - 4\omega_3$, however, is not observable in Fig. 6.7. It is not clear why the backward branch did not appear in the experiment. Some observations from Fig. 6.7 suggest that damping may be stronger for backward modes and at higher spin speed. For example, the magnitude of $\Omega^{(H)}_{H+\delta} - 4\omega_3$ is smaller than that of $\Omega^{(H)}_{H+\delta} + 4\omega_3$. Also, the magnitude reduces as spin speed increases, especially for the backward branch $\Omega^{(H)}_{H+\delta} - 4\omega_3$. Maybe the damping is too large thus eliminating the backward branch $\Omega^{(H)}_{L-\delta} - 4\omega_3$.

Finally, we have also measured waterfall plots using the PZT actuator (on housing excitation) and LDV (on rotor pickup). Figure 6.8 shows the measured waterfall plot from 0 rpm to 4800 rpm. There are several things worth noting. First, the primary branches $\Omega^{(H)}_{L-\delta}$ and $\Omega^{(H)}_{H+\delta}$ also have frequency dependence $\pm\delta$, which is consistent with the measurements

from the hammer and LDV. δ in this case is around 31 Hz at $\Omega_L^{(H)}$ and around 20 Hz at $\Omega_H^{(H)}$. Second, $\Omega_{L-\delta}^{(H)}$ and $\Omega_{H+\delta}^{(H)}$ are the most prominent modes compared to other modes in this waterfall plot. This again shows that $\Omega_{L-\delta}^{(H)}$ and $\Omega_{H+\delta}^{(H)}$ are housing dominant modes.

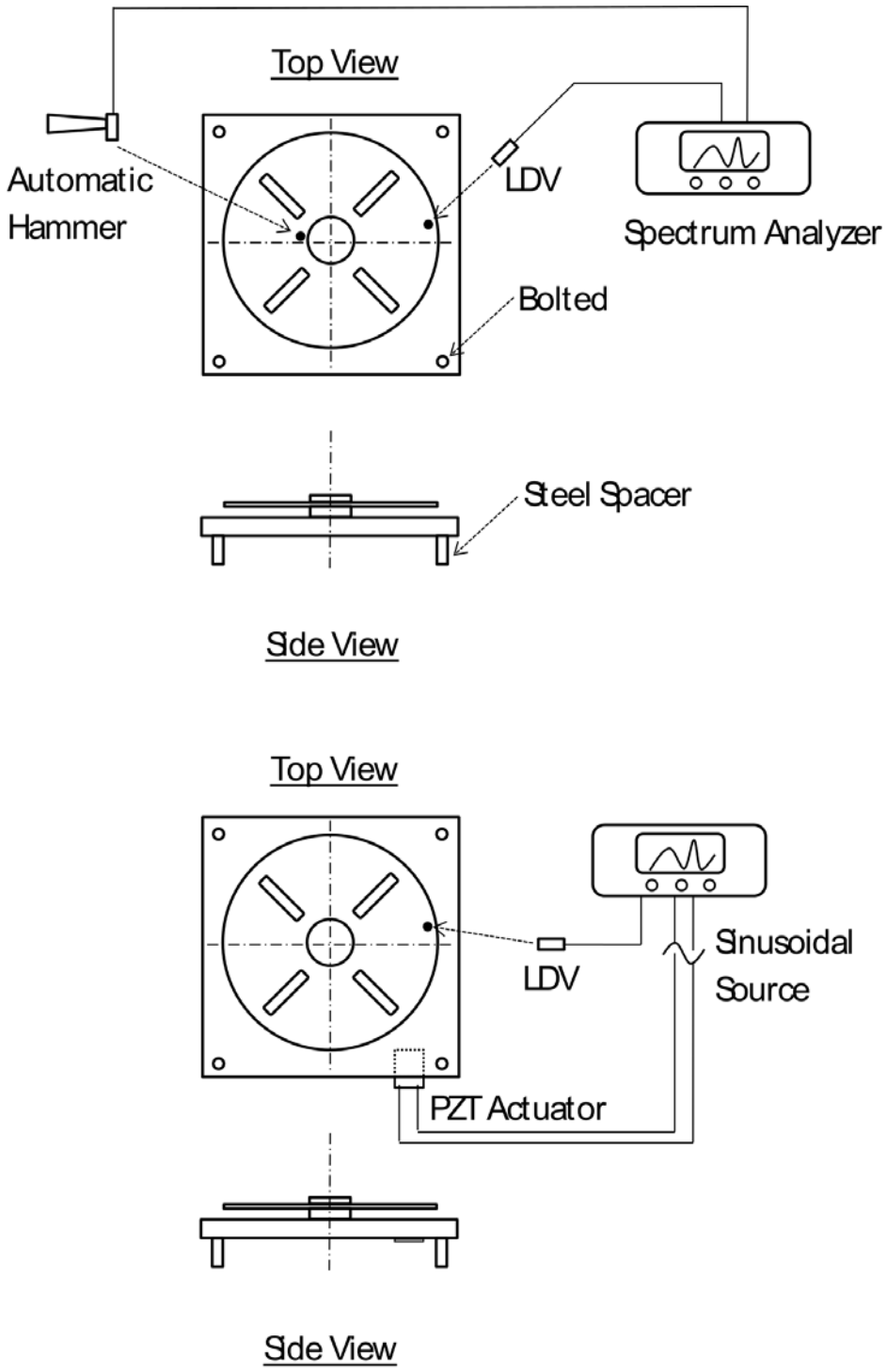

Figure 6.2: The Experiment Set Up. The Upper Schematics: The First Mode LDV/Hammer. The Lower Schematics: The Second Mode LDV/PZT Actuator. The Accelerometer is not Drawn for Simplicity.

Figure 6.3: The Cutout that Causes the Asymmetry on Housing

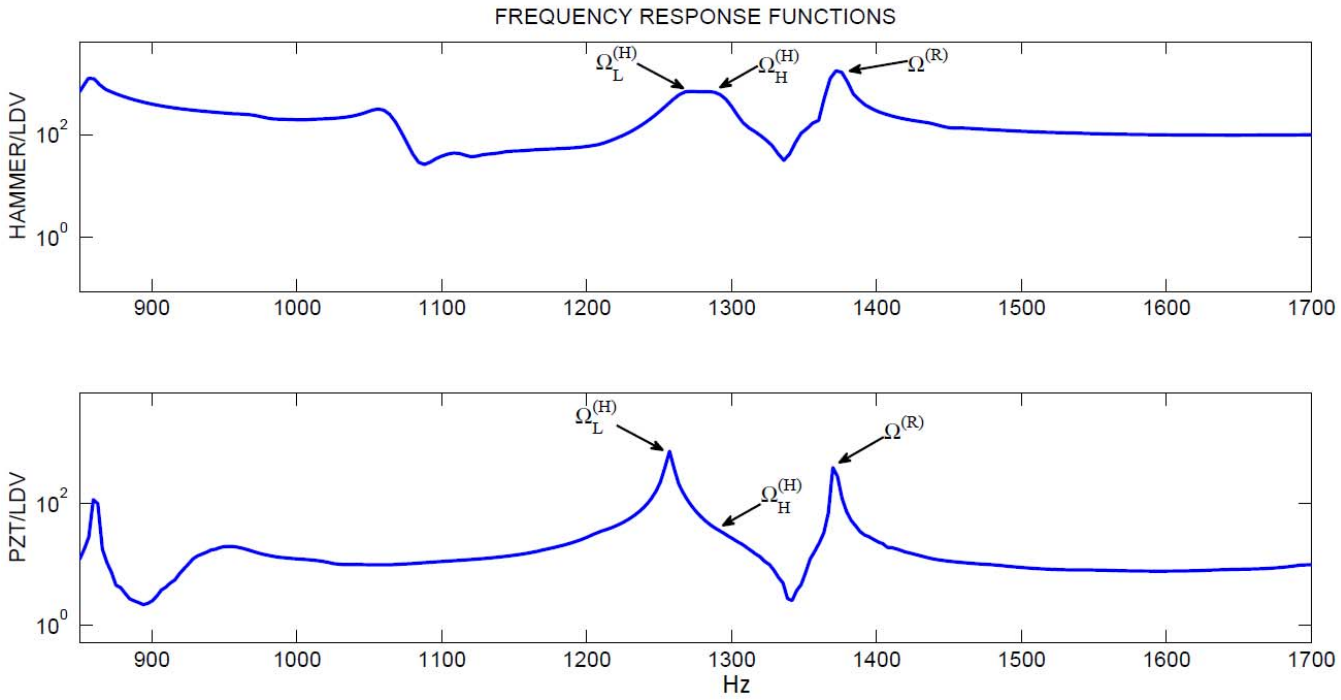

Figure 6.4: FRFs: Housing Dominant Modes. The Upper: FRFs with the Hammer/LDV. The Lower: FRFs with the PZT/LDV

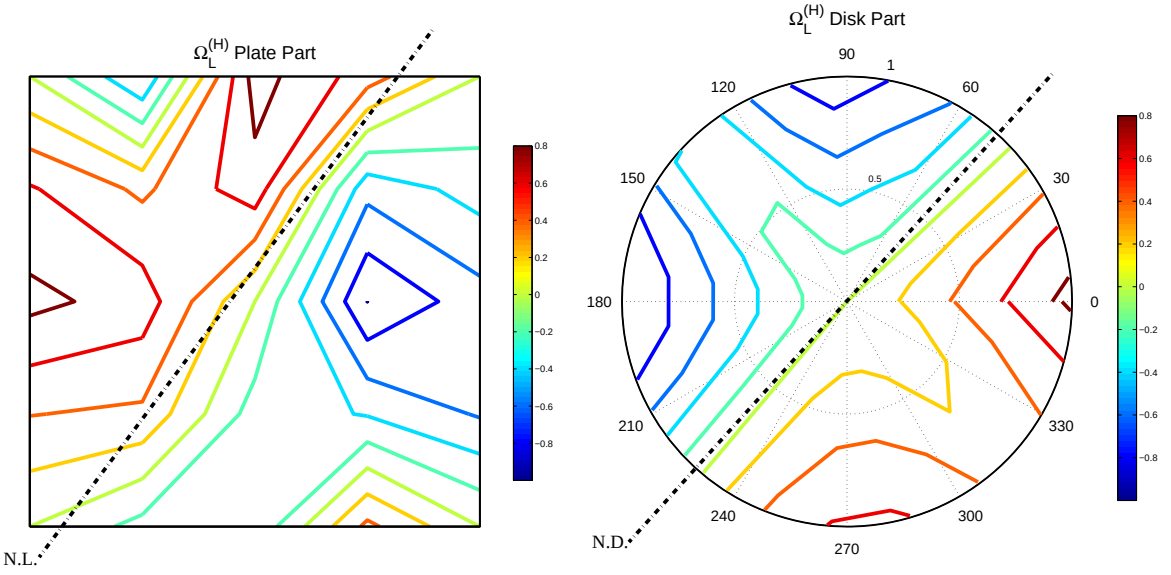

Figure 6.5: Experimental Mode Shapes: $\Omega_L^{(H)}$ Disk and Plate

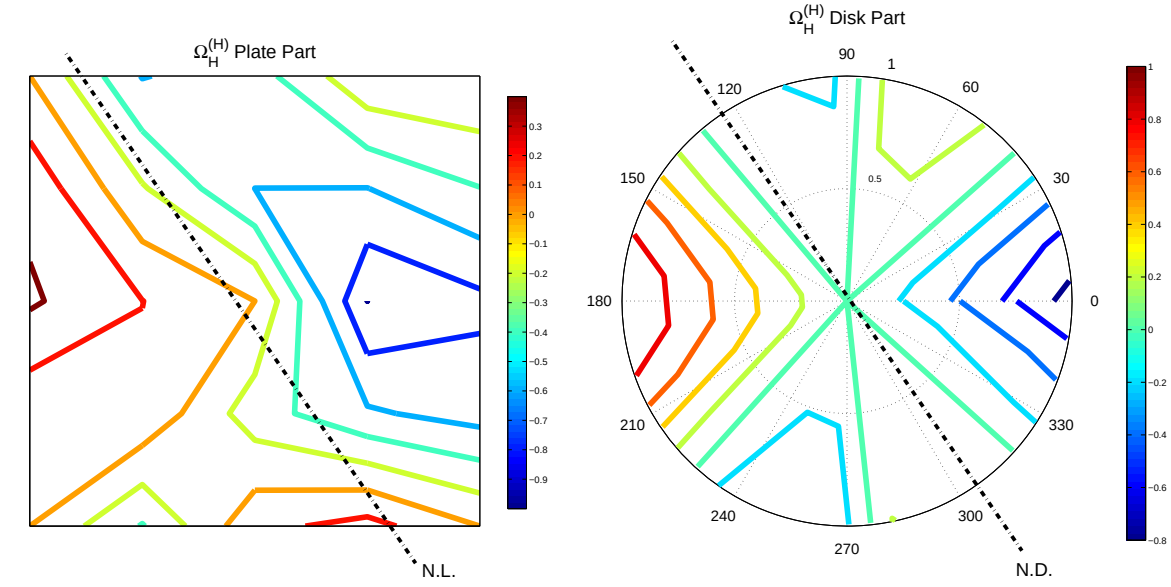

Figure 6.6: Experimental Mode Shapes: $\Omega_H^{(H)}$ Disk and Plate

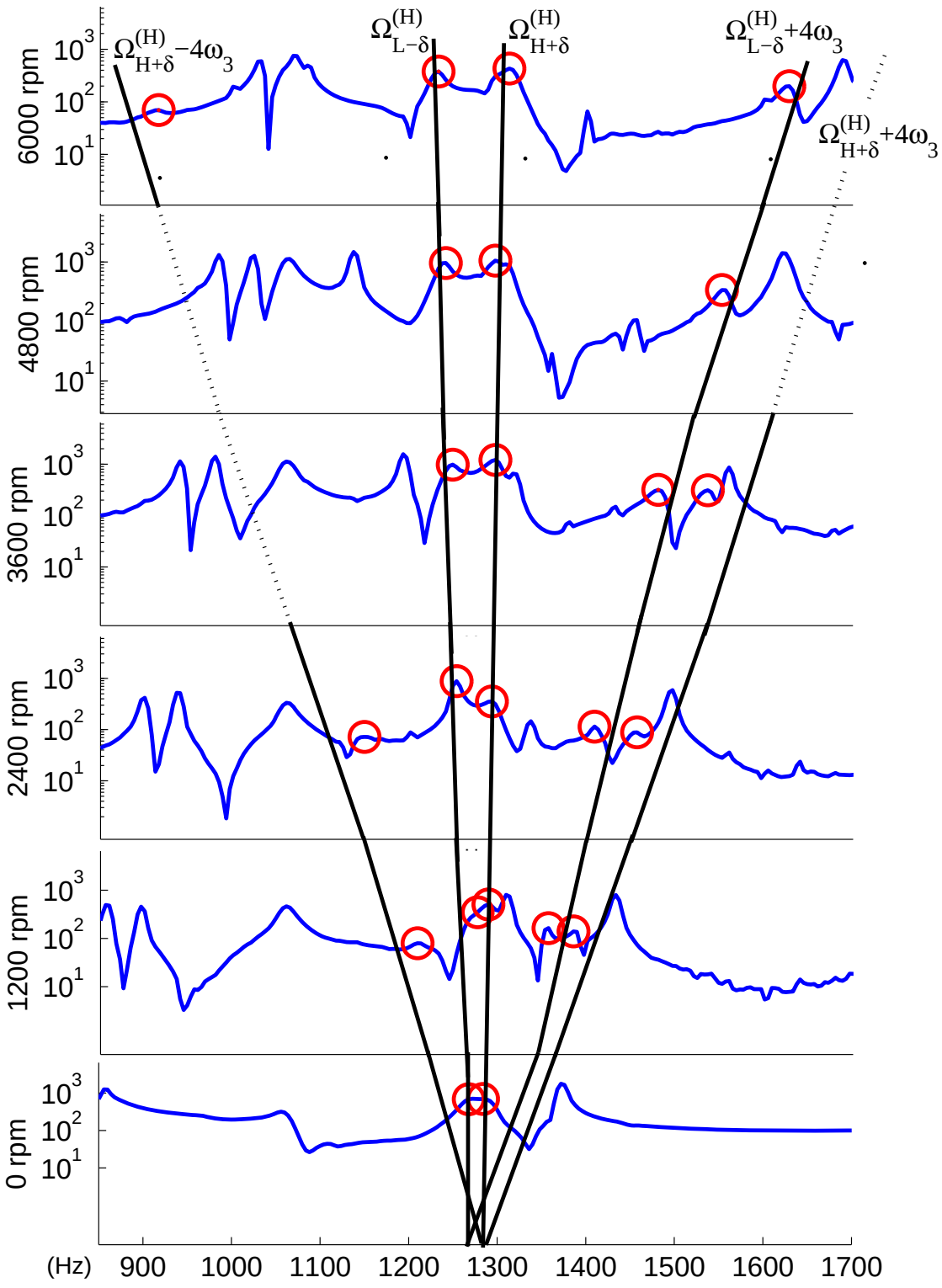

Figure 6.7: Waterfall with Hammer/LDV

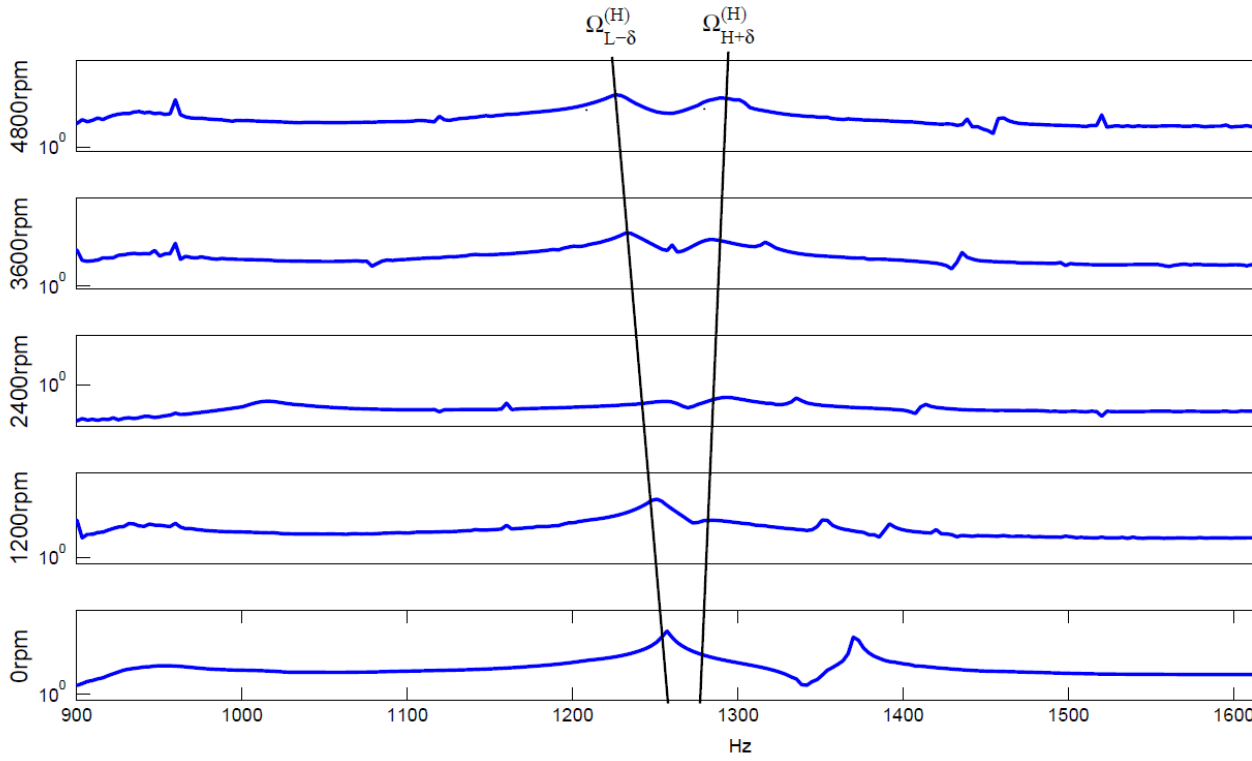

leftleft

Figure 6.8: Waterfall with PZT/LDV

Chapter 7

CONCLUSIONS AND FUTURE WORK

7.1 Conclusions

Through the theoretical, numerical, and experimental studies above, we reach the following conclusions.

1. For a spinning, cyclic symmetric rotor supported with linear bearings and an elastic housing, its equation of motion takes the form of a set of ordinary differential equation with periodic coefficients as shown in (2.50). The period is $2\pi/\omega_3$.

2. When the rotor is axisymmetric, the rotor-bearing-housing system could become unstable due to combination resonance of the sum type. The combination resonance involves a vibration mode of the housing and a vibration mode from the rotor. The vibration mode from the rotor can be a rigid-body translation mode, a rigid-body rocking mode, or an elastic rotor mode that has unbalanced inertia forces or moments (i.e., an unbalanced rotor mode). This combination resonance only occurs when the stiffness matrix, viewed from the ground-base observer, loses its positive definiteness.

3. When the rotor is cyclic symmetric, the rotor-bearing-housing system could become unstable due to combination resonance of the sum type. The combination resonance has the same characteristics as in the case of an axisymmetric rotor. Since cyclic symmetric rotors have more unbalanced modes, more combination resonances appear in spinning cyclic symmetric rotor-bearing-housing systems.

4. When damping is present in a coupled rotor-bearing-housing system, qualitative behavior of the instability is similar to that of a damped gyroscopic system with nonconservative forces. Damping of the housing widens the instability zones further desta-

bilizing the system. Rotor damping tends to stabilize the system by reducing the width of the instability zones.

5. Response of a rotor-bearing-housing system is in general a coupled vibration between the rotor and the housing. The coupled vibration can be classified as rotor-dominant modes and housing-dominant modes.

6. The phenomenon of gyroscopic splitting between rotor and housing is a characteristic of coupled rotor-bearing-housing system. Specifically, rotor response seen from a rotor-based observer shall contain frequency components that consist of a natural frequency of a housing-dominant mode plus or minus the spin speed, i.e., (4.9). Similarly, housing response seen from a ground-based observer shall contain frequency components that consist of a natural frequency of a rotor-dominant mode plus or minus the spin speed, i.e., (4.10). The gyroscopic splitting stems from the bearing coupling and the coordinate transformation between the rotor and housing.

7. The coupling of the rotor and housing will lead to specific frequency components in the rotor response as seen from a ground-based observer. For a housing-dominant mode, these frequency components will appear in the form of $\omega^{(H)} - (k+1)\omega_3$ and $\omega^{(H)} - (k-1)\omega_3$, where $\omega^{(H)}$ is the natural frequency of the housing-dominant mode. Moreover, $k = n + \mathbf{M}(N)$, where n is the phase index of the rotor mode that forms the housing-dominant mode, N is the number of substructure in the cyclic symmetric rotor, and $\mathbf{M}(N)$ is integer multiples of N. The presence of these frequency components manifests the coupling effect between the rotor and housing, because the phase index n belongs to the rotor and the natural frequency $\omega^{(H)}$ comes from the housing-dominant mode.

8. The phenomena of housing-dominant modes, gyroscopic splitting, and ground-base response of frequencies $\omega^{(H)} - (k \pm 1)\omega_3$ are all confirmed in the benchmark numerical model as well as in the calibrated experiments.

9. When the elastic part of a cyclic symmetric rotor has only out-of-plane motion and the

hub is rigid, only the repeated modes contribute to the periodic coefficients in the bearing stiffness (2.41). Consequently, the equation of motion (2.50) can be transformed into a time invariant gyroscopic system via an orthonormal coordinate transformation. Such system can then be solved exactly to obtain closed-form solutions.

10. In solving the transformed equation of motion, the gyroscopic splitting phenomenon is derived from the coordinate transformation.

11. Response of transformed equation of motion is verified to be identical to those from the original equation of motion via two numerical simulations.

7.2 Future Work

Based on the research progress achieved in this paper, current work can be extended to the following aspects in the future.

1. Instability regarding gyroscopic systems

2. Force response to excitations from the supports

3. Consideration of fluid dynamic bearings

The first area worth further study is instability of gyroscopic systems. Practically speaking, most rotary machines with cyclic symmetric rotors are gyroscopic systems, and gyroscopic forces dramatically influence the vibration responses. Despite the importance, how gyroscopic forces affect cyclic symmetric rotor-bearing-housing systems still lack fundamental understanding. In particular, Ariaratnam and Namachchivaya [36] pointed out parametrically excited gyroscopic systems may experience instability in terms of combination resonance of difference type. When it comes to rotary machinery, combination resonance of difference type is much more dangerous because it tends to happen when the spin speed is low. Hence, it is more crucial than the combination resonance of summation type discussed in Chap. 2.

The second area is force responses to excitations from the supports. For example, offshore wind turbines recently demonstrated their economic potential to efficiently harness renewable energy. In particular, floating offshore wind turbines employ floating foundations in order to harvest steady wind powers in deep ocean regions. The dynamic response between the turbine and platform in response to excitations from the wave motion is a major challenge [25, 26]. In terms of the current formulation, the offshore wind turbine/platform is equivalent to a cyclic symmetric rotor on a flexible housing subjected to prescribed excitations. It is expected that the dynamics of housings will essentially influence the interaction with rotors.

The third area is coupled rotor-bearing-housing systems with fluid dynamic bearing. When fluid dynamic bearings are present in the model, not only the bearing stiffness but the bearing damping will be periodic. The effects of periodic bearing damping remain largely unknown to spinning cyclic symmetric rotor-bearing-housing systems.

BIBLIOGRAPHY

[1] G. F. G. Jacquet-Richardet and P. Rieutord, "Frequencies and modes of rotating flexible bladed disc-shaft assemblies: A global cyclic symmetry approach," *Journal of Sound and Vibration*, vol. 191, pp. 901–915, Apr. 1996.

[2] E. P. P. M. Nikolic and D. J. Ewins, "Coriolis forces in forced response analysis of mistuned bladed disks," *Journal of Turbomachinery-Transactions of the Asme*, vol. 129, pp. 730–739, Oct. 2007.

[3] H. Kim and I. Y. Shen, "Ground-Based Vibration Response of a Spinning, Cyclic Symmetric Rotor with Gyroscopic and Centrifugal Softening Effects," *Journal of Vibration and Acoustics*, vol. 131, pp. 021007–1 to 021007–13, Apr 2009.

[4] I. Y. Shen and H. Kim, "A Linearized Theory on Ground-Based Vibration Response of Rotating Asymmetric Flexible Structures," *Journal of Vibration and Acoustics*, vol. 128, pp. 375–384, Oct 2006.

[5] H. K. C. W. Tseng, J. Y. Shen and I. Y. Shen, "A unified approach to analyze vibration of axisymmetric rotating structures with flexible stationary parts," *ASME Journal of Vibration and Acoustics*, vol. 127, pp. 125–138, Apr 2005.

[6] W. C. Tai and I. Y. Shen, "Parametric resonances of a spinning cyclic symmetric rotor assembled to a flexible stationary housing via multiple bearings," in *ASME IDETC/CIE 2012*, no. DETC2012-70150, (Chicago, IL, USA), 2012.

[7] D. L. Thomas, "Dynamics of rotationally periodic structures," *International Journal for Numerical Methods in Engineering*, vol. 14, pp. 81–102, 1979.

[8] J. Wildheim, "Excitation of rotating circumferentially periodic structures," *Journal of Sound and Vibration*, vol. 75, pp. 397–416, 1981.

[9] J. Wildheim, "Vibration of rotating circumferentially periodic structures," *Quarterly Journal of Mechanics and Applied Mathematics*, vol. 34, pp. 213–229, 1981.

[10] J. G. Tseng and J. A. Wickert, "On the vibration of bolted plate and flange assemblies," *Journal of Vibration and Acoustics*, vol. 116, pp. 468–473, Oct. 1994.

[11] I. Y. Shen, "Vibration of rotationally periodic structures," *Journal of Sound and Vibration*, vol. 172, pp. 459–470, May 1994.

[12] J. Tang and K. W. Wang, "Vibration control of rotationally periodic structures using passive piezoelectric shunt networks and active compensation," *Journal of Vibration and Acoustics*, vol. 121, pp. 379–390, Jul. 1999.

[13] J. Y. Chang and J. A. Wickert, "Response of modulated doublet modes to travelling wave excitation," *Journal of Sound and Vibration*, vol. 242, pp. 69–83, April 2001.

[14] J. Y. Chang and J. A. Wickert, "Measurement and analysis of modulated doublet mode response in mock bladed disks," *Journal of Sound and Vibration*, vol. 250, pp. 379–400, Feb. 2002.

[15] L. Kristensen and S. Frandsen, "Model for power spectra of the blade of a wind turbine measured from the moving frame of reference," *Journal of Wind Engineering and Industrial Aerodynamics*, vol. 10, pp. 249–262, 1982.

[16] A.-S. M. F. Lee, C. L. and T. G. Woehrle, "Natural frequency measurements for rotating spanwise uniform cantilever beams," *Journal of Sound and Vibration*, vol. 240, pp. 957–961, Mar 2001.

[17] D. H. H. D. Lee and M. J. Patil, "Multi-flexible-body dynamic analysis of horizontal axis wind turbines," *Wind Energy*, vol. 5, pp. 281–300, 2002.

[18] D. J. Malcolm, "Modal responses of 3-bladed wind turbines," *Journal of Solar Energy Engineering*, vol. 124, pp. 372–377, 2002.

[19] M. H. Hansen, "Improved modal dynamics of wind turbines to avoid stall-induced vibrations," *Wind Energy*, vol. 6, pp. 179–195, 2003.

[20] B. B. P. J. Murtagh and B. B. M., "Along-wind response of a wind turbine tower with blade coupling subjected to rotationally sampled wind loading," *Engineering Structures*, vol. 27, pp. 1209–1219, 2005.

[21] B. B. P. J. Murtagh, A. Ghosh and B. B. M., "Passive-control of wind turbine vibrations including blade/tower interaction and rotationally sampled turbulence," *Wind Energy*, vol. 11, pp. 305–317, 2008.

[22] *Wind Turbine Syndrome: a Report on a Natural Experiment.* Santa Fe, N.M.: K-Selected Books, 2009.

[23] O. D. Santiago and E. Abraham, "Rotordynamic analysis of a power turbine including support flexibility effects," in *ASME Turbo Exposition 2008*, no. GT2008-50900, (Berlin, Germany), 2008.

[24] P. Bonello and P. M. Hai, "Computational studies of the unbalance response of a whole aero engine model with squeeze-film bearings," in *ASME Turbo Exposition 2009*, no. GT2009-59687, (Orlando, Florida, USA), 2009.

[25] G. Betti, M. Farina, G. A. Guagliardi, A. Marzorati, and R. Scattolini, "Development of a Control-Oriented Model of Floating Wind Turbines," *IEEE TRANSACTIONS ON CONTROL SYSTEMS TECHNOLOGY*, vol. 22, pp. 69–82, JAN 2014.

[26] F. Viadero, A. Fernandez, M. Iglesias, A. de Juan, E. Liano, and M. A. Serna, "Non-stationary dynamic analysis of a wind turbine power drivetrain: Offshore considerations," *APPLIED ACOUSTICS*, vol. 77, pp. 204–211, MAR 2014.

[27] N. T. K. C. H. Kim and I. Y. Shen, "Mode Evolution of Cyclic Symmetric Rotors Assembled to Flexible Bearings and Housing," *ASME Journal of Vibration and Acoustics*, vol. 131, pp. 051008–1 to 051008–9, 2009.

[28] J. DUGUNDJI and J. WENDELL, "SOME ANALYSIS-METHODS FOR ROTATING SYSTEMS WITH PERIODIC COEFFICIENTS," *AIAA JOURNAL*, vol. 21, no. 6, pp. 890–897, 1983.

[29] G. Bir, "Multi-blade coordinate transformation and its application to wind turbine analysis," in *46th AIAA Aerospace Sciences Meeting and Exhibit*, no. AIAA 2008-1300, (Reno, Nevada), 7 - 10 January 2008.

[30] M. A. Dhadwal, H. S. and R. Khan, "Integrated fiber optic light probe: measurement of static deflections in rotating turbomachinery," *Review of Scientific Instruments*, vol. 67, pp. 546–552, February 1996.

[31] M. Zielinski and G. Ziller, "Noncontact vibration measurements on compressor rotor blades," *Mechanical Systems and Signal Processing*, vol. 11, pp. 847–856, July 2000.

[32] C. I. B. W. J. R. Dimitriadis, G. and J. E. Cooper, "Blade-tip timing measurement of synchronous vibrations of rotating bladed assemblies," *Mechanical Systems and Signal Processing*, vol. 16, no. 4, pp. 599–622, 2002.

[33] C. P. Slavic, J. and e. a. Babnik, A., "Measurement of the bending vibration frequencies of a rotating turbo wheel using an optical fibre reflective sensor," *Measurement Science and Technology*, vol. 13, pp. 477–482, April 2002.

[34] C. P. Lawson and P. C. Ivey, "Tubomachinery blade vibration amplitude measurement through tip timing with capacitance tip clearance probes," *Sensors and Actuators A-Physical*, vol. 118, pp. 14–24, January 2005.

[35] *Rotating Machinery Vibration: From Analysis to Troubleshooting*. Marcel Dekker, Inc., 2001.

[36] S. ARIARATNAM and N. NAMACHCHIVAYA, "PERIODICALLY PERTURBED LINEAR GYROSCOPIC SYSTEMS," *JOURNAL OF STRUCTURAL MECHANICS*, vol. 14, no. 2, pp. 127–151, 1986.

[37] Z. VIDERMAN, F. RIMROTT, and W. CLEGHORN, "PARAMETRICALLY EXCITED LINEAR NONCONSERVATIVE GYROSCOPIC SYSTEMS," *MECHANICS OF STRUCTURES AND MACHINES*, vol. 22, no. 1, pp. 1–20, 1994.

[38] K. Josic and R. Rossenbaum, "Unstable Solutions of Nonautonomous Linear Differential Equations," *SIAM Review*, vol. 50, pp. 570–584, SEP 2008.

[39] V. Kozlov, "Gyroscopic stabilization and parametric resonance," *PMM JOURNAL OF APPLIED MATHEMATICS AND MECHANICS*, vol. 65, no. 5, pp. 715–721, 2001.

[40] L. Mirovitch, "Rayleigh-Ritz Based Substructure Synthesis for Flexible Multibody Systems," *AIAA Journal*, vol. 29, pp. 1709–1719, Oct.

[41] P. H. K. Huseyin and W. Teschner, "On the Stability of Linear Conservative Gyroscopic Systems," *Journal of Applied Mathematics and Physics*, vol. 34, pp. 807–815, November 1983.

[42] K. Huseyin, "Standard Forms of Eigenvalue Problems Associated with Gyroscopic Systems," *Journal of Sound and Vibration*, vol. 45, pp. 29–37, 1976.

[43] L. Mirovitch, "New Method of Solution of Eigenvalue Problem for Gyroscopic systems," *AIAA Journal*, vol. 12, pp. 1337–1342, 1974.

[44] Y. S. T. Iwatsubo and S. Ogino, "Simple and Combination Resonances of Columns Under Periodic Axial Loads," *Journal of Sound and Vibration*, vol. 33, pp. 211–221, 1974.

[45] K. Takahashi, "Instability of Parametric Dynamic-Systems with Non-Uniform Damping," *Journal of Sound and Vibration*, vol. 85, pp. 257–262, 1982.

[46] O. N. Kirillov, "Paradoxes of dissipation-induced destabilization or who opened Whitneys umbrella?," *ZAMM-Journal of Applied Mathematics and Mechanics*, vol. 90, pp. 462–488, Jun 2010.

[47] *Vibrations and Stability of Multiple Parameter Systems.* Amsterdam: Sijthoff and Noordhoff, 1978.

[48] L. Meirovitch and G. Ryland, "A Perturbation Technique for Gyroscopic Systems with Small Internal and External Damping," *Journal of Sound and Vibration*, vol. 100, pp. 393–408, 1985.

[49] S. M. Yang and C. D. Mote, "Stability of Non-Conservative Linear Discrete Gyroscopic Systems," *Journal of Sound and Vibration*, vol. 147, pp. 453–464, Jun. 1991.

[50] O. N. Kirillov, "Gyroscopic Stabilization in the Presence of Nonconservative Forces," *DOKLADY MATHEMATICS*, vol. 76, pp. 780–785, Oct. 2007.

[51] C. S. Hsu, "On the Parametric Excitation of a Dynamic System Having Multiple Degrees of Freedom," *ASME* Journal of Applied Mechanics, vol. , no. , pp. pp. 367–372, 1963.

[52] *Differential Equations, Dynamical Systems, and an Introduction to Chaos, 2nd ed., Pure Appl. Math. (Amst.) 60*. Elsevier/Academic Press, Amsterdam, 2004.

Appendix A: Coordinate Transformation of Elastic Displacement Field of Axisymmetric Rotors

Let us define q and q' as the rotor-based and ground-based response respectively. The rotor-based and ground-based elastic displacement field of an axisymmetric rotor can be transformed from one the other as follows.

$$\begin{aligned}
\mathbf{W}(\tilde{\mathbf{r}}, t) &= \mathbf{W}(r, \theta, z)q \\
&= \mathbf{W}(r, \phi - \omega_3 t, z)q \\
&= \mathbf{A}(r, z)e^{j(\phi - \omega_3 t)}q \\
&= [\mathbf{A}(r, z)e^{j\phi}]e^{-j\omega_3 t}q \\
&= \mathbf{W}(r, \phi, z)q' \qquad (1)
\end{aligned}$$

where $\mathbf{W}(r, \theta, z)$ is the vibration motion as viewed in the rotor-based coordinate on which θ is measured whereas $\mathbf{W}(r, \phi, z)$ is the vibration motion as viewed in the ground-based coordinate on which ϕ is measured. Therefore, the ground-based response is related to the rotor-based response as $q' = e^{-j\omega_3 t}q$.

Appendix B: Linear Combination of Complex Mode Shapes to Real Mode Shapes

A pair of real repeated modes $\mathbf{W}^{\mathcal{R}}$ and $\mathbf{W}^{\mathcal{I}}$ can be derived by the linear combination of a pair of complex modes $\mathbf{W}^{\mathcal{C}}_{n=1}$ and $\mathbf{W}^{\mathcal{C}}_{n=N-1}$ with phase indices $n = 1$ and $n = N - 1$.

$$\begin{bmatrix} \mathbf{W}^{\mathcal{R}} \\ \mathbf{W}^{\mathcal{I}} \end{bmatrix} = \frac{\sqrt{2}}{2} \begin{bmatrix} 1 & 1 \\ -j & j \end{bmatrix} \begin{bmatrix} \mathbf{W}^{\mathcal{C}}_{n} \\ \mathbf{W}^{\mathcal{C}}_{-n} \end{bmatrix} \qquad p \in nr \tag{2}$$

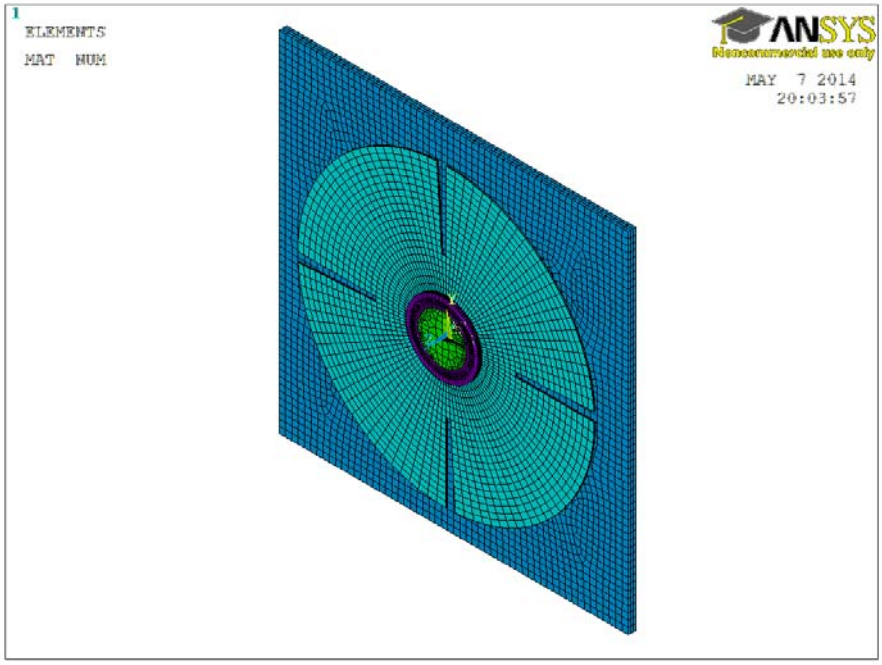

Figure 1: The Rotor-bearing-housing System. The Rotor and Housing are Modeled by Solid Elements

Appendix C: Finite Element Model of the Stationary Rotor-bearing-Housing System

The finite element analysis is performed in ANSYS. The rotor and housing are modeled by solid elements; see Fig. 1. The bearings are modeled by two methods. The first one is to use the multiple purpose constraint elements MPC184 with options of rigid beam and general joint. The rigid beam is used to constrain the degrees of freedom of the inner race and outer race of the rotor and housing to the general joints at the center of bearings; see Fig. 2. The second is to use MPC184 with options of rigid beam and general joint and the pilot node element TARGE170 and the surface contact element CONTA174. CONTA174 is used to constrain the degrees of freedom of the inner race and outer race of the rotor and housing to the pilot node created by TARGE170 which is later connected with MPC184 general joints at the center via MPC184 rigid beam; see Fig. 3.

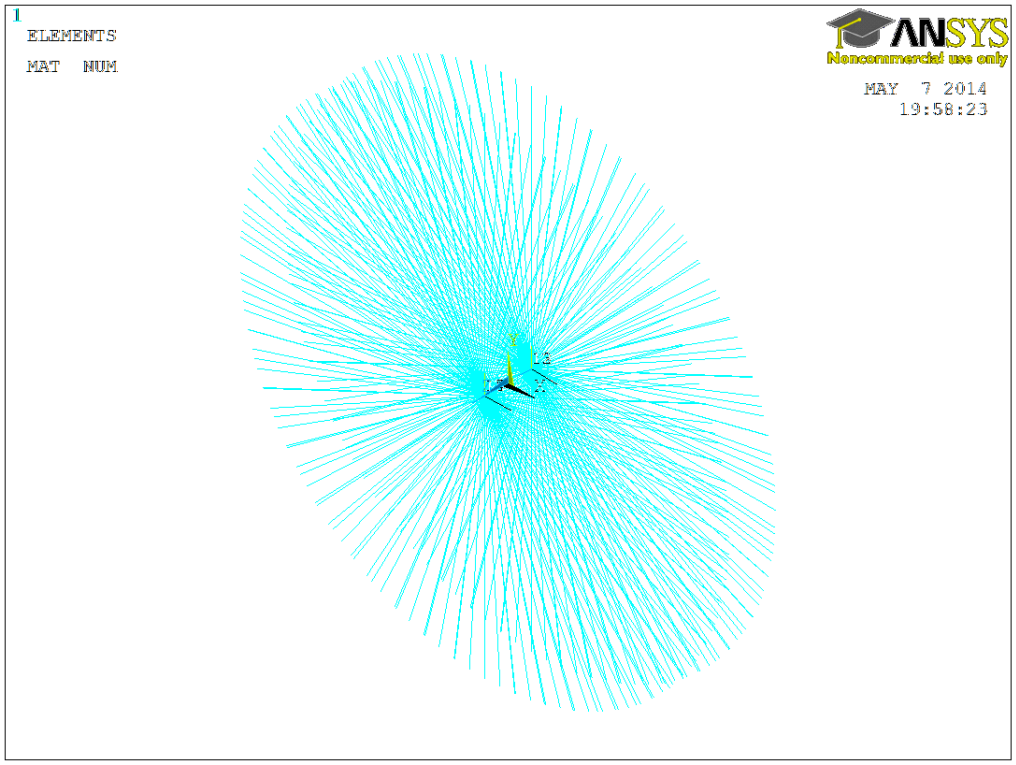

Figure 2: The Bearing. MPC184 Rigid Beam Constrain the DOF of the Inner and Outer races to MPC184 General Joints. The Two Local Coordinates Indicate the Position of General Joints. The Stiffness is Defined as Material Property of the Joints.

The source codes of the model using the contact element method is included as follows.

```
/prep7
csys,0
n,13837,0,0,6.715! lower bearing node of rotor
n,13838,0,0,6.715! lower bearing node of stator
n,13839,0,0,7.505! pilot node of rotor
n,13840,0,0,7.505! pilot node of stator
n,13841,0,0,8.295! upper bearing node of rotor
n,13842,0,0,8.295! upper bearing noe of stator
```

Figure 3: The Bearing. The Contact Element CONTA174 Constrain the DOF of the Inner and Outer Races to The Pilot Nodes Created by the Target Element Which is Later Connected to MPC184 General Joints via MPC184 Rigid Beam. The Two Local Coordinates Indicate the Position of The Pilot Nodes. The Stiffness is Defined as Material Property of the Joints.

```
csys,0
! step 1: Define a pilot node at the joint node of rotor with real constant 6
et,6,170
keyopt,6,2,1
real,6
tshap,pilot
type,6
e,13839 ! pilot element of rotor
! step 2: select the nodes of the corresponding surfaces
allsel
```

```
esel,s,mat,,2 ! the hub
nsle
csys,1
nsel,r,loc,x,12.495 ! inner race of the hub
! step 3: create the contact elements on the surface of rotor
et,7,174
keyopt,7,4,2
keyopt,7,2,2
keyopt,7,12,5
type,7
real,6
esurf
nsel,all

csys,0
! step 1: Define a pilot node at the joint node of stator with real constant 7
et,6,170
keyopt,6,2,1
real,7
tshap,pilot
type,6
e,13840 ! pilot element of stator
! step 2: select the nodes of the corresponding surfaces
allsel
esel,s,mat,,1 ! the shaft
nsle
csys,1
nsel,r,loc,x,12.495 ! outter race of the shaft
! step 3: create the contact elements on the surface of rotor
et,7,174
```

```
keyopt,7,4,2
keyopt,7,2,2
keyopt,7,12,5
type,7
real,7
esurf
nsel,all

!rigid beam of pilot node of rotor and bearing node of rotor
et,3,mpc184
keyopt,3,1,1 !1:rigid beam
keyopt,3,2,1 !lagrange multiplier
mat,1
type,3
e,13837,13839
e,13839,13841

!rigid beam of pilot node of stator and bearing node of stator
et,3,mpc184
keyopt,3,1,1 !1:rigid beam
keyopt,3,2,1 !lagrange multiplier
mat,1
type,3
e,13838,13840
e,13840,13842

!bearing
csys,0
et,4,mpc184
keyopt,4,1,16 !general link
```

keyopt,4,4,0 !1:only dis DOF are activated, 0:dis&rot DOFs are activated

sectype,4,joint,gene !general joint lower b

local,12,0,0,0,6.715

local,13,0,0,0,6.715

secjoint,,12,13

sectype,5,joint,gene !general joint upepr b

!!there we use only 3 dof, so we don't need to constraint more dof by secjoint and don't need to name local coord as below

local,14,0,0,0,8.295

local,15,0,0,0,8.295

secjoint,,14,15

kyyy=2.16e7

kxxx=2.16e7

kzzz=5.76e6

krotx=58.5e3

kroty=58.5e3

krotz=0

tb,join,3,,,stif !3 is material number

tbdata,1,kxxx

tbdata,7,kyyy

tbdata,12,kzzz

tbdata,16,krotx

tbdata,19,kroty

tbdata,21,krotz

csys,0

mat,3

secnum,4

type,4

e,13837,13838

mat,3

secnum,5

type,4

e,13841,13842